Luminescence studies and stability of bismuth doped lanthanum oxide and oxysulphide

By

Babiker Mohammed Jaffar Jabraldar

(B.Sc. Hons)

A dissertation submitted in fulfilment of the requirements for the degree

Magister Scientiae

in the

Faculty of Natural and Agricultural Sciences

Department of Physics

at the

University of the Free State

Republic of South Africa

Supervisor: Prof. R. E. Kroon

Co-supervisor: Prof. H. C. Swart

Co-supervisor: Dr. Hassan Abdel Halim Abdallah Seed Ahmed

Co-supervisor: Dr. Abdelrhman Yousif Mohmmed Ahmed

January 2019

Dedication

I dedicate this work to my lovely father: Mohammed Jaffar.

To my mother: Madiana Babiker, for her support, encouragement, and constant love have sustained me throughout my life.

To my brothers and sisters, for their respect and appreciation.

To all people who were suffering to create peace in my country and the world.

Declaration

I declare that this dissertation is mine and that it has not been submitted before for any degree or examination in any other University.

Babiker Mohammed Jaffar January 2019

Signature: 

Acknowledgements

I would like to thank the following individuals and institutions:

- My supervisor Prof R.E. Kroon who has supported me throughout my thesis with his patience and knowledge.
- Special thanks goes to Prof. H.C. Swart for giving me this opportunity to be part of the Department of Physics family and for his guidance and professional suggestions throughout this thesis as my co-supervisor.
- My co-supervisor Dr. Hassan Seed Ahmed for all his support and assistance.
- Dr. A. Yousif for being my co-supervisor and assisting me with all the chemistry involved in my project.
- Prof Liza Coetzee for measuring XPS and Auger spectra and SEM images.
- Mr. Emad Hasabeldaim for assistance with CL and AES measurements.
- The phosphor group at the University of the Free State for their good discussions.
- Dr. Ella Linganiso, Dr. Puseletso Mokoena and E. Lee of the center of microscopy UFS for their assistance in SEM measurements.
- Dr. N.J. Shivaramu for assistance with FTIR measurements.
- Dr. S.P. Tiwari for assistance with encapsulation of the phosphor in the PMMA polymer.
- For all my brothers and sisters from Sudan who are in Bloemfontein of always being together.
- Special thanks to Dr. Mohammed Abdul Aziz and his family (his wife Sarah and his kids Fatima and Tasneem) for their assistance.
- Special thanks to my lovely family, my parents for their support, encouragement, love and constant assistance throughout my life, to my sisters and brothers for their respect, appreciation, encouragement and constant love.
- My deep thanks and gratitude goes to the African Laser Centre (ALC) for their financial support.

ABSTRACT

Different concentrations of bismuth doped lanthanum oxide ($La_{2-x}O_3:Bi_x$) phosphor powder (x = 0.001, 0.002, 0.003, 0.004, 0.006, 0.008 and 0.01) were synthesised by means of the sol-gel combustion method at 250 °C using citric acid as the fuel. The product was annealed at different temperatures and the luminescence properties were investigated. The maximum photoluminescence (PL) emission was obtained for the sample which was doped with x = 0.002 and annealed at 1200 °C in air. The X-ray diffraction (XRD) analysis confirmed that all samples crystallized in the La_2O_3 hexagonal phase. The scanning electron microscopy (SEM) data showed that the grain size increased with increasing annealing temperature and the shape of the grains changed from rectangular to more round, but faceted, after annealing at 1200 °C in air. Energy dispersive X-ray spectroscopy (EDS) confirmed the chemical composition, while diffuse reflectance spectroscopy was used to study the absorption of the $La_{2-x}O_3:Bi_x$ samples. All the samples were absorbing in the ultraviolet range between 220 to 320 nm. The band gap of the La_2O_3 pure host sample was obtained from the reflectance data as 5.1 eV. Excitation at a wavelength of 308 nm resulted in a single broad blue luminescence emission band centred at 462 nm. The excitation and emission bands were attributed to transitions between the $^1S_0$ ground state and the $^3P_1$ excited state of Bi^{3+} ions, with a Stokes shift of 1.35 eV.

It was found that the samples no longer exhibited PL after storage of several weeks. Further XRD measurements revealed that the La_2O_3 had changed to $La(OH)_3$. This is consistent with reports that La_2O_3 can absorb moisture from the air and transform to $La(OH)_3$, which was observed to occur completely in about a week. Unlike for La_2O_3:Eu and La_2O_3:Ho phosphors for which the transformation reduced the luminescence, but did not quench it completely, the luminescence of the degraded La_2O_3:Bi was negligible so that simply the presence of luminescence can be used to indicate whether the transformation is not yet complete. This may be useful to use PL to monitor the transformation of La_2O_3 for other applications, e.g. ceramics and catalysis. If the transformed samples were re-annealed in air at 800 °C for 2 h, XRD results showed that the structure reverted completely to La_2O_3 and the blue PL emission was once again observed, however at only about one third of the intensity as for freshly prepared samples. For samples stored in a vacuum desiccator for one week, no change for XRD and PL were observed. Therefore La_2O_3:Bi phosphor may have application as a

moisture sensor, because while the luminescence remains high it is evidence that it has not been exposed to the atmosphere. Degradation was effectively slowed, but not eliminated, by encapsulation of the phosphor in poly(methyl methacrylate) polymer.

Therefore Bi^{3+} doped lanthanum oxysulphide (La_2O_2S) phosphor was synthesised to compare its stability and suitability as a blue emitting phosphor material. Synthesis was performed via the ethanol-assisted solution combustion method, followed by annealing for 2 h at 900 °C in a reducing atmosphere (5% H_2 in Ar gas). XRD data confirmed that all samples crystallized in the La_2O_2S hexagonal lattice. SEM data showed that the particles aggregated and had irregular shapes. EDS confirmed the chemical composition, although the Bi dopant could not be identified since its expected peak position overlapped that of S. The samples, measured by diffuse reflectance spectroscopy, were absorbing in the ultraviolet range between 220 to 350 nm. The band gap of the pure host La_2O_2S was found to be 4.90 eV. Excitation at a wavelength of 260 nm and 344 nm resulted in a single broad blue luminescence emission band centred at 456 nm, which was attributed to transitions between the $^1S_0$ ground state and the $^3P_1$ excited state of Bi^{3+} ions. La_2O_2S:Bi phosphor was found to have a similar emission colour as La_2O_3:Bi, although less pure and closer to the centre of the Commission International Eclairge (CIE) diagram. Although the emission intensity of La_2O_2S:Bi phosphor was initially less than the La_2O_2:Bi phosphor, it was found to be stable and therefore superior for applications where the phosphor will be exposed to the atmosphere. La_2O_2S:Bi phosphor also exhibited persistent luminescence, which was attributed to the Bi^{3+} ions acting as hole traps and host defects acting as electron traps.

The cathodoluminescence (CL) of the $La_{2-x}O_3:Bi_{x=0.002}$ and $La_{2-x}O_2S:Bi_{x=0.002}$ phosphors was compared and they were assessed for possible application in field emission displays (FEDs). Since the phosphor is not exposed to the atmosphere such an application, bulk hydroxylation of the La_2O_3:Bi cannot occur. However, electron-stimulated surface chemical reactions caused by the electron beam are known to induce changes on the surface of phosphors that can lead to CL degradation. Simultaneous CL and Auger electron spectroscopy (AES) measurements were performed during long term exposure of the samples to an electron beam to assess the CL degradation and chemical changes on the surface. X-ray photoelectron spectroscopy (XPS) measurements were also made on the samples before and after CL degradation. It was found that after a small amount of initial CL degradation, associated with removal of contamination from the surface, the La_2O_3:Bi sample remained stable under the

electron beam and it may be suitable for use in FEDs. However, the La_2O_2S:Bi showed continuous and severe CL degradation and is not suitable for CL applications. During degradation AES measurements showed that there was a decrease in the surface concentration of S, suggesting the formation of a non-luminescent La_2O_3 surface layer which was responsible for degradation. However, some S remained on the surface and XPS spectra showed that a sulphate, possibly $La_2O_2SO_4$, was present on the surface, which may have contributed to the degradation.

Keywords

La_2O_3; La_2O_2S; Bi^{3+} ions; Photoluminescence; Stability; Cathodoluminescence; Degradation

Acronyms

AES	Auger electron spectroscopy.
APPH	Auger peak-to-peak heights.
CL	Cathodoluminescence.
CRTs	Cathode ray tubes
DRS	Diffuse reflectance spectroscopy
EASC	Ethanol-assisted solution combustion
EDS	Energy dispersive spectroscopy
ESCA	Electron spectroscopy for chemical analysis
FEDs	Field emissive displays
FTIR	Fourier transform infrared spectroscopy
FWHM	Full width at half maximum
JCPDS	Joint Committee on Powder Diffraction Standards
LCDs	Liquid crystal displays
LEDs	Light emitting diodes
MMCT	Metal to metal charge transfer
PL	Photoluminescence.
PMMA	Poly (methyl methacrylate)
SEM	Scanning electron microscopy.
UHV	Ultra high vacuum
UV-vis	Ultraviolet-visible
XPS	X-ray photoelectron spectroscopy.
XRD	X-ray diffraction.

Table of Contents

Chapter 1
Introduction

1.1. Overview

Luminescent materials, also called phosphors, are materials that can emit light when they are excited by external sources of energy such as photons, electron beam, electric field, etc. Phosphor materials have many applications in new technology such as light sources like fluorescent tubes and light emitting diodes (LEDs), displays and scintillators [1].

Usually phosphors consist of a host material having wide band gap, such as an oxide, sulphide, silicate, selenide, halide, nitride, oxynitride or oxyhalide, doped with small amounts of activator ions called luminescent centres, like rare-earth and/or transition metal ions. These luminescent centres have energy levels that can be excited directly or indirectly by energy transfer.

Activator ions can be classified into two types. The first type has energy levels possessing weak interactions with the host lattice. Most of the lanthanide ions are typical examples of this type. The low lying *f* orbitals are well shielded from their coordination environment, thus giving rise to characteristics line emission spectra from the sharp *f-f* transitions. The second type of activator ions interact strongly with the host lattice. Examples include Mn^{2+}, Eu^{2+} and Ce^{3+} ions where *d*-electrons are involved. The *d*-orbitals have a pronounced interaction with the crystalline host lattice which lifts the degeneracy and leads to distinct energy states, giving rise to broad bands in the spectrum. The luminescence of Bi^{3+} ions is less intensively studied than the lanthanide and transition metal ions and are of the second type.

The stability of the phosphor under the application conditions is an inevitable issue for moving from the laboratory to the industry level and then to the public uses: phosphors which are used in field emissive displays (FEDs) must be stable under the electron beam irradiation, and for the use in photonic applications it must be stable under photon irradiation as well.

In this research study La_2O_3 and La_2O_2S phosphor powders have been investigated as phosphor host materials, both doped with Bi. Structural and luminescence properties of the prepared phosphors were studied experimentally by using different analytical techniques, i.e. X-ray diffraction, ultraviolet–visible spectroscopy, scanning electron microscopy, energy dispersive spectroscopy, infrared spectroscopy, photoluminescence spectroscopy, cathodoluminescence spectroscopy, X-ray photoelectron spectroscopy and Auger electron spectroscopy.

1.2. Problem statement

Lanthanum oxide (La_2O_3) has attracted much research interest because of its prospect as catalytic material and for thermal, chemical, electrical, magnetic, ceramic and optical applications [2]. In addition, La_2O_3 has a high dielectric constant, high melting point, large band gap, and low lattice energy while displaying good electrical properties [3]. La_2O_3 is recognized as having a relatively low cost compared to other rare earth oxides (Lu_2O_3, Gd_2O_3, etc.) and as an excellent host lattice material for activators [4]. It has been used as a host lattice to produce phosphors emitting a variety of colours, but mainly when doped with lanthanides ions such as Eu [5], Er [6] and Yb [7]. There has also been some interest in the blue emission when doped by Bi^{3+} ions [8], but more studies are required for La_2O_3 doped with Bi.

For any phosphor to be used in an application, its stability under a particular application environment is an important consideration. The host La_2O_3 has been found to be hygroscopic and converted to a hydroxide within days after exposure to the atmosphere. Therefore Bi^{3+} doped lanthanum oxysulphide (La_2O_2S) phosphor was synthesised to compare its stability and suitability as a blue emitting phosphor material. The crystal structure of La_2O_2S is similar to that of La_2O_3, and it can be described simply by the alternation of the anionic layers of La_2O_3 [9]. This also means that sulphur atoms in La_2O_2S occupy three of the seven oxygen sites in the La_2O_3 unit cell. However, La_2O_2S has been assessed as a phosphor host doped with lanthanides ions such as Yb [10], Eu^{3+} [11], Tb^{3+} [12], but there have been no reports yet of La_2O_2S doped with Bi. We consider adding Bi as an activator to improve the emission in this host La_2O_2S.

1.3. Research aims

1. To prepare La_2O_3 phosphor powders doped with Bi using the sol-gel combustion method.
2. To synthesize La_2O_2S phosphor powders doped with Bi using the ethanol-assistant solution combustion method.
3. To study the crystal structure of the phosphors and determining the crystallite size with X-ray diffraction.
4. To study the morphology of the phosphors with scanning electron microscopy and a scanning Auger electron microprobe.
5. To determine the chemical composition of the phosphors by energy dispersive X-ray spectroscopy.
6. Measuring the absorption and reflectance of the phosphors and determining the band gap from this data.
7. To study the photoluminescence properties of La_2O_3:Bi and La_2O_2S:Bi phosphor powders.
8. To investigate the cathodoluminescence degradation of La_2O_3:Bi and La_2O_2S:Bi phosphor powders.
9. To study the stability of La_2O_3:Bi phosphor powders in the atmosphere and in a polymer composite.
10. To compare La_2O_2S:Bi with La_2O_3:Bi in terms of its luminescence and stability, both for photoluminescence in the atmosphere and for cathodoluminescence when exposed to an electron beam in a vacuum chamber.

1.4. Layout of the thesis

This dissertation consists of eight chapters. *Chapter* 1 presents a general introduction about the work and aims of the study. *Chapter* 2 includes background information on fundamentals of phosphors and luminescence processes. *Chapter* 3 gives a brief description of the experimental techniques that were used to synthesize and characterize the phosphors. *Chapter* 4 presents the luminescence properties of Bi doped La_2O_3 powder phosphor. Stability of $La_2O_3:Bi^{3+}$ powder phosphor prepared via sol-gel combustion method is discussed in *chapter* 5. *Chapter* 6 discusses the comparison study of $La_2O_2S:Bi^{3+}$ with $La_2O_3:Bi^{3+}$ phosphor powder. In *chapter* 7 cathodoluminescence degradation of $La_2O_3:Bi^{3+}$ and $La_2O_2S:Bi^{3+}$ powder phosphors are presented. Finally, a summary of the thesis as well as future work are given in *chapter* 8.

1.5. References

1. William M. Yen, Shigeo Shionoya, Hajime Yamamoto. Phosphor Handbook. 2nd Edition. CRC Press, Boca Raton, London New York (2007). ISBN: 0-8493-3564-7

2. Xing Wang, Hongxia Liu, Lu Zhao, Chenxi Fei, Xingyao Feng, Shupeng Chen, Yongte Wang. Structural Properties Characterized by the Film Thickness and Annealing Temperature for La_2O_3 Films Grown by Atomic Layer Deposition. *Nanoscale Research Letters* 12 (2017) 233. https://doi.org/10.1186/s11671-017-2018-8

3. L. Armelao, M. Pascolini, G. Bottaro, G. Bruno, M.M. Giangregorio, M. Losurdo, G. Malandrino, R. Lo Nigro, M.E. Fragala. Microstructural and Optical Properties Modifications Induced by Plasma and Annealing Treatments of Lanthanum Oxide Sol-Gel Thin Films. *The Journal of Physical Chemistry C* 113 (2009) 2911–2918. https://doi.org/ 10.1021/jp809824e

4. M. Méndez, J. J. Carvajal, L. F. Marsal, P. Salagre, M. Aguiló, F. Díaz, P. Formentín, J. Pallarès and Y. Cesteros. Effect of the $La(OH)_3$ Preparation Method on the Surface and Rehydroxylation Properties of Resulting La_2O_3 Nanoparticles. *Journal of Nanoparticle Research* 15 (2013) 1479. https://doi.org/10.1007/s11051-013-1479-7

5. B. Pu, Z. Mo, C. Jiang, R Guo. Synthesis and Luminescence Properties of Rod-Shaped $La_2O_3:Eu^{3+}$ Nanocrystalline Using Carbon Nanotubes as Templates. *Synthesis and Reactivity in Inorganic, Metal-Organic and Nano-Metal Chemistry* 45 (2015) 988–992. https://doi.org/10.1080/15533174.2013.843547

6. A.K. Singh, S. Singh, D. Kumar, D.K. Rai, S.B. Rai, K. Kumar. Light-into-Heat Conversion in $La_2O_3:Er^{3+}$-Yb^{3+} Phosphor an incandescent emission. *Optics Letters* 37 (2012) 776–778. https://doi.org/10.1364/OL.37.000776

7. Xiao Zhang, Piaoping Yang, Dong Wang, Jie Xu, Chunxia Li, Shili Gai, Jun Lin. $La(OH)_3:Ln^{3+}$ and $La_2O_3:Ln^{3+}$ (Ln = Yb/Er, Yb/Tm, Yb/Ho) Microrods: Synthesis and Up-Conversion Luminescence Properties. *Crystal Growth & Design* 12 (2012) 306–312. https://doi.org/10.1021/cg201091u

8. Toshihiro Miyata, Jun Ichi Ishino, Keiichi Sahara, Tadatsugu Minami. Color Control of Emissions from Rare Earth-Co-Doped La_2O_3:Bi Phosphor Thin Films Prepared by Magnetron Sputtering. *Thin Solid Films* 519 (2011) 8095–8099. https://doi.org/10.1016/j.tsf.2011.04.236

9. Guodong Liu, Qinghong Zhang, Hongzhi Wang, Yaogang Li. A Reddish La_2O_2S-Based Long-Afterglow Phosphor with Effective Absorption in the Visible Light Region. *Materials Science and Engineering B: Solid-State Materials for Advanced Technology* 177 (2012) 316–320. https://doi.org/10.1016/j.mseb.2011.12.045

10. Xi-xian Luo, Wang-he Cao. Ethanol-Assistant Solution Combustion Method to Prepare La_2O_2S:Yb,Pr Nanometer Phosphor. *Journal of Alloys and Compounds* 460 (2008) 529–534. https://doi.org/10.1016/j.jallcom.2007.06.011

11. Guicheng Jiang, Xiantao Wei, Yonghu Chen, Changkui Duan, Min Yin, Bin Yang, Wenwu Cao. Luminescent $La_2O_2S:Eu^{3+}$ nanoparticles as Non-Contact Optical Temperature Sensor in Physiological Temperature Range. *Materials Letters* 143 (2015) 98–100. https://doi.org/10.1016/j.matlet.2014.12.057

12. Lixi Wang, Xiaojuan Yang, Qitu Zhang, Bo Song, Chingping Wong. Luminescence Properties of $La_2O_2S:Tb^{3+}$phosphors and Phosphor-Embedded Polymethylmethacrylate Films. *Materials and Design* 125 (2017) 100–108. https://doi.org/10.1016/j.matdes.2017.04.003

Chapter 2

Background information and applications of phosphors

2.1. Fundamentals of phosphors

Phosphors, also called luminescent materials, are solid compounds that will emit light, or luminesce, when exposed to an external energy excitation source [1]. Excitation can be according to different types of sources such as photons, voltage or electric field, etc. Phosphors are mostly inorganic materials and are widely available in the form of powders, but in some cases they may be in the form of thin films [2]. A phosphor consists of a host lattice, which is normally either an insulator or semiconductor with a wide band gap, which is usually intentionally doped with impurities (such as rare earth ions) to act as activators for luminescence. Due to the concentration quenching phenomenon, the concentration of the activator is generally low.

The common representation of a phosphor is given by a formula such as $La_2O_3:Bi^{3+}$ (0.2 mol%), where La_2O_3 represents the host, bismuth Bi^{3+} represents the activator and 0.2 mol% indicates the concentration of the activator per mole relative to the host matrix.

Generally, a good host for luminescent ions must exhibit properties such as transparency for visible and infrared light as well as good chemical and structural stability [3]. In fact, there are different kinds of host materials such as alkali-earth aluminates, alkali-earth sulphides, rare-earth oxides, lanthanide halides, nitrides and oxysulphides, gallates and silicates, etc.

Phosphors are used in several emerging advanced high technology applications today. The applications of phosphors can be listed as: (1) lighting sources; (2) display devices; (3) detectors and scintillators; and (4) other simple applications, such as luminous paint with long persistent phosphorescence [4] Figure 2.1 illustrates some of these applications. Major applications are in emissive displays and fluorescent lamps. In addition, some X-ray detector systems are based on luminescent materials as well [5].

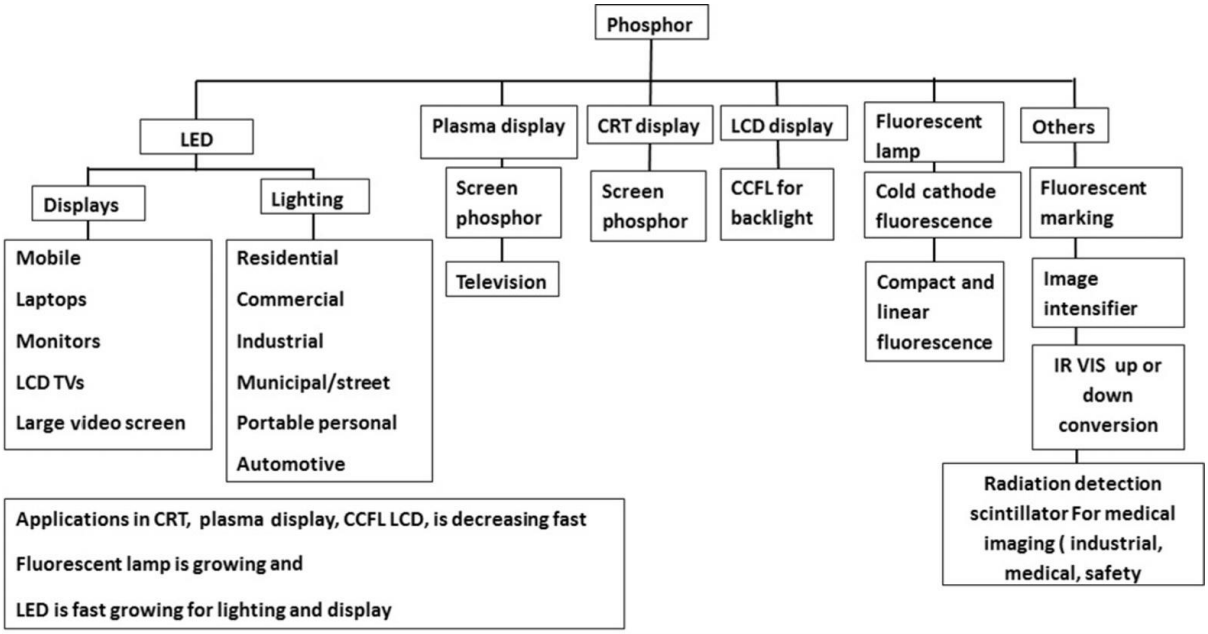

Figure 2.1: The application range of phosphors in various applications [6].

2.2. Luminescence

Luminescence, also called cold light, is a process of light emission from any material when it is excited using an external energy source [7] if the light is not emitted due to the high temperature of the material, which would represent incandescence. Luminescence is due to electrons being excited by the external source. They absorb the excitation energy and jump to a higher energy level, where after short relaxation time the electrons will return back to their ground state level, releasing their energy as light [7].

Luminescence can be classified into two categories, namely fluorescence and phosphorescence, depending on the amount of time emitted light continues to glow (figure 2.2). Fluorescence is a fast luminescence process in which emission stops suddenly after the excitation source has been removed, whereas phosphorescence is a slow luminescence process whereby the light emission from a substance continues for a few seconds, minutes or even hours after the excitation has ceased [7].

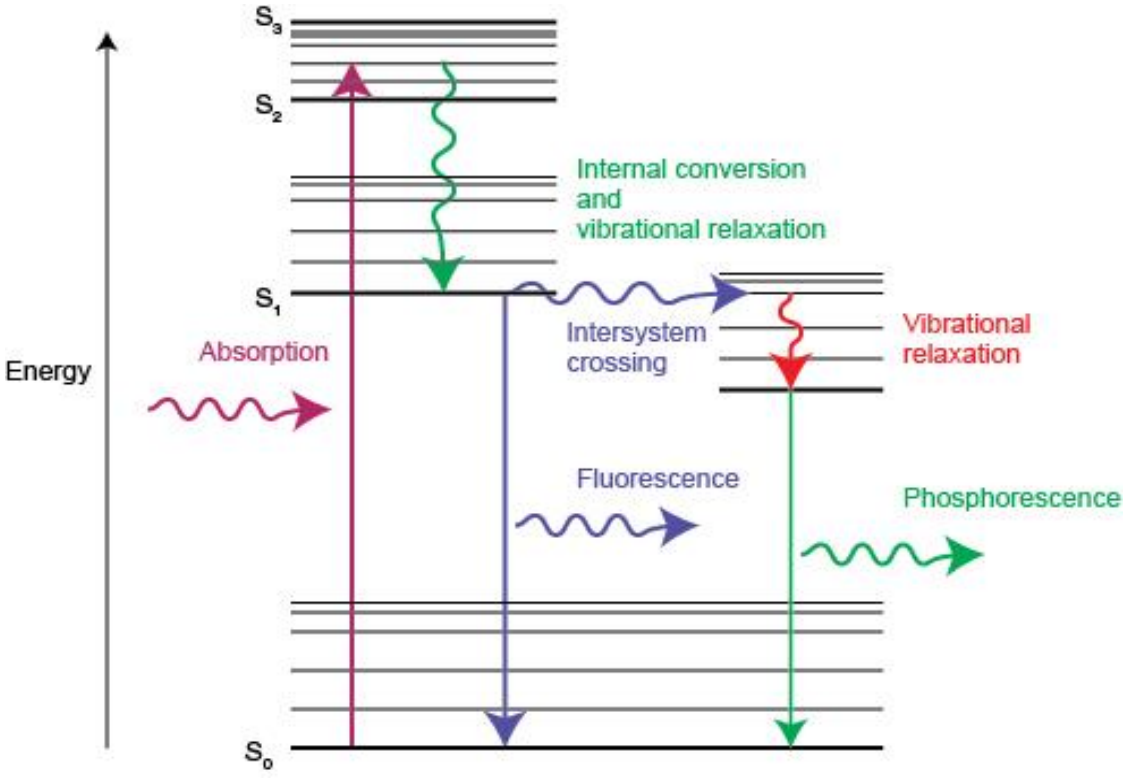

Figure 2.2: Energy level diagram showing absorption, emission, fluorescence and phosphorescence processes [8].

2.3. Types of luminescence

There are various types of luminescence, each classified differently according to the excitation method used. For **photoluminescence** light emission is produced by absorption of photons or light; **cathodoluminescence** is produced when an electron beam impacts on a luminescent material; **bioluminescence** is generated by a living organism such as a firefly; **chemiluminescence** results from a chemical or electrochemical reaction; **radioluminescence** occurs due to exposing materials to ionizing radiation like α, β or γ rays; **electroluminescence** is produced when an electric current passes through a material; **crystalloluminescence** is produced during crystallization; **thermoluminescence** is luminescence activated thermally after initial irradiation by other means such as α, β, γ, UV or X-rays; **mechanoluminescence** is generated due to any mechanical impact on a solid and **sonoluminescence** is the emission of short bursts of light from imploding bubbles in a liquid produced by high frequency sound waves or phonons [9].

2.4. Band gap

In solid-state physics an energy range where no electron states can exist in a solid is called an energy or band gap. Materials having a band gap are referred to as insulators or semiconductors and the band gap energy refers to the difference between the top of the valence band and the bottom of the conduction band. The band gap energy of insulators is larger than that of semiconductors [10].

Semiconductor materials have a filled valence band and an empty conduction band (Figure 2.3). Electrons from the valence band can be excited to the conduction band by either thermal excitation or by optical absorption. When the electron returns to the valence band the energy is released either as heat or as photons [11].

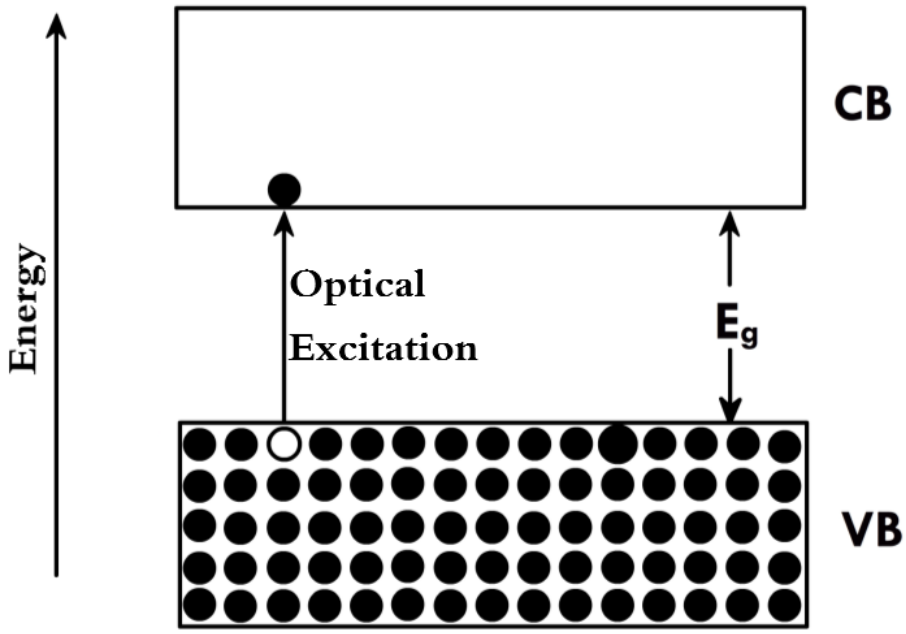

Figure 2.3: Band picture of a semiconductor showing the full valence band and empty conduction band. The gap between these is called the band gap [11].

The band gap of a semiconductor is usually classified into two types: direct band gap and indirect band gap, illustrated in figure 2.4. The minimal-energy state in the conduction band as well as the maximal-energy state in the valence band, are each characterized in the Brillouin zone by a certain k-vector. If each of the k-vectors are the same, it is called a "direct gap", otherwise it is called an "indirect gap". In the direct band semiconductors the electron

makes a direct transition from conduction band to valence band emitting a photon. In an indirect semiconductors the electrons make transition from conduction band to valence band passing through intermediate states giving up its energy to the crystal lattice, causing rise in crystal temperature [4].

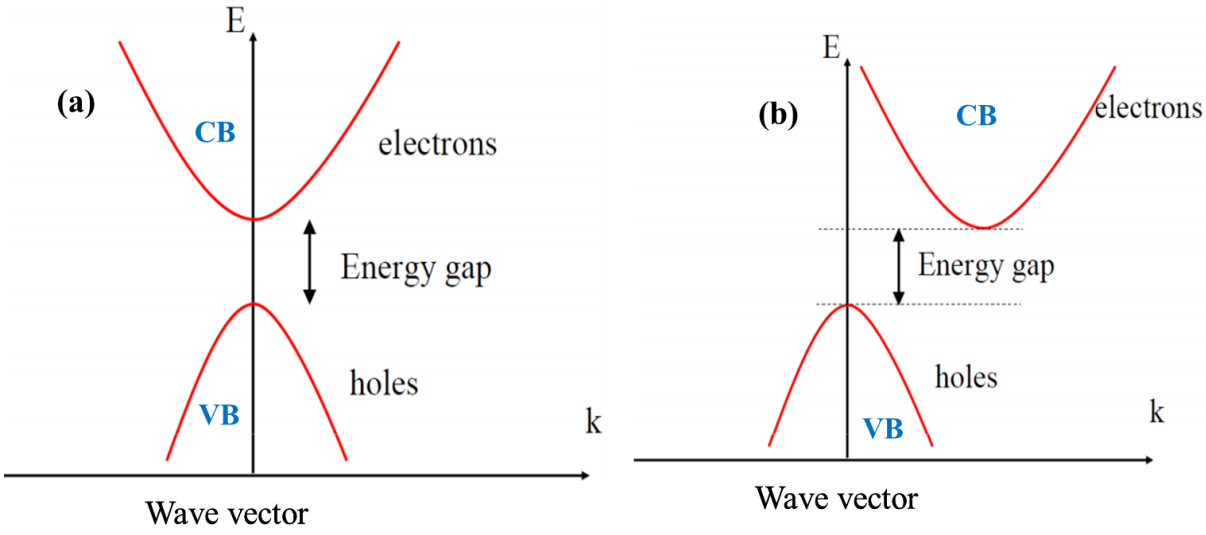

Figure 2.4: Schematic diagrams for: (a) direct band gap and (b) indirect band gap semiconductors.

2.5. Bismuth

The rare earth ions (e.g. Eu, Pr, Yb) are usually added as an activator for luminescence, but the main group metal ions such as Tl^{+}, Pb^{2+}, Bi^{3+} and Sb^{3+} may also be useful luminescence centres [12]. Bismuth is a chemical element with symbol (Bi) and atomic number 83. Bismuth is located in group 15 of the periodic table of elements and it is the heaviest element in this group with an atomic weight of 208.98 amu. Bi atoms have an electronic configuration [Xe] $4f^{14}5d^{10}6s^{2}p^{3}$. Elemental bismuth may occur naturally, although its sulphides and oxides form important commercial ores. The boiling point and melting point of Bi are 1564 °C and 271 °C, respectively. Bi is non-toxic as well as non-radioactive [13]. Bi has a large number of valence states (e.g. +3, +2, +1, 0, -2) in various host materials [14]. The Bi^{3+} trivalent state is normally the most stable valence state [14]. The luminescence properties of Bi^{3+} ions have been studied in different host materials [15]. The ground state of the Bi^{3+} ion, having $6s^{2}$ configuration, is $^{1}S_{0}$ and the excited $6s^{1}6p^{1}$ configuration has four energy levels, namely $^{3}P_{0}$, $^{3}P_{1}$, $^{3}P_{2}$ and $^{1}P_{1}$. The optical transitions from $^{1}S_{0}$ to $^{3}P_{0}$ and $^{3}P_{2}$ are spin forbidden, whereas the transition from $^{1}S_{0}$ to $^{1}P_{1}$ is spin allowed. Mixing of the $^{1}P_{1}$ and $^{3}P_{1}$ levels by spin orbit

coupling makes the $^3P_1$ allowed [15]. Figure 2.5 shows the energy level diagram for the free Bi^{3+}.

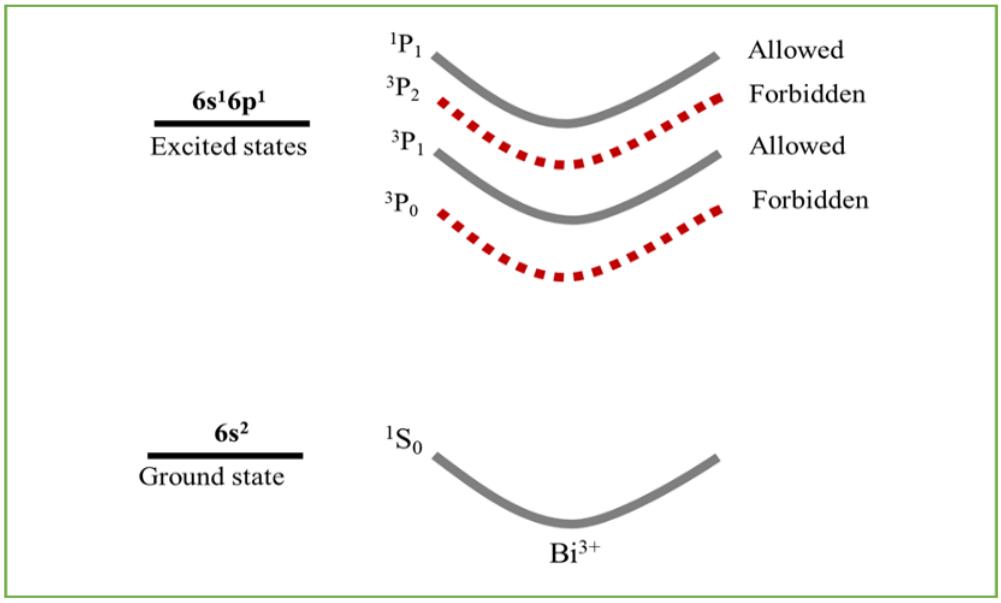

Figure 2.5: Schematic diagram of the energy levels of the Bi^{3+} ion.

Luminescent materials activated by Bi ions exhibit interesting optical properties due to a strong interaction with the surrounding host lattice and the large number of valence states. That is due to the outer electron orbitals of Bi ions are not shielded from the surrounding environment [16]. For instance, luminescent materials doped with Bi^{3+} ions emit in the near ultraviolet and blue region as well as green regions. Bi^{2+} ions emit orange-red light. The Bi^+ ion or Bi^0 emits broadband near infrared in the range from 1000 to 1600 nm. The Bi_5^{3+} cluster emits broadband near to mid infrared in the range from 1000 to 3000 nm [17]. In all cases, the emission regions of these ions varied with variation of the host materials [15]. In this research study, the main focus of investigations is the spectroscopic property of Bi^{3+} as a dopant in phosphor materials.

2.6. Lanthanum oxide (La_2O_3) and lanthanum oxysulphide (La_2O_2S)

Generally, a good host for luminescent ions must exhibit some special properties, such as to be transparent for visible and infrared light and, among others, to have a good chemical and structural stability. Lanthanum oxide (La_2O_3) has attracted much research interest because of its prospect as catalytic materials and for thermal, chemical, electrical, magnetic, ceramic and optical applications [18]. Lanthanum oxide is recognized as a relatively low-cost material compared to other rare earth oxides (Lu_2O_3, Gd_2O_3, etc.) and an excellent host lattice for

luminescent materials [19]. La_2O_3 among rare earth oxides has the largest band gap of 4.3 eV [1], besides the lowest lattice energy, with high dielectric constant (approximately 27) [18]. La_2O_3 has p-type semiconductor properties. Its resistivity decreases when the temperature increasing and it has an average room temperature resistivity of 10 kΩ·cm [20]. La_2O_3 is very sensitive to atmospheric conditions: it can react relatively quickly with the water and carbon dioxide of the atmosphere to form new stable hydroxide and carbonate phases [21].

The lanthanide (La-Lu) oxysulphides have been extensively studied as host materials for phosphors, due to their high chemical stability, high thermal stability, large light absorption properties and wide band gap (4.6-4.8 eV), insolubility in water and high luminescence efficiency [22]. Lanthanum oxysulphide (La_2O_2S) has been extensively studied because of its potential applications for luminescent devices, high-performance magnets, catalysts, and other functional materials based on the optical, electronic, magnetic, and chemical characteristics. [23]. La_2O_2S with high chemical stability and high thermal stability is known as an excellent host material for luminescence applications [24]. It is a semiconductor material [25] with a wide band gap of 4.6 eV [26].

The crystal structures of La_2O_3 and La_2O_2S are shown in figure 2.6. Both La_2O_3 and La_2O_2S belong to the hexagonal crystal family (trigonal crystal system) with space group $P\bar{3}m1$ (No. 164) [27]. In La_2O_3 the La^{3+} ions are bonded with seven oxygen atoms, while for La_2O_2S the La3+ ions are bonded to three sulphur atoms and four oxygen atoms [28]. Thus the crystal structure of both La_2O_2S and La_2O_3 are similar and can be described simply by the alternation of the anionic layers of La_2O_3 [29]. This also means that sulphur atoms in La_2O_2S replace three of the seven oxygen sites in the La_2O_3 structure.

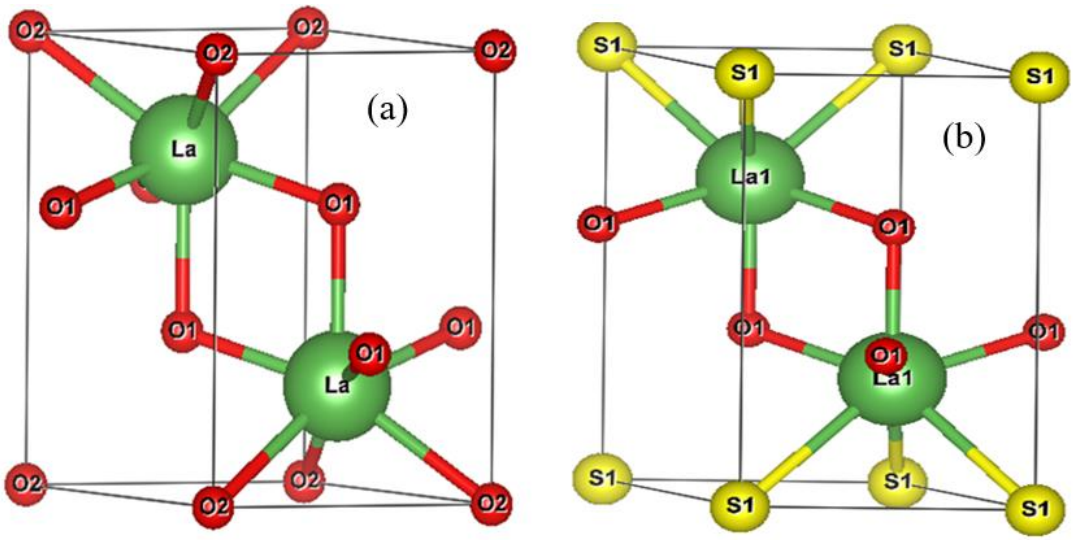

Figure 2.6: The unit cell of (a) La_2O_3 and (b) La_2O_2S drawn with the Vesta software [30].

Lanthanum oxide has many potential uses and applications e.g. to develop ferroelectric materials, such as La-doped $Bi_4Ti_3O_{12}$ and $(Pb_xZr_{1-x})TiO_3$, which represent new materials for non-volatile ferroelectric memories [31]. In optical materials La_2O_3 is often used to dope optical glasses to improve their refractive index, chemical durability and mechanical strength. The presence of the La_2O_3 in the melt glass leads to increasing transition temperature of the glass from 658 °C to 679 °C [32]. The addition also leads to a higher value of density, micro hardness, and refractive index of the glass. La_2O_3 with oxides of tantalum, tungsten and thorium improves the resistance of the glass from attack by alkali. La_2O_3 is widely used as piezoelectric, galvanothermy and thermoelectric materials and also as an important catalyst support in automobile exhaust-gas convectors [33]. La_2O_3 is used to produce phosphors for X-ray imaging intensifying screens and also used in dielectric and conductive ceramics [20]. In addition, various optical applications of La_2O_3 are in infrared-transmitting glass ceramics and as an additive to various transparent ceramic laser materials to improve their optical properties [34]. Furthermore, La_2O_3-based glasses have been considered as an ideal material for broadband optical fibre amplifiers. Luminescent materials formed by doping La_2O_3 have many potential applications in cathode ray tubes, field emission displays, plasma display panels, and vacuum fluorescent display devices [35]. Lanthanum oxysulphide has significant applications such as for television picture tubes, up-conversion phosphors, catalysts, oxygen storage and solid-state lasers [26].

2.7. Preparation methods of phosphors

2.7.1. Sol-gel combustion method

The novelty of the sol-gel combustion synthesis is that it uses a unique combination method of the chemical sol-gel process and combustion which requires relatively simple equipment and produces samples in a short amount of time [36]. Synthesis of ceramic oxides via the sol-gel provides in a single step a product with high purity, good homogeneity, high surface area and low processing temperature [37]. The sol-gel combustion synthesis is based on the gelling and subsequent combustion of an aqueous solution containing a nitrate of the desired metals and an organic fuel (citric acid) and it yields a voluminous and fluffy product with a large surface area [35]. Figure 2.7 is a schematic diagram for the preparation of La_2O_3:Bi powders by the citric acid sol-gel combustion process. A brief, good description of the process is given by [38]: In the citric acid sol–gel combustion method, the raw materials, which are usually a nitrate compound and a fuel (citric acid), are dissolved in water. The mixed solution is then heated to convert the sol into a high-viscosity gel. Increasing the temperature of the gel causes an exothermic combustion process to occur. After completion of combustion, the colour of the resulting powder was brown, which suggests that it contained some residual carbon due to the incomplete combustion of citric acid [39]. Annealing the resulting brown powder at different temperatures between 800 °C and 1400 °C produced the final product (white powder), since the carbon impurity can be oxidized above 600 °C [39] and released as gaseous CO_2.

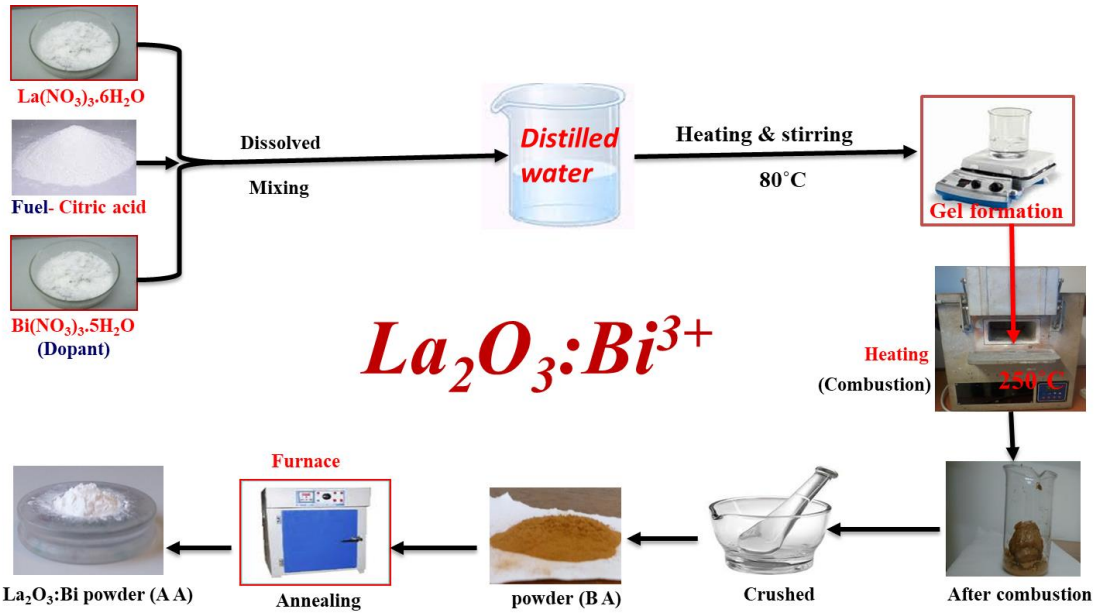

Figure 2.7: Schematic diagram for preparation of La_2O_3:Bi powders by the citric acid sol-gel combustion method.

2.7.2. Ethanol-assisted solution combustion (EASC) method

The ethanol-assistant solution combustion (EASC) method is an efficient route to synthesize nanocrystalline materials due to its advantages such as low process temperature, low-cost method, and reduced time consumption. The EASC method is based on the interaction between rare earth nitrate and organic fuel thiourea (NH_2CSNH) or thioacetamide (CH_3CSNH_2). In the EASC method the raw materials are dissolved in an ethanol–water solution medium. The ethanol, used as an assistant fuel, could dissolve rare earth nitrates and inexpensive thioacetamide organic fuel was used as a source of sulphur. Moreover, during heating ethanol is ignited in the first instance, which leads to a combustion decomposition reaction between the rare earth nitrate and organic fuel and rare earth oxysulphide formed rapidly [40]. Figure 2.8 is a schematic diagram for the preparation of La_2O_2S:Bi powders by the EASC method.

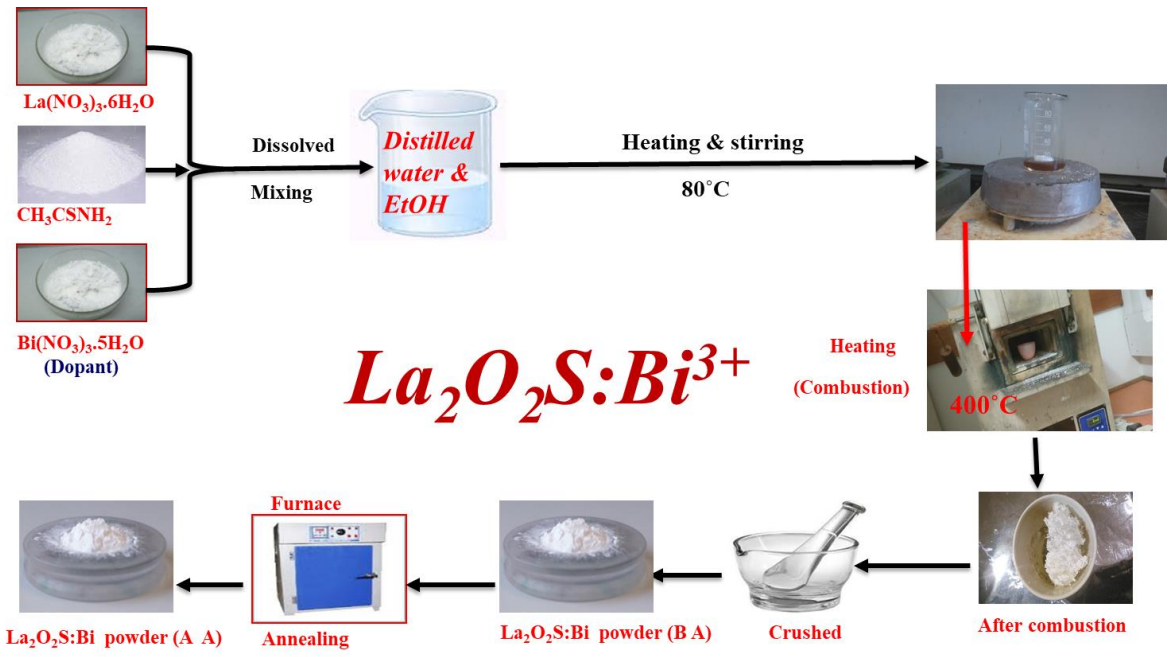

Figure 2.8: Schematic diagram for the preparation of La_2O_2S:Bi powders by the ethanol-assistant solution combustion method.

2.8. References

1. V. Đorđević, Ž. Antić, M.G. Nikolić, M.D. Dramićanin. The Concentration Quenching of Photoluminescence in Eu^{3+}-Doped La_2O_3. *Journal of Research in Physics* 37 (2013) 47–54. https://doi.org/10.2478/jrp-2013-0005

2. H.A.A. Seed Ahmed, *Luminescence from lanthanide ions and the effect of co-doping in silica and other hosts*, PhD thesis, University of the Free State, Bloemfontein, South Africa, 2012.

3. S.R. Rotman, Wide-Gap Luminescent Materials: Theory and Application. Kluwer Academic, Dordrecht (1997). ISBN 978-1-4615-4100-4

4. William M. Yen, Shigeo Shionoya, Hajime Yamamoto. Phosphor Handbook. 2nd Edition. CRC Press, Boca Raton (2007). ISBN: 0-8493-3564-7

5. C. R. Ronda, T. Jüstel, H. Nikol. Rare Earth Phosphors: Fundamentals and Applications. *Journal of Alloys and Compounds* 275–277 (1998) 669–676. https://doi.org/10.1016/S0925-8388(98)00416-2

6. G. Balachandran. Extraction of Rare Earths for Advanced Applications. *Treatise on Process Metallurgy* 3 (2014) 1291-1340. https://doi.org/10.1016/B978-0-08-096988-6.09983-1

7. K.V.R. Murthy, Hardev Singh Virk. Luminescence Phenomena: An Introduction. *Defect and Diffusion Forum* 347 (2013) 1–34. https://doi.org/10.4028/www.scientific.net/DDF.347.1.

8. Photoluminescence, Available from http://www.renishaw.com/en/photoluminescence-explained--25809 (Accessed 11 June 2018).

9. Ashiq Hussain Khalid, Konstantinos Kontis. Thermographic Phosphors for High Temperature Measurements: Principles, Current State of the Art and Recent Applications. *Sensors* 8 (2008) 5673–5744. https://doi.org/10.3390/s8095673

10. José C.S. Costa, Ricardo J.S. Taveira, Carlos F.R.A.C. Lima, Adélio Mendes, Luís M.N.B.F. Santos. Optical Band Gaps of Organic Semiconductor Materials. *Optical Materials* 58 (2016) 51–60. https://doi.org/10.1016/j.optmat.2016.03.041

11. S.O. Kasap. Principles of electronic materials and devices. 3rd Edition, McGraw Hill, New York (2006) 302. ISBN: 0-07-295791-3

12. G. Blasse, A. Bril. Investigations on Bi^{3+} Activated Phosphors. *The Journal of Chemical Physics* 48 (1968) 217–222. https://doi.org/10.1063/1.1667905

13. Ram Mohan. Green Bismuth. *Nature* 2 (2010) 336 (1 page). https://doi.org/10.1038/nchem.609

14. A. Yousif, R. M. Jafer, S. Som, M.M. Duvenhage, E. Coetsee, H.C. Swart. Ultra-Broadband Luminescent from a Bi Doped CaO Matrix. *RSC Advances* 5 (2015) 54115–54122. https://doi.org/10.1039/c5ra09246a

15. Roy H.P. Awater, Pieter Dorenbos. The Bi^{3+} 6s and 6p Electron Binding Energies in Relation to the Chemical Environment of Inorganic Compounds. *Journal of Luminescence* 184 (2017) 221–231. https://doi.org/10.1016/j.jlumin.2016.12.021

16. W.A.I. Tabaza, H.C. Swart, R.E. Kroon. Optical properties of Bi and energy transfer from Bi to Tb in $MgAl_2O_4$ phosphor. *Journal of Luminescence* 148 (2014) 192-197. https://doi.org/10.1016/j.jlumin.2013.12.018

17. Renping Cao, Fangteng Zhang, Chenxing Liao, Jianrong Qiu. Yellow-to-Orange Emission from Bi^{2+}-doped RF_2 (R = Ca and Sr) Phosphors. *Optics Express* 21 (2013) 15728. https://doi.org/10.1016/10.1364/OE.21.015728

18. Xing Wang, Hongxia Liu, Lu Zhao, Chenxi Fei, Xingyao Feng, Shupeng Chen, Yongte Wang. Structural Properties Characterized by the Film Thickness and Annealing Temperature for La_2O_3 Films Grown by Atomic Layer Deposition. *Nanoscale Research Letters* 12 (2017) 233 (7 pages). https://doi.org/10.1186/s11671-017-2018-8

19. M. Méndez, J.J. Carvajal, L.F. Marsal, P. Salagre, M. Aguiló, F. Díaz, P. Formentín, J. Pallarès, Y. Cesteros. Effect of the $La(OH)_3$ Preparation Method on the Surface and Rehydroxylation Properties of Resulting La_2O_3 Nanoparticles. *Journal of Nanoparticle Research* 15 (2013) 1479 (16 pages). https://doi.org/10.1007/s11051-013-1479-7

20. A. Bahari, A. Anasari, Z. Rahmani. Low Temperature Synthesis of La_2O_3 and CrO_2 by Sol–Gel Process. *Journal of Engineering and Technology Research* 3 (2011) 203–208. http://www.academicjournals.org/journal/JETR/article-abstract/642383112607

21. T. Levan, M. Che, J.M. Tatibouet, M. Kermarec. Infrared Study of the Formation and Stability of $La_2O_2CO_3$ During the Oxidative Coupling of Methane on La_2O_3. *Journal of Catalysis* 142 (1993) 18–26. https://doi.org/10.1006/jcat.1993.1185

22. Yanhua Song, Hongpeng You, Yeju Huang, Mei Yang, Yuhua Zheng, Lihui Zhang, Ning Guo. Highly Uniform and Monodisperse $Gd_2O_2S:Ln^{3+}$ (Ln=Eu,Tb) Submicrospheres: Solvothermal Synthesis and Luminescence Properties. *Inorganic Chemistry* 49 (2010) 11499–11504. https://doi.org/10.1021/ic101608b

23. Takayuki Hirai, Takuya Orikoshi. Preparation of yttrium oxysulfide phosphor nanoparticles with infrared-to-green and -blue upconversion emission using an emulsion liquid membrane system. *Journal of Colloid and Interface Science* 273 (2004) 470–477. https://doi.org/10.1016/j.jcis.2003.12.013

24. Guicheng Jiang, Xiantao Wei, Yonghu Chen, Changkui Duan, Min Yin, Bin Yang, Wenwu Cao. Luminescent $La_2O_2S:Eu^{3+}$ nanoparticles as Non-Contact Optical Temperature Sensor in Physiological Temperature Range. *Materials Letters* 143 (2015) 98–100.

https://doi.org/10.1016/j.matlet.2014.12.057

25. R. Vali. Electronic, Dynamical, and Dielectric Properties of Lanthanum Oxysulfide. *Computational Materials Science* 37 (2006) 300–305. https://doi.org/10.1016/j.commatsci.2005.08.007

26. Jingbao Lian, Bingxin Wang, Ping Liang, Feng Liu, Xuejiao Wang. Fabrication and Luminescent Properties of $La_2O_2S:Eu^{3+}$ translucent Ceramic by Pressureless Reaction Sintering. *Optical Materials* 36 (2014) 1049–1053. https://doi.org/10.1016/j.optmat.2014.01.024

27. M. Méndez, J.J. Carvajal, Y. Cesteros, M. Aguiló, F. Díaz, A. Gigure, D. Drouin, E. Martínez-Ferrero, P. Salagre, P. Formentín, *et al*. Sol-Gel Pechini Synthesis and Optical Spectroscopy of Nanocrystalline La_2O_3 doped with Eu^{3+}. *Optical Materials* 32 (2010) 1686–1692. https://doi.org/10.1016/j.optmat.2010.02.018

28. Xiao Yan, George R. Fern, Robert Withnall, Jack Silver. Effects of the Host Lattice and Doping Concentration on the Colour of Tb^{3+}cation Emission in $Y_2O_2S:Tb^{3+}$and $Gd_2O_2S:Tb^{3+}$nanometer Sized Phosphor Particles. *Nanoscale* 5 (2013) 8640–8646. https://doi.org/10.1039/c3nr01034a

29. Guodong Liu, Qinghong Zhang, Hongzhi Wang, Yaogang Li. A Reddish La_2O_2S-Based Long-Afterglow Phosphor with Effective Absorption in the Visible Light Region. *Materials Science and Engineering B: Solid-State Materials for Advanced Technology* 177 (2012) 316–320. https://doi.org/10.1016/j.mseb.2011.12.045

30. Koichi Momma and Fujio Izumi. VESTA 3 for Three-Dimensional Visualization of Crystal, Volumetric and Morphology Data. *Journal of Applied Crystallography* 44 (2011) 1272–1276. https://doi.org/10.1107/S0021889811038970

31. L. Armelao, M. Pascolini, G. Bottaro, G. Bruno, M.M. Giangregorio, M. Losurdo, G. Malandrino, R. Lo Nigro, M E Fragala. Microstructural and Optical Properties Modifications Induced by Plasma and Annealing Treatments of Lanthanum Oxide Sol - Gel Thin Films. *The Journal of Physical Chemistry C* 113 (2009) 2911–2918. DOI: 10.1021/jp809824e

32. N. N. Vinogradova, L. N. Dmitruk and O. B. Petrova. Glass Transition and Crystallization of Glasses Based on Rare-Earth Borates. *Glass Physics and Chemistry* 30 (2004) 1–5. https://doi.org/10.1023/B:GPAC.0000016391.83527.44

33. Jieming Cao, Hongmei Ji, Jinsong Liu, Mingbo Zheng, Xin Chang, Xianjia Ma, Aimin Zhang, Qinhua Xu. Controllable Syntheses of Hexagonal and Lamellar Mesostructured Lanthanum Oxide. *Materials Letters* 59 (2005) 408–411. https://doi.org/10.1016/j.matlet.2004.09.034

34. Jian Zhang, Liqiong An, Min Liu, Shunzo Shimai, Shiwei Wang, Lidong Chen. The Fabrication and Optical Spectroscopic Properties of Rare Earth Doped Y_2O_3 Transparent Ceramics. *Ceramics* 24 (2007) 681–684

35. Lixin Song, Pingfan Du, Jie Xiong, Xiaona Fan, Yuxue Jiao. Preparation and Luminescence Properties of Terbium-Doped Lanthanum Oxide Nanofibers by Electrospinning. *Journal of Luminescence* 132 (2012) 171–174. https://doi.org/10.1016/j.jlumin.2011.08.007

36. Chi-Hwan Han, Hak Soo Lee, and Sang Do Han. Synthesis of Nanocrystalline TiO2by Sol-Gel Combustion Hybrid Method and Its Application to Dye Solar Cells. *Bulletin of the Korean Chemical Society* 29 (2008) 1495–1498. https://doi.org/10.5012/bkcs.2008.29.8.1495

37. Yingchao Han, Shipu Li, Xinyu Wang, Xiaoming Chen. Synthesis and Sintering of Nanocrystalline Hydroxyapatite Powders by Gelatin-Based Precipitation Method. *Materials Research Bulletin* 39 (2004) 25–32. https://doi.org/10.1016/j.ceramint.2005.09.001

38. A. Khorsand Zak, M. Ebrahimizadeh Abrishami, W. H Abd Majid, Ramin Yousefi, S. M. Hosseini. Effects of Annealing Temperature on Some Structural and Optical Properties of ZnO Nanoparticles Prepared by a Modified Sol-Gel Combustion Method. *Ceramics International* 37 (2011) 393–398. https://doi.org/10.1016/j.ceramint.2010.08.017

39. Karim Khan, Ayesha Khan Tareen, Sayed Elshahat, Ashish Yadav,Usman Khan, Minghui Yang, Luigi Bibbò and Zhengbiao Ouyang. Facile synthesis of a cationic-doped $[Ca_{24}Al_{28}O_{64}]^{4+}(4e-)$ composite via a rapid citrate sol–gel method. Dalton Transactions 47 (2018) 3819-3830. https://doi.org/10.1016/10.1039/c7dt04543c

40. Xi-xian Luo, and Wang-he Cao. Ethanol-Assistant Solution Combustion Method to Prepare La_2O_2S:Yb,Pr Nanometer Phosphor. *Journal of Alloys and Compounds* 460 (2008) 529–534. https://doi.org/10.1016/j.jallcom.2007.06.011

Chapter 3

Theory of characterization techniques

3.1. Introduction

This chapter is a brief description of different techniques of research used to characterize the presented powder phosphors. These techniques include:

1. X-ray diffraction (XRD) - to determine the crystalline structure and the phase quality of prepared samples and to estimate the crystallite size;
2. Scanning electron microscopy (SEM) - to determine the surface morphology;
3. Energy dispersive spectroscopy (EDS) - to determine the chemical composition of the samples;
4. Ultraviolet–visible spectroscopy (UV-vis) and diffuse reflectance spectroscopy (DRS) - to detect the absorption wavelengths and the bandgap of materials;
5. Fourier transform infrared spectroscopy (FTIR) – to determine the vibration modes in order to identify impurities;
6. Photoluminescence spectroscopy (PL) - to determine the excitation, emission and lifetime luminescence properties;
7. Auger electron spectroscopy (AES) - to determine the elemental composition of the sample surface;
8. Cathodoluminescence spectroscopy (CL) - to determine the light emission of samples when exposed to an electron beam;
9. X-ray photoelectron spectroscopy (XPS) - to investigate the atoms in the surface of samples and identify their oxidation states.

3.2. X-ray diffraction (XRD)

The discovery of X-rays was by the German physicist Wilhelm Conrad Roentgen at the University of Würzburg in 1895 [1]. X-rays are a form of electromagnetic radiation in the range between gamma rays and ultraviolet rays and which have a wavelength ranging from 0.1 up to 10 nm in the electromagnetic spectrum [2]. X-rays have the ability to penetrate into solid substances and yield information about their internal crystalline structure.

XRD is a technique that can be used for identification of the degree of crystallinity, analysis of lattice parameters, phase identification and crystallite size determination [3]. The basic principles of this technique consist in the interaction between a projected X-ray beam and target substances. The diffractometer for XRD is made up of three main elements: an X-ray source, a sample stage and an X-ray detector [3] as presented in figure 3.1.

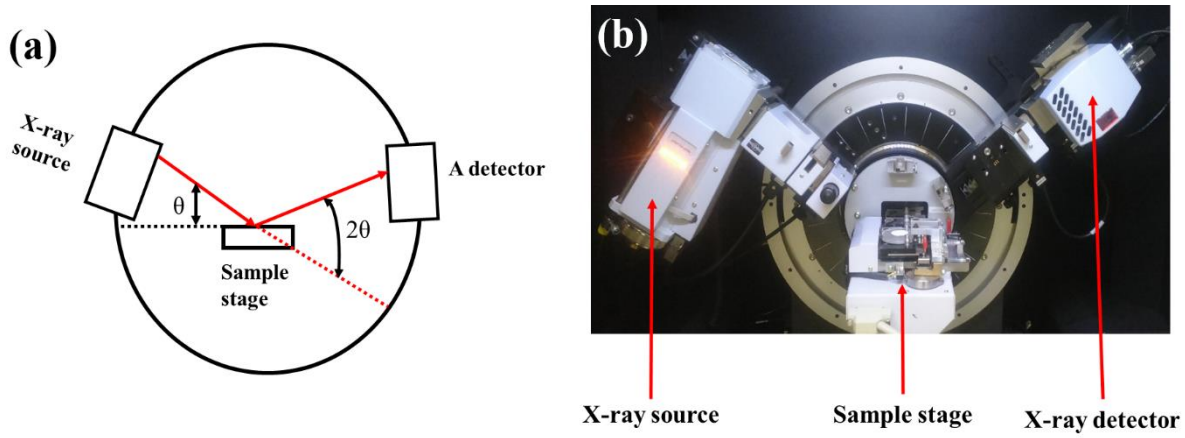

Figure 3.1: The X-ray diffractometer (a) diagrammatic representation (b) Photograph of a commercial system.

The X-rays are generated in a cathode ray tube (X-ray source) by heating a filament to produce electrons, which are accelerated toward a target material (sample stage). When the incident electrons interact with the electrons in a core shell of the target material, characteristic X-rays will be emitted. The characteristic spectrum consists of various components e.g. Kα and Kβ are the most common components with a specific characteristic wavelength. The most common material used as a target is Cu. The wavelength (**λ**) of Cu Kα radiation is 0.15406 nm. A monochromator is often used to select a single wavelength from X-ray spectra. A nickel (Ni) β-filter is used for this purpose. Ni can absorbs X-rays below 0.15 nm and can be used to filter the Kβ X-rays from Cu [3], as shown in figure 3.2.

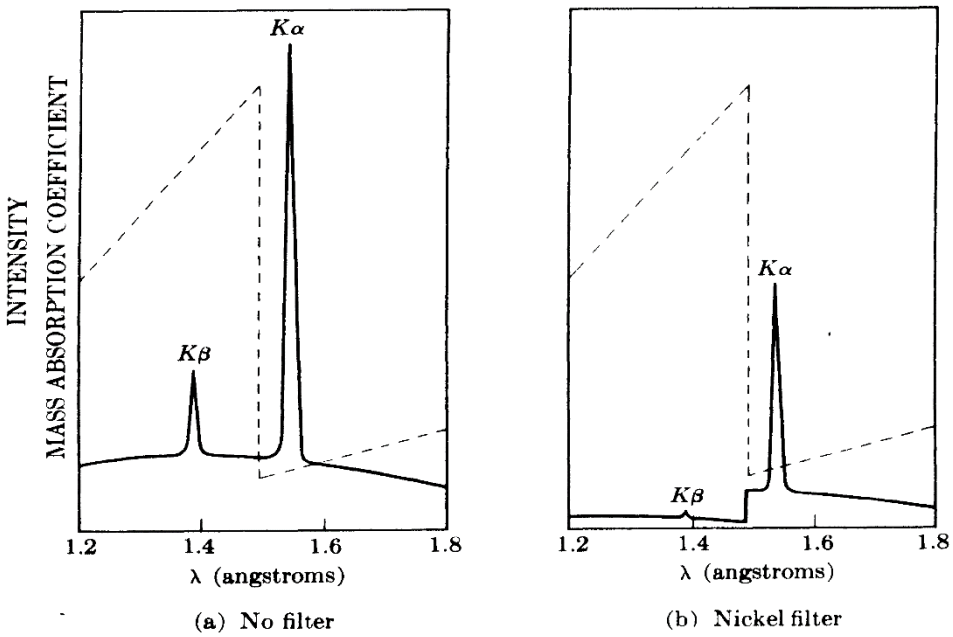

Figure 3.2: Copper radiation (a) before and (b) after passage through a nickel filter [4].

The interaction of incident X-rays with crystalline material produces constructive interference, and some incident beam is diffracted by the crystalline phases of the material when the condition for Bragg's law is satisfied, as presented in figure 3.3. The parallel X-rays are projected onto crystal planes at an angle θ. The crystal planes diffract the rays and constructive interference occurs when the difference in the path is equal to a whole number of wavelengths. Bragg equation is given by:

$$n\lambda = 2d \sin\theta \quad \ldots\ldots\ldots\ldots\ldots\ldots\ldots\ldots \quad (3.1)$$

where n is an integer that indicates the order of the reflection, θ is Bragg angle and d is the inter-planar distance. If the X-ray wavelength is known, the inter-planar distance can be obtained by measuring the Bragg angle [5].

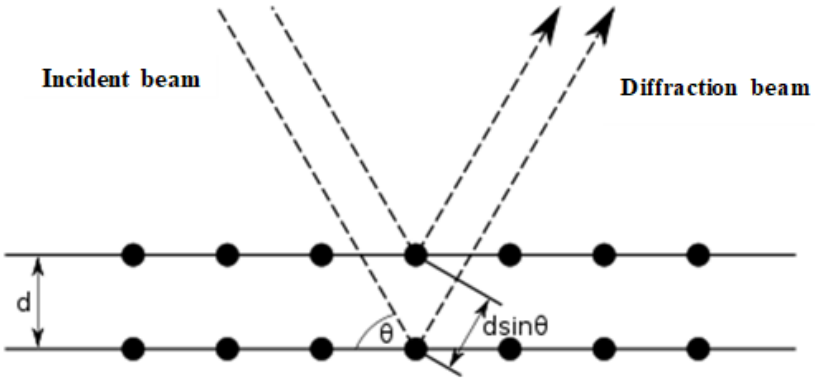

Figure 3.3: Schematic diagram showing the diffraction of X-rays from atoms and Bragg's law [6].

There is a relationship between Miller indexes (*hkl*) and lattice parameters for each reflection plane and the inter-planar distance (d_{hkl}). For example, for cubic structures with a lattice parameter *a*, it can be formulated as [7]

$$d_{hkl} = \frac{a}{\sqrt{h^2+k^2+l^2}} \quad \ldots\ldots\ldots\ldots\ldots\ldots\ldots\ldots\ldots (3.2)$$

The crystallite size, *D*, can be estimated from the broadened peaks of the XRD spectra by using the Scherrer equation:

$$D = \frac{K\lambda}{\beta cos\theta} \quad \ldots\ldots\ldots\ldots\ldots\ldots\ldots\ldots\ldots\ldots (3.3)$$

where λ is the X-ray wavelength, β is the full width at half maximum (FWHM) of a diffraction peak, θ is the Bragg angle and *K* is a constant related to crystallite shape, normally taken as 0.9 [7]. The value of β in 2θ axis of diffraction profile should be in radians. The θ can be in radians or degrees, since the cosθ corresponds to the same number.

XRD patterns were collected at the department of Physics of the University of the Free State using a Bruker D8 Advance X-ray diffractometer equipped with a copper anode X-ray tube (figure 3.4). The system was operated using a 40 mA filament current and a generator voltage of 40 kV to accelerate the electrons. Moreover, a nickel filter was used to remove the Cu Kβ X-rays. Measurements were taken with a 2θ step size of 0.02°. It is important to load the samples at the same height, since small peak shifts may occur.

Figure 3.4: The Bruker D8 Advance X-ray diffractometer at the Department of Physics of the University of the Free State.

3.3. Scanning electron microscopy (SEM)

SEM is a technique that can be used for analysing the microstructure and morphology of samples. In this technique, a focused beam of electrons is used to scan the sample surface, providing images of that sample [9]. This provided images to give information about the topography and morphology of the sample [9]. Additional information about elemental composition of the material can be provided too if the system is equipped with an energy dispersive X-ray spectrometer (EDS), which is described in the next section. The principle of the SEM technique is based on the interaction of an incident electron beam with the solid specimen. During SEM measurements, the electron beam is generated from electron gun and then focused and accelerated towards the surface of the sample by electromagnetic lenses and is rastered by pairs of coils in the objective lens over the sample surface. Figure 3.5 shows a simple diagram of scanning electron microscopy. When the beam of electrons hits the sample, different types of electromagnetic waves and electrons are produced from various depths including: secondary electrons, back-scattered electrons, characteristic X-rays, cathodoluminescence, specimen current and transmitted electrons [10]. Figure 3.6 shows the regions from which different signals are detected. Secondary electrons and backscattered electrons are the most important signals that are detected to produce SEM images. Secondary electrons are used principally for topographic contrast in the SEM (i.e., for the visualization

of surface texture and roughness), while backscattered electrons are used for illustrating contrasts in compositions in multiphase samples (i.e. for rapid phase discrimination) [10].

The SEM measurements in this study were performed on a JEOL JSM-7800F scanning electron microscope (figure 3.7) equipped with EDS. The SEM image collection was done with a 5 kV electron beam. Some SEM images were also collected using a PHI 700 nano scanning Auger electron microprobe (NanoSAM) system with a 20 kV electron beam.

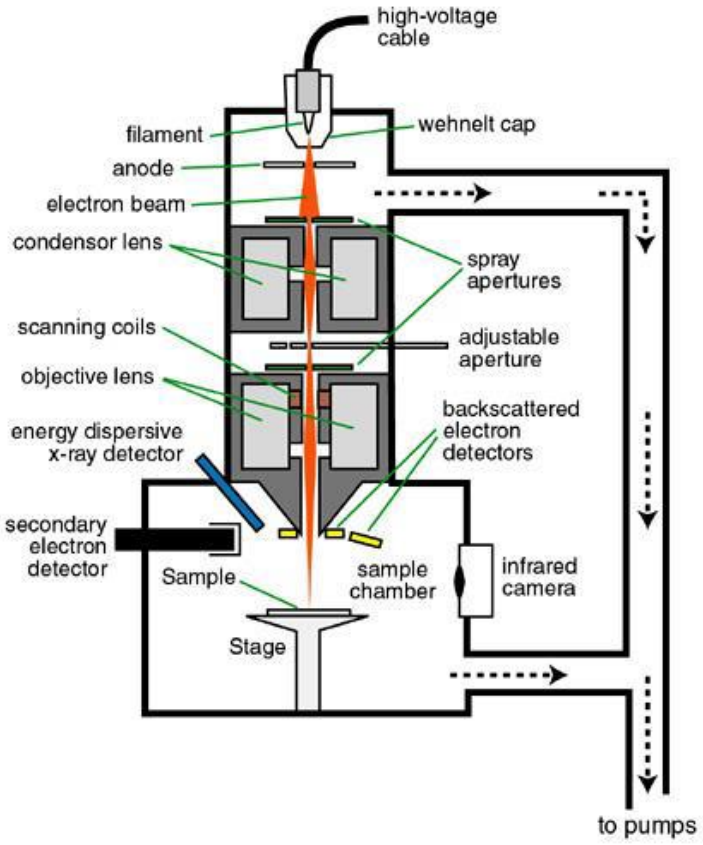

Figure 3.5: Schematic diagram of a typical SEM [11].

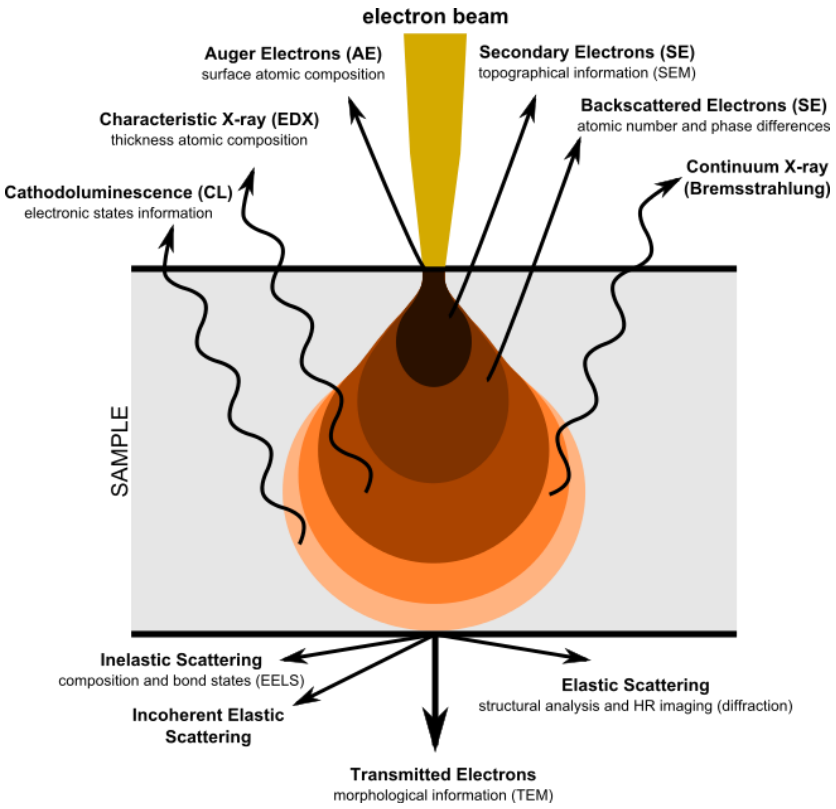

Figure 3.6: The signals produced from electron beam interaction with solid matter [12].

Figure 3.7: JEOL JSM-7800F system at the Centre for Microscopy at University of the Free State.

3.4. Energy dispersive X-ray spectroscopy (EDS)

The EDS is a technique used for chemical microanalysis, it is also used in conjunction with scanning electron microscopy (SEM) to detect the X-rays emitted from material sample as bombarded by an electron beam to characterize the elemental composition of the volume under analysis. Features or phases as small as 1 μm or less can be analyzed [13].

Once the sample is bombarded by the SEM's electron beam, an electron is ejected from the inner shell of the sample atom. The resulting electron holes are filled by electrons from a higher state, and an X-ray is emitted to balance the energy difference between the two electrons' states. The X-ray energy is a characteristic of the element from which it was emitted.

The EDS X-ray detector measures the relative abundance of emitted X-rays versus their energy. The detector is typically a lithium-drifted silicon solid-state device. When an incident X-ray strikes the detector, it creates a charge pulse that is proportional to the energy of the X-ray. The charge pulse is converted to a voltage pulse by a charge-sensitive preamplifier. The signal is then sent to a multichannel analyser where the pulses are sorted by voltage. The energy (as determined from the voltage measurement) for each incident X-ray is sent to a computer for display and further data evaluation. The spectrum of X-ray energy versus counts is evaluated to determine the elemental composition of the sampled volume [14].

In this study the chemical compositions of the powders were obtained using an X-Max^{N}80 detector from Oxford Instruments in the SEM as presented in Figure 3.7.

3.5. Ultraviolet-visible spectroscopy (UV-vis) and diffuse reflectance spectroscopy (DRS)

UV-vis is an optical spectroscopic technique that measures the intensity of light against the wavelength after passing through a sample or reflecting from a sample surface. The UV region ranges from 190 to 400 nm and the visible region from 400 to 800 nm [15]. The technique can provide both quantitative and qualitative information. Figure 3.8 shows an illustrative diagram of a UV-visible spectrometer.

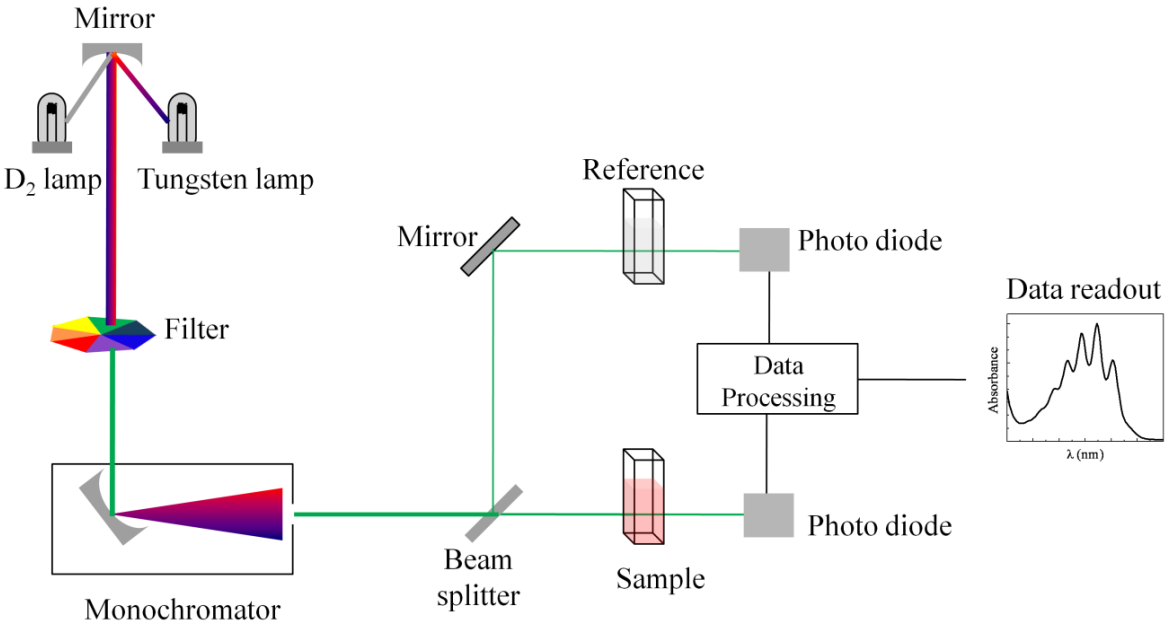

Figure 3.8: Schematic of UV-vis spectrophotometer [16].

In UV-vis the light source for UV measurements is usually a deuterium lamp and for visible measurements it is a tungsten-halogen lamp. The two lamps can cover the range of wavelengths of 200 – 800 nm. The wide range output from the light source is focused onto the diffraction grating to obtain a monochromatic beam, since the incoming light splits into its component colours of different wavelengths, like a prism but more efficiently [15]. Transmission as well as absorption can be measured for liquid samples or transparent solid samples.

For powder samples such as phosphor, the absorption and band gap values can be calculated by using DRS measurements, which is usually used to measure the reflected light from the powder samples. For a DRS measurement, the instrument must be equipped with an integrating sphere coated with a white standard to collect the light reflected by the standard and the sample [17]. During the DRS measurements, the light from the source is split into two beams: one directed to the detector as a reference and the second one directed to the sample. Some of the incident beam is absorbed by the sample and the second part will be diffused and reflected. The sample is positioned inside an integrating sphere that collects the diffusely scattered light by the sample. The collected light eventually reaches the detector, which compares the collected light from the source light to calculate the amount that has been absorbed. The Kubelka-Munk function

$$F(R_\infty) = \frac{(1-R_\infty)^2}{2R_\infty} \quad \ldots\ldots\ldots\ldots\ldots\ldots\ldots\ldots\ldots\ldots\ldots \text{(3.4)}$$

can be used to convert the diffuse reflectance measurements to values proportional to the absorption [18]. For an indirect band gap material such as La_2O_3 a Tauc plot of $[F(R_\infty)h\nu]^{1/2}$ versus $h\nu$ can then be used to determine the optical band gap by fitting a linear region and extrapolating this to where it cuts the horizontal (energy) axis [26].

The Lambda 950 UV–vis spectrophotometer equipped with an integrating sphere that displays reflectance close to 100% reflectance in the wavelength range from near UV to the near infrared was used in this research study to obtain the diffuse reflectance spectra. The standard used was spectralon. Figure 3.9 shows the UV-Vis spectrophotometer used in this study.

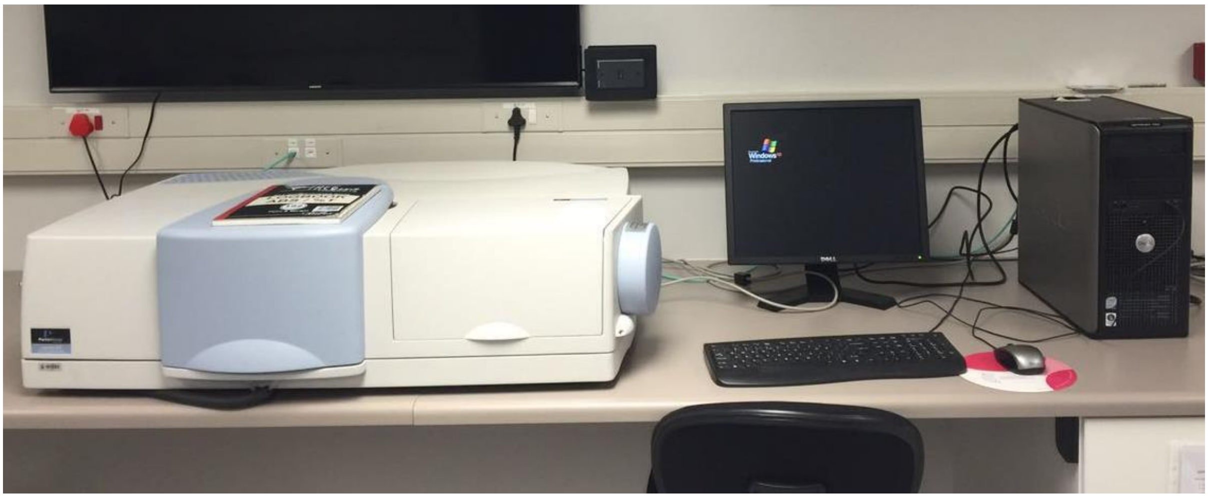

Figure 3.9: PerkinElmer Lambda 950 UV-Vis-IR spectrometer at the Department of Physics, University of the Free State.

3.6. Fourier transform infrared spectroscopy (FTIR)

FTIR is an analytical technique that can be used to identify the functional groups present in organic and inorganic compounds by measuring their absorption of infrared radiation over a range of wavelengths [20]. Infrared radiation is invisible electromagnetic radiation just below the red colour of the visible electromagnetic spectrum, with wavelength range from 700 nm to 1 mm [21].

The FTIR spectrometer consists of infrared source, an interferometer, a sample compartment, a detector and a computer. The source generates infrared radiation. This energy beam passes through a slit which controls the amount of radiation projected to the substance, and finally to the detector. The resulting interferogram signal exits the interferometer and enters the sample compartment. This is where particular frequencies of energy which are uniquely characteristic of the sample are absorbed. The beam passes into the detector for final measurement and the measure signal is digitized and sent to the computer where the Fourier transform takes place. The final infrared spectrum is then presented to the analysis for evaluation.

Powder samples for FTIR can be mixed with potassium bromide (KBr) which is transparent in the infrared to form a fine powder which is then compressed into a thin pellet to be analyzed. The thickness of the pellet and the ratio between the KBr and the powder sample can affect the peak intensity and broadness. It is important to dry the sample properly to avoid broad band signals in the spectrum coming from water. FTIR spectra of the powders in this work were obtained using a Thermo Scientific Nicolet 6700 FT-IR instrument, for which pellets were prepared by mixing 0.002 g of sample with 0.2 g of KBr (heated in a drying oven at 70 °C for 12 h to eliminate moisture).

3.7. Photoluminescence (PL) spectroscopy

PL spectroscopy is a non-destructive analytical technique. In this technique, the material is excited from its ground electronic state to one of its excited electronic states, usually by using a UV light or laser beam. Resulting luminescence is produced when the electrons fall back to the ground electronic state and this can be recorded as a plot of the intensity of emitted light versus wavelength or energy [22]. The technique is usually used to record emission and excitation spectra as well as luminescence lifetimes.

In PL spectroscopy, the incident light is absorbed by a sample and imparts excess energy into the material in a process called *photo-excitation.* The photo-excitation causes the electron to jump from its ground electronic state to one of the various vibrational states in the excited electronic state. Non-radiative relaxation is accompanied with the emission of phonons, allowing the excited electron to lose energy until it reaches the lowest vibrational state of the excited electronic state [23]. When this electron returns to its initial state or to any luminescent centre from which the electron was excited, the excess energy may be released

as emission of photon, hence called a radiative process, or may not for a nonradiative process. The released energy emitted as light (photoluminescence) corresponds to the energy difference between the two electron energy levels of the excited state and the ground state involved in the transition. The quantity of the emitted light is related to the relative contribution of the radiative process. The emitted light, in almost all cases, has less energy relative to the original light from the energy source. Hence, PL spectra always possess a wavelength range that is longer than the wavelength of the excitation source [22]. Figure 3.10 is a schematic diagram of the basic components of a PL spectrophotometer. This consists of the sample exposed to the light for excitation, a monochromator used to select excitation wavelength, and a detector used to observe the luminescence through another monochromator. Usually the angle between the detection of the excitation light and the detector is 90° to prevent the scattered light reaching the detector. The emission spectrum obtained when the excitation wavelength is kept fixed and scans through the emitted radiation [24]. The International Commission for Illumination (CIE) coordinates of the emitted light was calculated using the GoCIE software [25]

The photoluminescence measurements were carried out by using a Cary Eclipse fluorescence spectrophotometer equipped with a 150 W xenon flash lamp as an excitation source, operating in fluorescence mode or phosphorescence mode (figure 3.11 (a)). Other steady-state and lifetime measurements were performed using a FLS980 fluorescence spectrometer from Edinburgh Instruments (figure 3.11(b)).

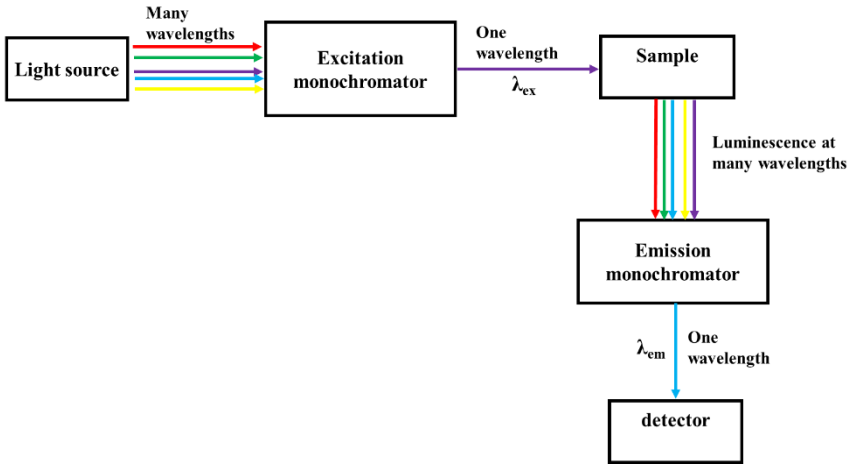

Figure 3.10: Schematic illustration of the basic components of a spectrophotometer.

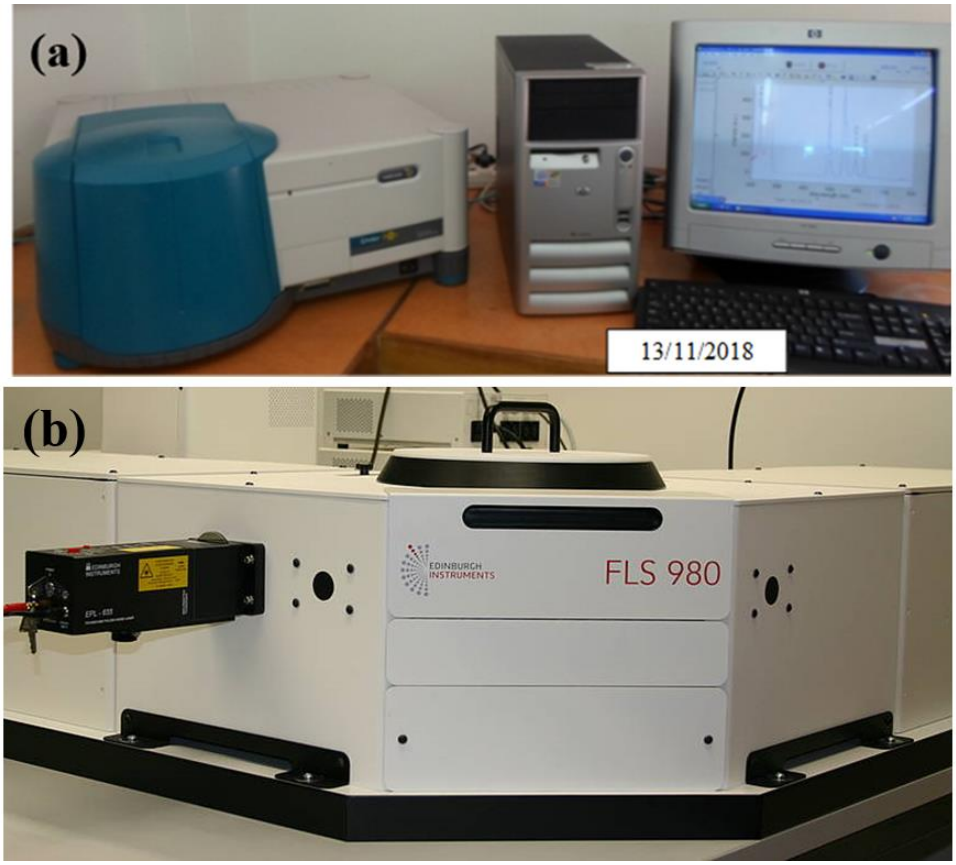

Figure 3.11: (a) Cary Eclipse fluorescence spectrophotometer. (b) FLS980 fluorescence spectrometer, at the Department of Physics, University of the Free State.

3.8. Auger electron spectroscopy (AES)

AES is an analytical technique commonly used to investigate the elemental composition and the chemical state of the atoms on the surface of a solid material. Auger electrons are emitted when a focused electron beam bombards the sample and ejects an electron of the inner shell of the atom. This vacancy must be refilled by an electron from a higher energy level ($L_{2,3}$). When the higher energy electron fills the hole, the release of energy is transferred to an electron in an outer orbit electron. That electron has sufficient energy to overcome the binding energy and the work function to be ejected with a characteristic kinetic energy. The ejected electron is referred to as an Auger electron after Pierre Auger who first discovered it in 1925. Figure 3.12 shows a schematic diagram of an Auger emission process in a solid. Furthermore, the kinetic energy (E_{kin}) of an Auger electron is given by

$$E_{kin} = E_K - E_{L1} - E_{L2,3} - \Phi \quad \ldots\ldots\ldots\ldots\ldots\ldots \quad (3.5)$$

where the symbol K represents the initial state (the ground state), L_1 and $L_{2,3}$ represent the final state transitions and Φ is the work function of the analyser material. Equation 3.5 does not take into account the transition energies between the core holes (K) and double ionized states ($L_{2,3}$). So, for approximation, the following is used to include the transition probability, which was developed by Jenkins and Chung [26].

$$E_{kin} = E_K(Z) - 0.5[E_{L1}(Z) + E_{L1}(Z+1)] - 0.5[E_{L2,3}(Z) + E_{L2,3}(Z+1)] - \Phi \ldots\ldots\ldots (3.6)$$

where Z is the atomic number of the atom involved. AES is a surface sensitive technique. This is due to the relatively short inelastic mean free path for Auger electrons. AES is widely used to provide information about the composition of surfaces of the solid materials. AES can detect all elements except H and He [27]; because the Auger process is a three-electron process these cannot be detected because both have less than three electrons.

AES surface analyses required the sample to be inserted into an ultra-high vacuum (UHV), usually at a base pressure of 10^{-7} Pa or less. The reason is the surface composition should remain unchanged (clean) during the experiment. UHV guarantees the high quality of AES results. AES can be used to determine the depth profile by recording Auger peak to peak height (APPHs) of Auger signals as a function of sputter erosion depth. Surface mapping is also possible by AES.

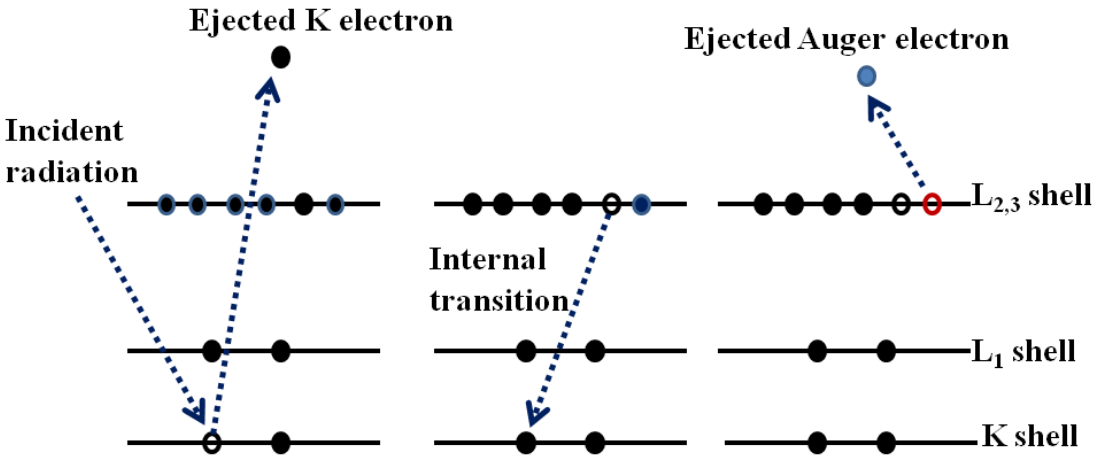

Figure 3.12: Schematic diagram of electron transitions in the case of Auger electron emission.

The Auger measurements in this study were carried out in an UHV chamber at the base pressure of $1.3x10^{-8}$ Torr with a PHI model 549 system (figure 3.13). The powder was irradiated with a beam of electron with energy of 2.5 keV and a beam current of 4 μA. Also a PHI 700 Nano scanning Auger electron microprobe (NanoSAM) with a 20 kV, 1 nA electron beam was used to analyse the surface elemental composition.

Figure 3.13: PHI Model 549 AES unit at the Department of Physics, University of the Free State.

3.9. Cathodoluminescence (CL) spectroscopy

Many materials exhibit the phenomenon of CL, which is the emission of a photon (light) from a specimen when excited by an electron beam. This includes semiconductors, many minerals and some organic compounds. The energy of the emitted photons in CL is typically 0.3 to 6 eV, covering the range of wavelengths from the UV to the near-infrared [28]. CL is the inverse of the photoelectric effect in which electron emission is induced by irradiation with photons [29]. CL is similar to PL but using electrons to excite the substance instead of photons. The most common example of the CL process is the screen of a television cathode ray tube (CRT) monitor.

CL occurs when a material is bombarded by a high energy electron beam. Energy from the incident electron is absorbed by the materials causing electrons to be excited from the ground state (valence band) to the higher electronic state (conduction band), leaving a hole in the valence band. When this electron returns to its valence band (direct band to band

recombination) or other luminescent centres (activator ions or structural defects), energy may be released in form of photons (light). The energy of the photon and the probability that a photon will be emitted or not depend on the material, its purity and its defect state. Any non-metallic material or semiconductors can be examined in this case. In terms of band structure, classical semiconductors, insulators, ceramics, gemstones, minerals, and glasses can be treated as well. Figure 3.17 shows the process causing cathodoluminescence emission.

In this study, an Ocean Optics PC2000 spectrometer attached with PHI model 549 AES was used to collect the CL data. OOI Base32 computer software was utilized to record and plot the data. The CL measurements were carried out by using an electron beam which had a working voltage of 2.5 keV and a beam current of 4 μA.

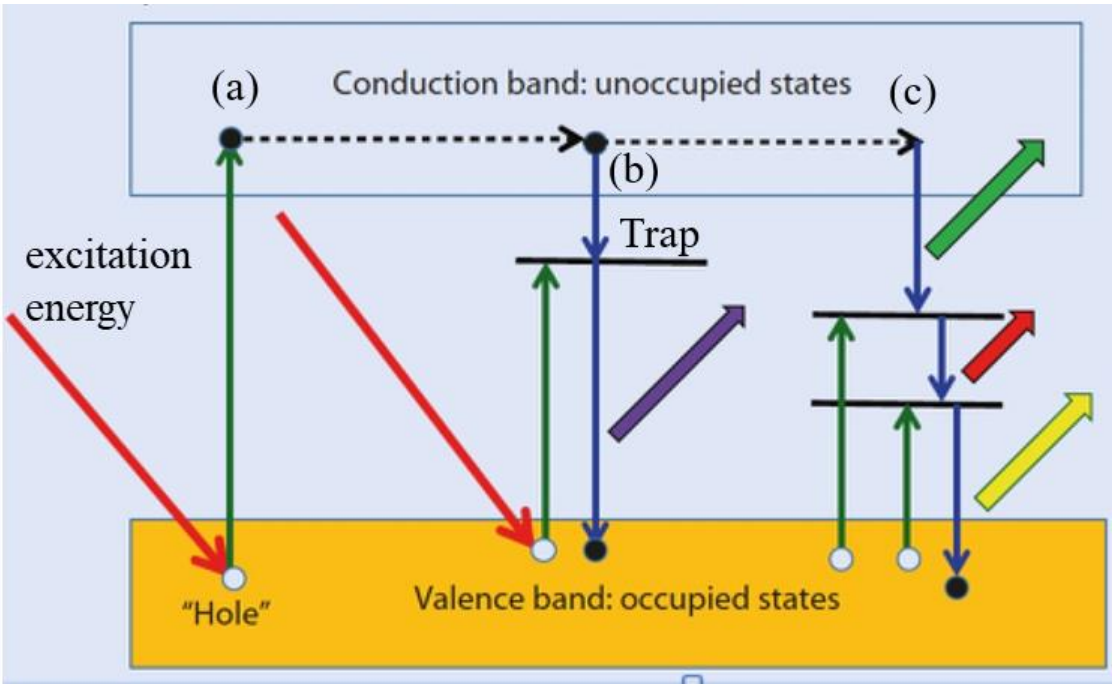

Figure 3.17: CL mechanisms due to the recombination processes in insulators or semiconductors: (a) recombination by direct band-to-band transition, (b) structural defects states in the forbidden gap and (c) the impurity energy levels [30].

3.10. X-ray photoelectron spectroscopy (XPS)

XPS, also popularly known as electron spectroscopy for chemical analysis (ESCA), is a surface-sensitive quantitative spectroscopic technique widely used to investigate the chemical composition of the surface of the material. XPS provides a total elemental analysis, except for hydrogen and helium. Furthermore, XPS provides a quantitative elemental analysis of the top

1-20 nm of solid surface. Information about chemical bonding and molecular orientation can also be obtained [31]. The XPS method, shown schematically in Figure 3.18, is based on Einstein's classic explanation of the photoelectric effect. As shown in figure 3.19, when a material surface is bombarded by an X-ray photon having energy $h\nu$ (where h is Planck's constant and ν is the frequency), this may be absorbed by an electron from a core level which is therefore ejected from the atom. The emitted electron should overcome the binding energy (BE) of the orbital in which it was located in the atom before leaving the surface of the material. The amount of remaining incident radiation energy determines the kinetic energy (KE) of the ejected electron. Thus the binding energy of the electron can be identified from the energy of the incident radiation and the kinetic energy of the electron, the binding energy identifies the elements present and the oxidation state of that element. The energy of the emitted electron, which is characteristic of the atom from which the electron originated and its environment, is measured by a hemispherical electron analyser. The KE of the ejected electron is given by

$$\mathrm{KE} = h\nu - \mathrm{BE} - \Phi \quad \ldots\ldots\ldots\ldots\ldots\ldots \quad (3.7)$$

where Φ is the spectrometer work function. XPS is considered as a surface sensitive analytical technique; due to the very short path of the photoelectrons excited from the material, only the electrons that are generated from the top few atomic layers of the surface can reach the detector. Monochromatic X-rays are used as excitation sources. The most commonly used X-ray sources are Mg Kα, and Al Kα [32]. X-ray photoelectron spectroscopy must be performed under ultrahigh vacuum conditions (greater than $1\text{x}10^{-8}$ Torr) in order to prevent scattering of photoelectrons and to minimize contamination of the sample surface.

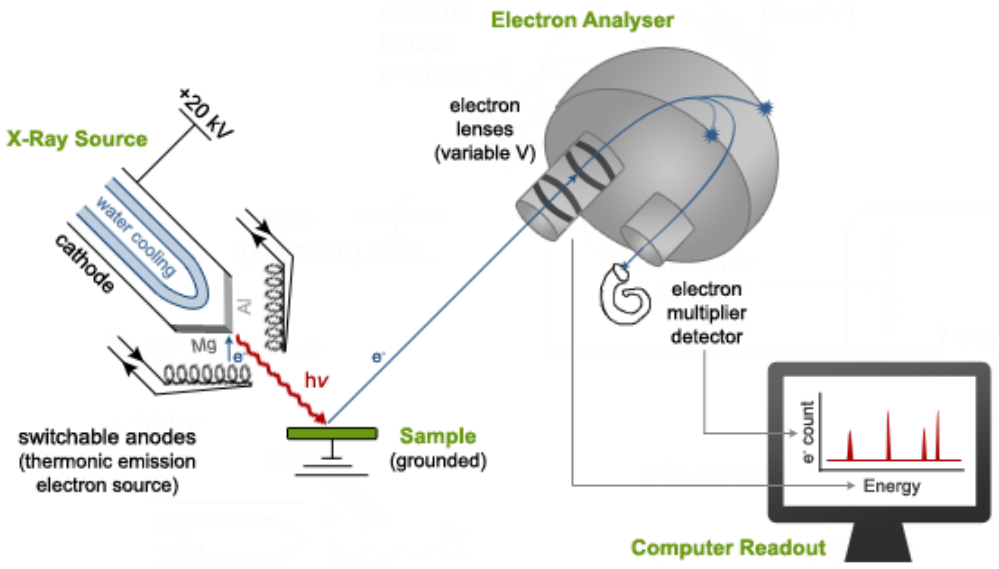

Figure 3.18: Schematic diagram of an XPS system [33].

The XPS measurements in this study were performed on a PHI 5000 Versaprobe-scanning ESCA microprobe shown in figure 3.20. The XPS surveys were done with a 100 µm diameter monochromatic Al Kα X-ray beam generated by a 25 W, 15 kV electron beam. The depth profile and sputtering were done with 2 kV, 2 µA 1×1 mm raster-Ar ion gun of sputtering rate of about 14 nm/min. For high resolution spectra the pass energy was generally set to 11 eV, giving an analyser resolution of less than or equal to 0.5 eV. Multipack version 9 software was utilized to analyse the spectra to identify the chemical compounds and their electronic states using Gaussian fits.

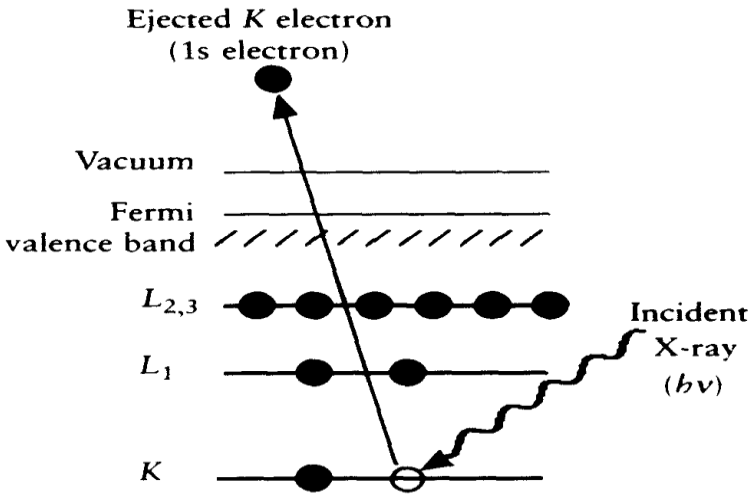

Figure 3.19: Schematic diagram of the XPS process, showing photoionization of an atom by the ejection of a 1s electron [26].

Figure 3.20: PHI 5000 Versaprobe XPS system at the Department of Physics, University of the Free State.

3.11. References

1. Jens Als-Nielsen, Des McMorrow. Elements of Modern X-ray Physics. 2nd Edition. John Wiley & Sons, London (2011). ISBN 978-0-470-97395-0

2. X-ray diffraction (XRD): [online]. Available from https://engineering.jhu.edu/labs/wp-content/uploads/sites/76/2016/04/Phillips-Basic-XRD-Theory.pdf (Accessed 16 August 2018)

3. Andrei A. Bunaciu, Elena gabriela Udriştioiu, Hassan Y. Aboul-Enein. X-Ray Diffraction: Instrumentation and Applications. *Critical Reviews in Analytical Chemistry* 45 (2015)289–99. https://doi.org/10.1080/10408347.2014.949616

4. B.D. Cullity. Elements of x-ray diffraction. Addison-Wesley Publishing Company, Reading (1956).

5. Ahmad Monshi, Mohammad Reza Foroughi, Mohammad Reza Monshi. Modified Scherrer Equation to Estimate More Accurately Nano-Crystallite Size Using XRD. *World Journal of Nano Science and Engineering* 2 (2012) 154–160. https://doi.org/10.4236/wjnse.2012.23020

6. X-ray diffraction: [online]. Available from https://chem.libretexts.org/Textbook_Maps/Analytical_Chemistry/Supplemental_Modules_(Analytical_Chemistry)/Instrumental_Analysis/Diffraction_Scattering_Techniques/Powder_X-ray_Diffraction (Accessed 17-08- 2018)

7. Vinod Kumar, H.C. Swart, S. Som, Vijay Kumar, A. Yousif, Anurag Pandey, S.K.K. Shaat, O.M. Ntwaeaborwa. The Role of Growth Atmosphere on the Structural and Optical Quality of Defect Free ZnO Films for Strong Ultraviolet Emission. *Laser Physics* 24 (2014) 105704. https://doi.org/10.1088/1054-660X/24/10/105704

8. V.D. Mote, Y. Purushotham, B.N. Dole. Williamson-Hall analysis in estimation of lattice strain in nanometer-sized ZnO particles. *Journal of Theoretical and Applied Physics* 6 (2012) 2-9. https://doi.org/10.1186/2251-7235-6-6

9. V. Meynen, P. Cool, E.F. Vansant. Verified Syntheses of Mesoporous Materials. *Microporous and Mesoporous Materials* 125 (2009) 170–223. https://doi.org/10.1016/j.micromeso.2009.03.046

10. Weilie Zhou, Zhong Lin Wang. Scanning Microscopy for Nanotechnology. Techniques and Applications. Springer Science+Business Media, New York (2006). ISBN-13: 978-0-387-33325-0

11. SEM technique: [online]. Available from https://www2.nau.edu/micro-analysis/wordpress/index.php/instrumentation/ (Accessed 12 November 2018).

12. Weilie Zhou, Zhong Lin Wang. Scanning Microscopy for NanotechnologyTechniques and Applications, Springer Science+Business Media, New York (2006). ISBN-13: 978-0-387-33325-0

13. I.M. Watt, The principles and practice of electron microscopy. 2nd Edition. Cambridge University Press, Cambridge (1997). ISBN: 0521435919

14. Nick Taylor. Energy Dispersive Spectroscopy, 2nd Edition, Essential Knowledge Briefings (2015) p. 9. ftp://iristor.vub.ac.be/patio/SURF/pub/DATATransit%20SURF-INTERNVUB/oscars/EDAX/EKB_Energy_Dispersive_Spectroscopy.pdf

15. UV-Vis spectrophotometer: [online]. Available from http://www.rsc.org/learn-chemistry/content/filerepository/CMP/00/001/304/UVVis_Student%20resource%20pack_ENGLISH.pdf (Accessed 12 November 2018).

16. UV-Vis spectroscopy: [online]. Available from https://orgspectroscopyint.blogspot.com/p/basics-of-uv-visible-spectroscopy.html (Accessed 13 November 2018).

17. H.A.A. Seed Ahmed, *Luminescence from lanthanide ions and the effect of co-doping in silica and other hosts*, PhD thesis, University of the Free State, Bloemfontein, South Africa, 2012.

18. Rosendo López, Ricardo Gómez. Band-Gap Energy Estimation from Diffuse Reflectance Measurements on Sol-Gel and Commercial TiO_2: A Comparative Study. *Journal of Sol-Gel Science and Technology* 61 (2012) 1–7. https://doi.org/10.1007/s10971-011-2582-9

19. Aman Pandey, Gunisha Jain, Divya Vyas, Silvia Irusta, Sudhanshu Sharma. Nonreducible, Basic La_2O_3 to Reducible, Acidic $La_{2-x}Sb_xO_3$ with Significant Oxygen Storage Capacity, Lower Band Gap, and Effect on the Catalytic Activity. *The Journal of Physical Chemistry C* 121 (2017) 481–489. https://doi.org/10.1021/acs.jpcc.6b10821

20. Brian C. Smith. Fundamentals of Fourier Transform Infrared Spectroscopy. Second Edition. CRC Press, Boca Raton (2011). ISBN: 13: 978-1-4200-6930-3

21. Walter M. Doyle. Principles and Applications of Fourier Transform Infrared (FTIR) Process Analysis. Technical Note AN–906 Rev. C. http://www.hellma-axiom.com/pdf/technical_notes/AN-906.pdf

22. Sally Eaton-Magana, Christopher M. Breeding. An Introduction to Photoluminescence Spectroscopy for Diamond and Its Applications in Gemology. *Gems & Gemology* (2016) 1–17. https://doi.org/10.5741/GEMS.52.1.2

23. J. García Solé, L.E. Bausá, D. Jaque. An introduction to the optical aspectroscopy of solids. John Wiley & Sons, Chichester (2005). ISBN 0-470-868864

24. Daniel C. Harris. Quantitative Chemical Analysis. 7th Edition. W. H. Freeman and Company, New York (2007) p. 394. ISBN: 0-7167-7041-5

25. GoCIE V2, K. R. Justin Thomas, Department of chemistry, Indian Institute of Technology Rookee, India, 2009. http://faculty.iitr.ac.in/~krjt8fcy/gocie.html

26. John F. Watts, John Wolstenholme. An introduction to surface analysis by XPS and AES. Wiley-VCH, New York (2003) p. 9. ISBN 0-470 84712 3

27. J.L. Ong, L.C. Lucas. Auger Electron Spectroscopy and Its Use for the Characterization of Titanium and Hydroxyapatite Surfaces. *Biomaterials* 19 (1998) 455–464. https://doi.org/10.1016/S0142-9612(97)00224-X

28. Cathodoluminescence: [online]. Available from http://www.microbeamanalysis.org/topical-conferences/cl 2011/Cathodoluminescence%202011Abstract%20Book.pdf (Accessed 20 November 2018).

29. K.V.R. Murthy, Hardev Singh Virk. Luminescence Phenomena: An Introduction. *Defect and Diffusion Forum* 347 (2013) 1–34. https://doi.org/10.4028/www.scientific.net/DDF.347.1.

30. Roushdey Salh. Defect Related Luminescence in Silicon Dioxide Network: A Review. Chapter 9 in: Sukamar Basu (Editor) *Crystalline Silicon - Properties and Uses* (2011) 135–

172. https://doi.org/10.5772/35404

31. Terrance E. Conners, Sujit Banerjee. Surface Analysis of paper. Boca Raton, New York (1995) 232. ISBN: 0-8493-8992-5

32. Krishna M. Pamidimukkala. X-Ray Photoelectron Spectroscopy, Paper Surface Analysis By. *Encyclopedia of Analytical Chemistry* (2006) 1–17. https://doi.org/10.1002/9780470027318.a2207

33. XPS process: [online]. Available from http://faculty.chem.queensu.ca/people/faculty/horton/research.html (Accessed 19 November 2018).

Chapter 4

Luminescence properties of Bi doped La_2O_3 powder phosphor

4.1. Introduction

Generally, a good host for luminescent ions must exhibit properties such as transparency for visible and infrared light as well as good chemical and structural stability. The rare earth oxides have attracted much research interest because of their prospective use as catalytic materials and for their excellent thermal, chemical, electrical, magnetic, ceramic and optical properties [1, 2]. Among all rare earth metal oxides, lanthanum oxide (La_2O_3) is recognized as having a relatively lower cost compared to other rare earth oxides (e.g. Lu_2O_3, Gd_2O_3) and as being an excellent host lattice for luminescent ions [3]. La_2O_3 belongs to the hexagonal crystal family (trigonal crystal system) with space group $P\bar{3}m1$ (No. 164) [4] and its structure is shown in figure 4.1. Each La^{3+} ion has equivalent surroundings, with C_{3v} site symmetry and coordination number seven (three O^{2-} ions being slightly further than the other four) [5].

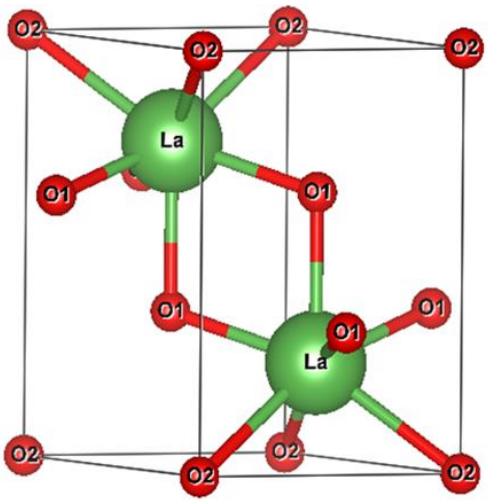

Figure 4.1: The unit cell of La_2O_3 drawn with the Vesta software [6].

La_2O_3 has various optical applications such as in infrared transmitting glass ceramics [7] and as an additive to various transparent ceramic laser materials to improve their optical properties [8]. It has also been assessed as a phosphor host doped with Eu [9], Bi [10], Er [11] and Yb [12] ions. Rare-earth ions are usually used as activators for luminescent materials due

to their intra-configurational 4f transitions [13]. However, main group metal ions such as Tl^{+}, Pb^{2+}, Bi^{3+} and Sb^{3+} may also be useful luminescence centres [14]. The luminescence properties of Bi^{3+} ions have been studied in different host materials [15], particularly Y_2O_3 [16]. For blue-emitting La_2O_3:Bi phosphor thin films it has been reported that the excitation spectrum consisted of two bands, the main excitation band around 302 nm and a weak band around 250 nm, associated with the $6s^2$–6s6p transitions in Bi^{3+} [10]. However, a third excitation peak located at 225 nm was reported by Tadatsugu Minami *et al.* [17]. The ground state of the Bi^{3+} ion, having $6s^2$ configuration, is $^1S_0$ and the excited $6s^16p^1$ configuration has four energy levels, namely $^3P_0$, $^3P_1$, $^3P_2$ and $^1P_1$. The optical transitions from $^1S_0$ to $^3P_0$ and $^3P_2$ are completely spin forbidden, whereas the transition from $^1S_0$ to $^1P_1$ is spin allowed. Mixing of the $^1P_1$ and $^3P_1$ levels by spin orbit coupling makes the $^3P_1$ allowed [18]. In this work, blue emitting Bi doped La_2O_3 powders ($La_{2-x}O_3:Bi_x$) were synthesized by the sol-gel combustion method and assessed as potential phosphor materials. Excitation and emission at 308 nm and 462 nm were attributed to transitions between the $^1S_0$ ground state and $^3P_1$ excited state with a Stokes shift of 1.35 eV. The blue emission could also be excited at 250 nm and the nature of this excitation was considered so that an energy level scheme for $La_{2-x}O_3:Bi_x$ could be constructed. The luminescence intensity was optimized by varying the Bi doping concentration and the annealing temperature. The low value of the optimal doping concentration (x = 0.002) and a decrease in the average lifetime measured with an increase of doping concentration suggest that there is a strong interaction between the Bi^{3+} ions.

4.2. Experimental

Powder samples of $La_{2-x}O_3:Bi_x$ were prepared via the citric acid sol-gel combustion method [19]. For the undoped host sample 2.5980 g of lanthanum nitrate ($La(NO_3)_3{\cdot}6H_2O$, 99.999%, purchased from Sigma Aldrich) and 2.5216 g of citric acid monohydrate ($C_6H_8O_7{\cdot}H_2O$, 99.5%, analytical grade, purchased from Sigma Aldrich) were completely dissolved in 20 ml of deionized water. Since Bi is known to form the stable oxide Bi_2O_3 composed of Bi^{3+} ions and the ionic radii of Bi^{3+} and La^{3+} ions are similar (no value is tabulated by Shannon [20] for VII coordinated Bi^{3+}, but for VI coordination the ionic radius of Bi^{3+} is 0.103 nm and that for La^{3+} is 0.1032 nm [20]), so the Bi dopant was expected to be incorporated by substitution of La. Therefore an appropriate amount of $La(NO_3)_3{\cdot}6H_2O$ was replaced by an equal amount of bismuth nitrate ($Bi(NO_3)_3.5H_2O$, 99.999% purchased from Sigma Aldrich), which was first dissolved separately in 5 ml of distilled water mixed with 0.125 ml of 70% concentrated

nitric acid and then introduced drop-wise to the above solution. The molar ratio of metal ions to citric acid was 1:2, consistent with the reaction

$$[4\text{-}2x]La(NO_3)_3 + [2x]Bi(NO_3)_3 + 8C_6H_8O_7 \rightarrow 2La_{2\text{-}x}O_3{:}Bi_x + 6NO + 48CO + 32H_2O + 3N_2$$

where the waters of hydration have been neglected for simplicity. The reaction beaker was heated at 80 °C under vigorous stirring for 3 h, after which about 10 ml of gel remained. This was placed in a furnace set to 250 °C where it burnt with a white flame. The resulting product was a brown powder. The final $La_{2\text{-}x}O_3{:}Bi_x$ powders were obtained after annealing for 2 h, either in air or a reducing atmosphere (5% H_2 in Ar gas) at different temperatures between 800 °C and 1400 °C. Samples were stored in a vacuum desiccator to prevent absorption of moisture from the air and the formation of lanthanum hydroxide.

The phase composition was characterized by X-ray diffraction (XRD) measurements using a Bruker D8 Advance diffractometer. The Cu Kα X-ray source was operated at an accelerating voltage of 40 kV and a current of 40 mA and emitted characteristic X-rays with wavelength 0.154 nm. Diffuse reflectance spectra were recorded using a Lambda 950 UV-vis spectrophotometer from PerkinElmer with integrating sphere accessory. The photoluminescence (PL) properties of the powders were measured at room temperature using a Cary Eclipse fluorescence spectrophotometer equipped with a 150W monochromatized xenon flash lamp as an excitation source, operating in fluorescence mode. A JSM-7800F scanning electron microscope (SEM) was used to analyse the particle morphology. The chemical composition was determined by energy dispersive X-ray spectroscopy (EDS) using an X-Max^{N}80 detector from Oxford Instruments in the SEM. Surface elemental composition analysis was carried out using a PHI 700 Nano scanning Auger electron microprobe (Auger/NanoSAM) with a 20 kV, 1 nA electron beam. Decay curves were measured using an FLS980 fluorescence spectrometer from Edinburgh Instruments with an EPLED light source of fixed wavelength 304 nm, bandwidth 10 nm and pulse time less than 1 ns. The International Commission for Illumination (CIE) coordinates of the emitted light was calculated using the GoCIE software [21]

4.3. Results and discussion

4.3.1. Structural, morphology and chemical composition analysis

The XRD patterns of $La_{2-x}O_3:Bi_x$ powder samples having x = 0, 0.002 and 0.01, annealed in air at 1200 °C, are shown in figure 4.2(a), together with data from JCPDS card #05-0602 for La_2O_3. The good match of all the observed peaks revealed that La_2O_3 with its hexagonal crystal structure had been successfully synthesized. No extra diffraction peaks due to impurities were detected, suggesting that the Bi^{3+} ions were successfully incorporated in the La_2O_3 host structure. Also, no obvious shifting of the peak positions was observed while the Bi concentration increased. The average crystallite size *D* was estimated from the full-width at half-maximum β of the diffraction peaks using the Scherrer equation [22], $D = \frac{0.9\lambda}{\beta cos\theta}$, where λ is the X-ray wavelength and θ is the Bragg angle. The results are summarized in Table 4.1 and show that the average crystallite size for the La_2O_3 pure host and doped $La_2O_3:Bi_x$ powders (x = 0, 0.002 and 0.01) were almost the same (~87 nm).

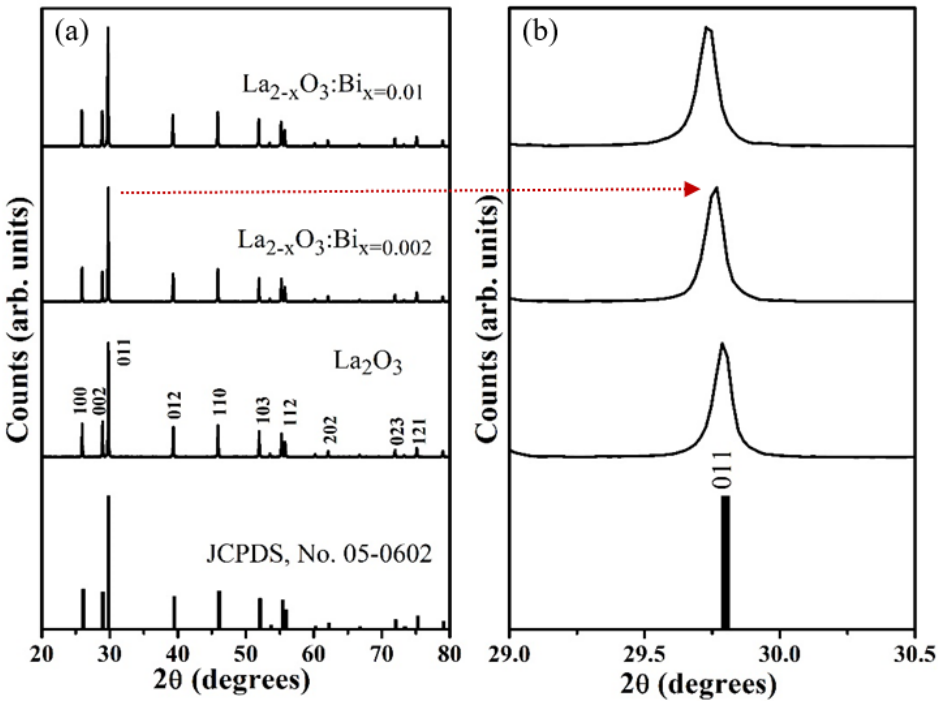

Figure 4.2: (a) XRD patterns of La_2O_3 and $La_{2-x}O_3:Bi_x$ powders (x = 0.002 and 0.01) together with JCPDS card #05-0602 for La_2O_3. (b) Magnified view of the 011 main diffraction peak.

Table 4.1: Crystallite sizes calculated from the Scherrer equation.

Diffraction peak	Crystallite size (nm)		
	La_2O_3	**$La_{2-x}O_3:Bi_{x=0.002}$**	**$La_{2-x}O_3:Bi_{x=0.01}$**
100	96	92	94
002	89	85	87
011	96	93	90
012	88	88	86
110	84	88	88
103	78	81	83
112	77	84	85
201	82	88	87
Average	86 ± 7	87 ± 4	88 ± 3

Figure 4.3 shows SEM images of the La_2O_3 host powders that were annealed at (a) 800 °C and (b) 1200 °C in air. The grain size increased with increasing annealing temperature. The shape changed from rectangular to more round, but faceted. Figure 4.3(c) is the SEM image of the doped $La_{2-x}O_3:Bi_{x=0.01}$ annealed at 1200 °C. The grain size and shape are similar to the undoped sample annealed at the same temperature, but the doped sample had some steps on the grains. Figure 4.3(d) shows similar steps observed with poorer resolution for a SEM image taken using the NanoSAM system, which allowed Auger spectra such as that in figure 4.3(e) to be collected from various positions on the surface. Only La, O and adventitious C Auger peaks were observed at various positions near the step, showing that Bi was not enriched as part of the surface near the step structure, although it may be present at a concentration below the detection limit. Although the origin of the steps on the surface of the grains of the doped material is unclear, they may be associated with the much lower melting point of Bi_2O_3 (817 °C) [23] compared to La_2O_3 (2350 °C) [24].

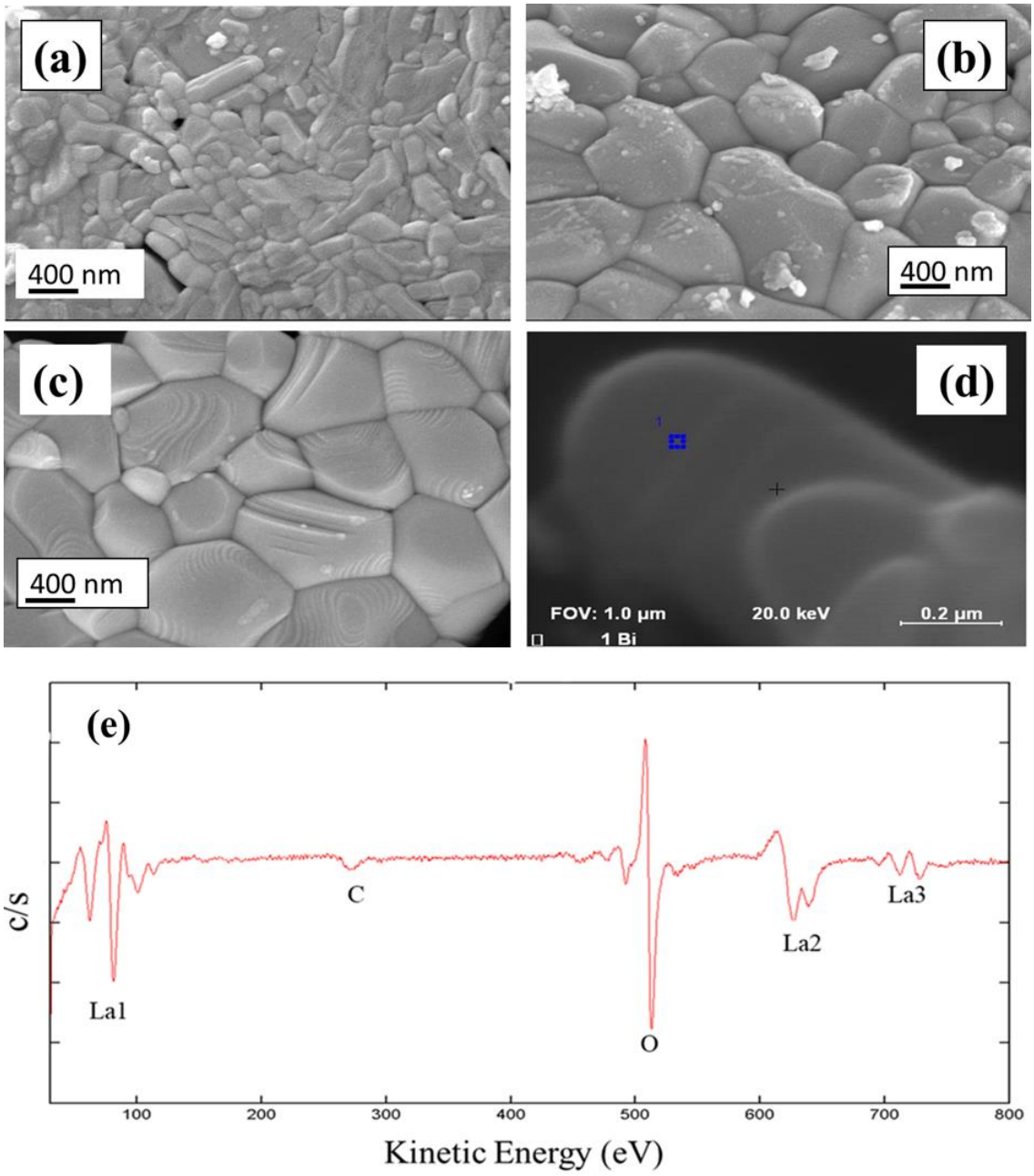

Figure 4.3: SEM images of the La_2O_3 host powder annealed at (a) 800 °C and (b) 1200 °C in air. SEM images of $La_{2-x}O_3:Bi_{x=0.01}$ annealed at 1200 °C in air taken with (c) the JEOL SEM (d) NanoSAM. (e) Auger spectrum of $La_{2-x}O_3:Bi_{x=0.01}$ annealed in air at 1200 °C, representative of all points near the step edge.

The EDS spectrum shown in figure 4.4(a) of the undoped sample confirmed the presence of La and O, together with a very small quantity of C that probably originated from the citric acid precursor used in the sol-gel combustion synthesis, or possibly could result from the carbon tape that was used to mount the samples. The EDS spectrum of the doped sample in

figure 4(b) is similar except for the additional small peak near 2.5 keV attributed to the Bi dopant.

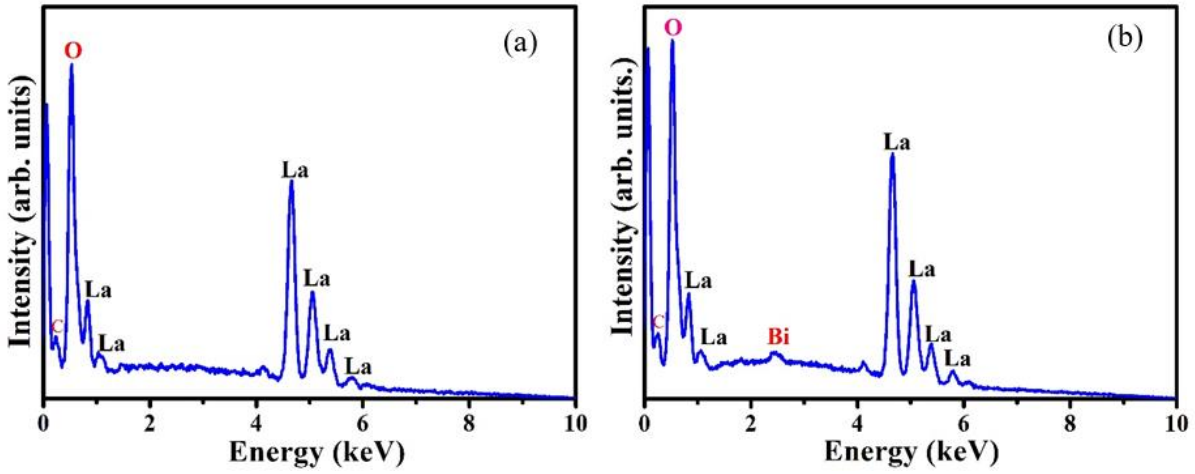

Figure 4.4: EDS spectra of (a) La_2O_3 and (b) $La_{2-x}O_3:Bi_{x=0.01}$ phosphor powders annealed at 1200 °C in air.

4.3.2. Diffuse reflectance spectra and band gap calculation

Diffuse reflectance spectroscopy was used to study the absorption properties of the La_2O_3 pure host and the effects of Bi when incorporated in the host lattice, as shown in figure 4.5(a). For the host as well as doped samples the diffuse reflection (R_∞) decreased dramatically below 250 nm, which was attributed to absorption above the band gap. An absorption band centered at 308 nm was only present in the doped samples and it increased with increasing Bi concentration. Therefore it was attributed to absorption by the Bi^{3+} ions. The Kubelka-Munk function $F(R_\infty) = \frac{(1-R_\infty)^2}{2R_\infty}$ can be used to convert the diffuse reflectance measurements to values proportional to the absorption [25]. For an indirect band gap material such as La_2O_3 a Tauc plot of $[F(R_\infty)h\nu]^{1/2}$ versus $h\nu$ can then be used to determine the optical band gap by fitting a linear region and extrapolating this to where it cuts the horizontal (energy) axis [26]. Such a plot is shown in figure 4.5(b) for the La_2O_3 host, from which the band gap was estimated to be 5.1 eV. In addition, the band gap of La_2O_3 has been reported by several groups as summarized in Table 4.2. Although the values vary quite considerably, the result obtained here correlates well with more recent measurements reported since 2014.

Table 4.2: Band gaps of La_2O_3 reported from various experiments.

Band gap (eV)	Technique	Year	Reference
3.6	UV-vis transmission	2008	28
5.84	UV-vis transmission	2009	27
5.3	Spectroscopic ellipsometry	2009	29
5.18 ± 0.2 5.20	XPS UV-vis transmission	2014	30
5.20 - 5.55	XPS	2017	1
5.0	UV-vis reflectance	2017	26

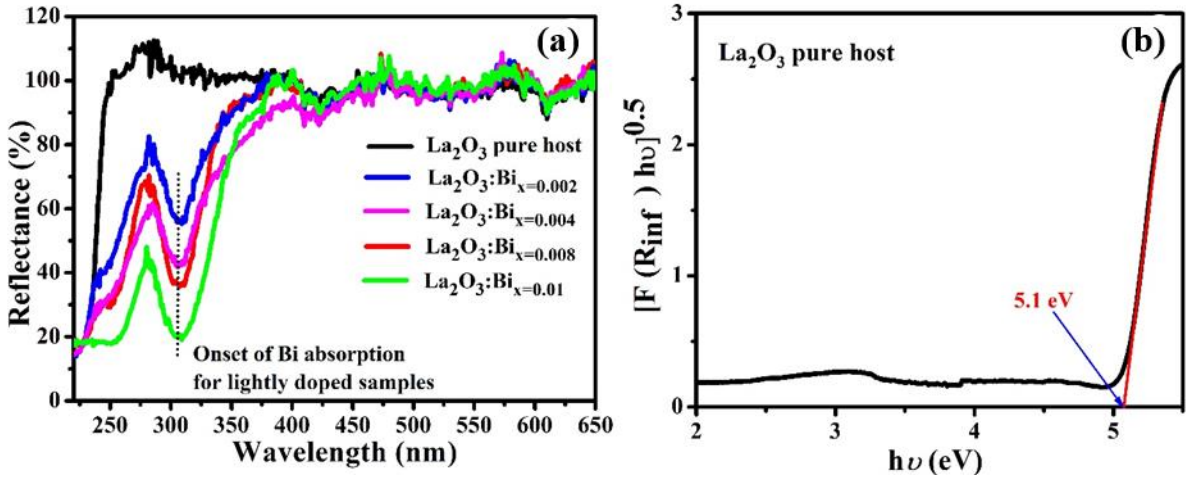

Figure 4.5: (a) Diffuse reflectance spectra of La_2O_3 pure host and doped samples annealed at 1200 °C in air. (b) A Tauc plot to obtain the indirect optical band gap of undoped La_2O_3.

4.3.3. Photoluminescence (PL) analysis

Figure 4.6(a) shows the PL excitation and emission spectra of the La_2O_3 doped with different Bi concentrations annealed at 1200 °C in air. Blue emission was observed at 462 nm, for which the excitation spectra consisted of two peaks at 250 nm and 308 nm. We did not observe the excitation peak at 225 nm as reported in [17]. As mentioned in the introduction, the Bi^{3+} ion has four excited states ($^3P_0$, $^3P_1$, $^3P_2$ and $^1P_1$, in increasing energy as shown in figure 4.7) of which transitions to the $^3P_0$ and $^3P_2$ levels are not allowed. In early work, Boulon [31] measured similar luminescence spectra and assigned the two excitation peaks to transitions from the $^1S_0$ ground state to the $^1P_1$ and $^3P_1$ energy levels. The lower energy excitation peak observed in this work (308 nm, 4.03 eV) is similarly assigned to the $^1S_0 \rightarrow {}^3P_1$ transition, but the higher energy excitation peak (250 nm, 4.96 eV) requires more careful

consideration. Lili Want *et al.* [32] considered a large number of Bi^{3+} doped materials and obtained a quantitative relationship between the energies of the co-called A band ($^1S_0 \rightarrow {}^3P_1$) and C band ($^1S_0 \rightarrow {}^1P_1$), namely $E_C = 3.236 + 2.290(E_A - 2.972)^{0.856}$ for values in eV. This predicts that if the $^1S_0 \rightarrow {}^3P_1$ excitation occurs at 308 nm in La_2O_3, then the $^1S_0 \rightarrow {}^1P_1$ excitation may be expected near 5.64 eV (220 nm). However, the observed higher energy excitation band in figure 4.6(a) occurs at a longer wavelength (250 nm) and a comparison between the reflectance of the pure host and doped samples in figure 4.5(a) also shows evidence of absorption near 250 nm. Many materials doped with Bi^{3+} have been reported to exhibit a metal to metal charge transfer (MMCT) from the Bi^{3+} ion to cations of the host, which can be considered as a transition from the Bi^{3+} ground state ($^1S_0$) to the host conduction band (see figure 4.7). Boutinaud [33] evaluated many hosts doped with Bi^{3+} ions and showed that the energy of the MMCT absorption, in hosts where the cation coordination exceeded 4, was predicted to an accuracy of ±3 000 cm^{-1} by the equation E_{MMCT} = 55 000 - 45 500χ/d (in cm^{-1}), where χ is the electronegativity of the host cations and d is the distance between the Bi^{3+} and host cations (in Å). Using his values $\chi = 1.3$ and $d = 3.98$ Å predicts that for $La_{2-x}O_3:Bi_x$ the MMCT excitation may be expected at 40 000 ± 3 000 cm^{-1} i.e. 250 ± 20 nm. This matches perfectly with the higher energy excitation band measured in this study, which is therefore assigned to the MMCT band rather than to the C band.

The single broad band of blue emission, shown in figure 4.6(a), which was centered at 462 nm (2.68 eV) was attributed to radiative transitions from the $^3P_1$ excited state back to the $^1S_0$ ground state, with a Stokes shift of 1.35 eV. For comparison, Y_2O_3:Bi has two emission bands located at 407 and 495 nm which are attributed to Bi^{3+} ions in two different sites of the host lattice [34]. The single emission in our results indicates that only one site occurs for Bi^{3+} ions in the La_2O_3 host, which is consistent with Bi substituting for La in the crystal structure where all the La sites are equivalent. Figure 4.6(b) shows the emission intensity as a function of Bi doping concentration, with the maximum occurring for x = 0.002. Above that concentration the luminescence intensity decreases, which can be ascribed to concentration quenching. When concentration quenching occurs due to migration of energy between the activators as a result of electric dipole or quadrupole interactions, appreciable quenching may occur for low dopant concentrations from 0.001 to 0.01 [35], suggesting a strong interaction between the Bi^{3+} ions. The PL emission intensity as a function of annealing temperature, for annealing in air between 800 °C to 1400 °C, is shown in figure 4.6(d). The blue PL intensity increased as the annealing temperature was increased, reaching a maximum at an annealing

temperature 1200 °C and then decreased with a further increase of the temperature. The luminescence intensity may be expected to increase with annealing temperature due to improvement of the crystalline quality and elimination of defects. Alternatively, in a study of the effect of annealing temperature on Bi doped Y_2O_3 powders [34] the increase of the luminescence intensity with annealing temperature up to a maximum value was attributed to segregation effects of the dopant to the particle surface, while quenching at higher temperatures was caused by evaporation loss of the dopant from the sample surface. The optimum annealing temperature for $La_{2-x}O_3:Bi_x$ (1200 °C) found in this study was lower than that reported for $Y_{2-x}O_3:Bi_x$ (1400 °C) [34].

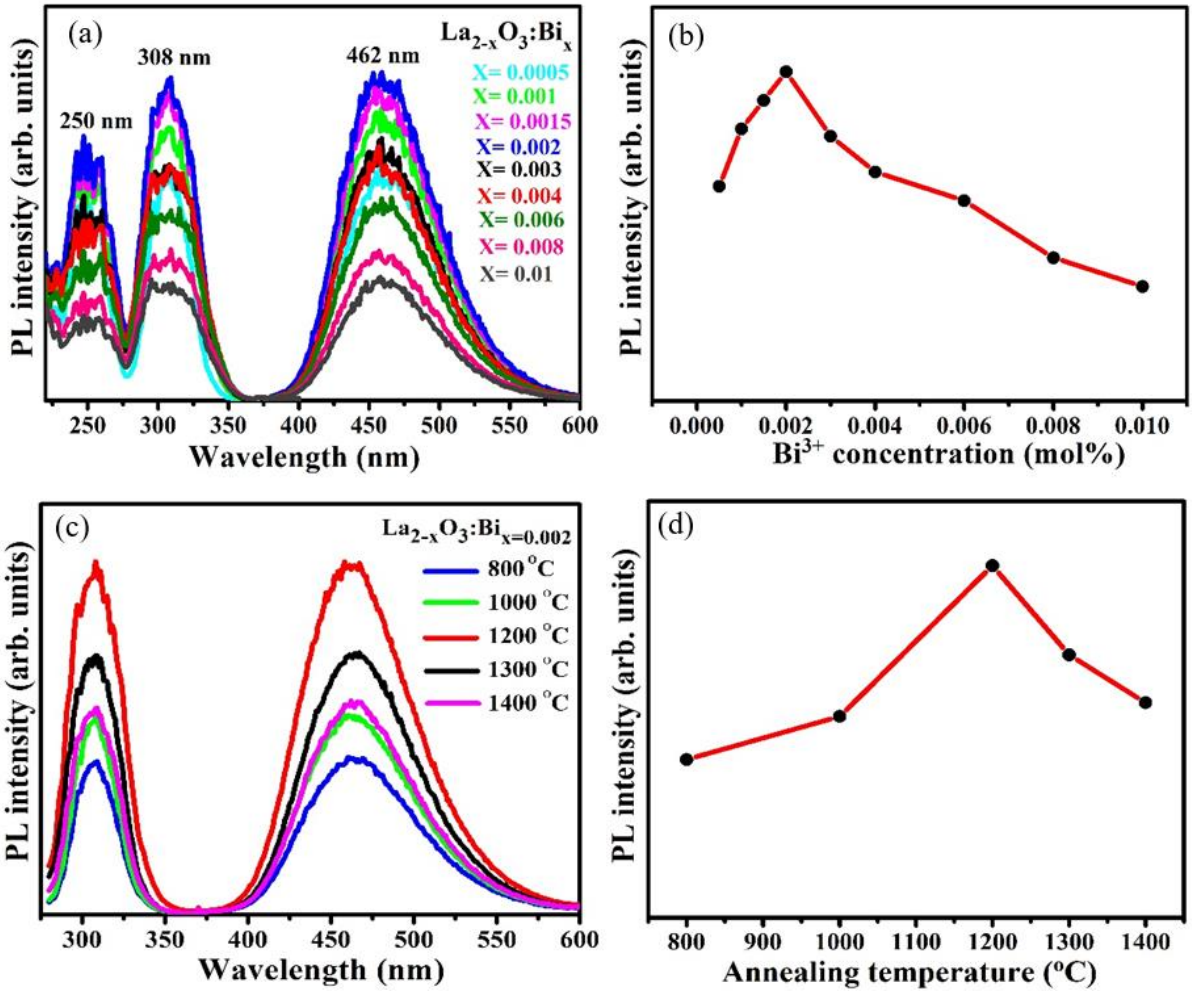

Figure 4.6: (a) Excitation and emission spectra of $La_{2-x}O_3:Bi_x$ doped with different Bi concentrations, annealed in air at 1200 °C. (b) Emission peak intensity as a function of Bi concentration. (c) Excitation and emission spectra of $La_{2-x}O_3:Bi_{x=0.002}$ annealed at different temperatures. (d) Emission peak intensity as a function of the annealing temperature.

Figure 4.7 shows a schematic diagram of the energy levels involved in the optical properties of $La_{2-x}O_3:Bi_x$ which was constructed using data measured in this work. The band gap, from the diffuse reflection results, was taken as 5.1 eV. The bottom of the $^1S_0$ level, used as the reference (zero) level, was located at 4.96 eV below the conduction band based on the measured energy of the MMCT excitation, which meant that it was located quite close to the valence band. The curve representing the $^3P_1$ energy level was located in the band gap with its minimum being offset so that the excitation and emission between the $^1S_0$ and $^3P_1$ matched the experimental data (4.03 eV and 2.68 eV respectively). The position of the $^1P_1$ band, not observed in this study, was located at its predicted position of 5.64 eV. While the position of the $^3P_2$ level was not known and it was placed randomly between the $^3P_1$ and $^1P_1$ levels, the $^3P_0$ level has been reported to act as a non-radiative electron trap 371 cm^{-1} (0.046 eV) below the $^3P_1$ level [33] and was placed appropriately.

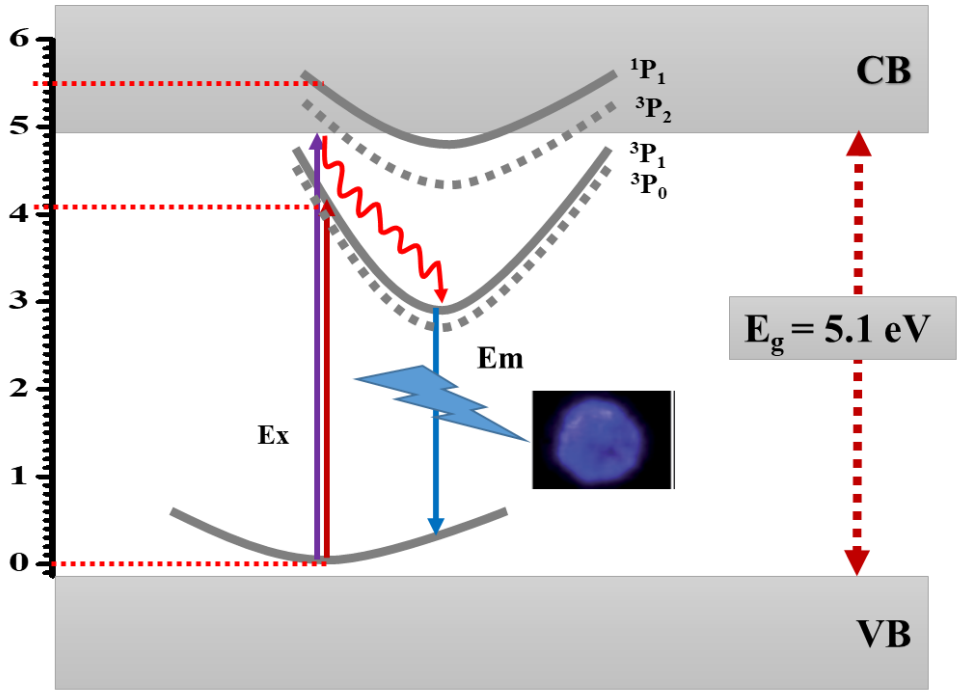

Figure 4.7: Energy level diagram for Bi doped La_2O_3.

The decay curves of $La_{2-x}O_3:Bi_x$ powder phosphors are shown in Figure 4.8. Although the sample with lowest doping (x = 0.001) showed a single exponential decay, the samples having higher Bi concentration deviated from simple exponential decay curves. For consistency, all the curves were fitted by a double exponential decay model

$$I(t) = A_0 + A_1\exp(-t/\tau_1) + A_2\exp(-t/\tau_2) \quad \ldots\ldots\ldots\ldots\ldots\ldots \quad (4.1)$$

where τ_1 and τ_2 are the short- and long-decay components, A_0 is the background and A_1 and A_2 are the fitting constants. The average lifetimes (τ_{ave}) were obtained using $\tau_{ave} = (A_1\tau_1^2 + A_2\tau_2^2)/(A_1\tau_1 + A_2\tau_1)$ and are given with the fitting data in Table 4.3. The average lifetime decreased with increasing the Bi^{3+} doping concentration, which can be ascribed to energy migration between the Bi^{3+} ions which also led to the concentration quenching at increased doping levels discussed earlier.

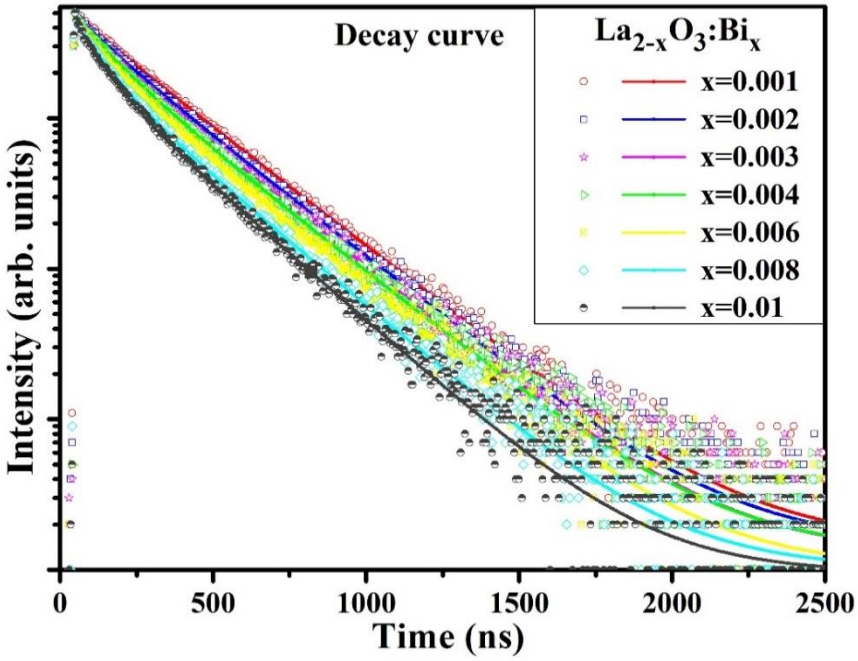

Figure 4.8: Fluorescence decay curves of $La_{2-x}O_3:Bi_x$ phosphor powders annealed at 1200 °C (excitation 304 nm, emission 462 nm).

Table 4.3: Fitting parameters for the decay curves and average lifetimes of $La_{2-x}O_3:Bi_x$ powder phosphors.

Bi concentration (x)	A_1 (%)	τ_1 (ns)	A_2 (%)	τ_2 (ns)	τ_{ave} (ns)
0.001	11	115	89	276	268
0.002	20	118	80	273	258
0.003	24	105	76	269	251
0.004	34	119	66	272	244
0.006	36	91	64	260	232
0.008	46	89	54	252	215
0.01	48	79	52	241	203

Figure 4.9(a) presents the chromaticity coordinates of $La_{2-x}O_3:Bi_{x=0.002}$ powder phosphor under excitation of 308 nm, determined using the GoCIE software. Its blue colour has chromaticity coordinates X = 0.15 and Y = 0.17. Figure 4.9(b) compares the PL excitation and emission of $La_{2-x}O_3:Bi_{x=0.002}$ powder phosphor annealed at 1200 °C in air with that annealed in a reducing atmosphere (5% H_2 and 95% Ar gas mixture). Annealing $Ba_2P_2O_7$ in a reducing (CO) atmosphere at 1100 °C was reported to change the valence state of Bi^{3+} ions to Bi^{2+} and Bi^0 [36]. Lower valence (Bi^{2+}) ions, although they are difficult to stabilize, have been reported to give orange-red emission [37], but no additional luminescence bands or shift in emission wavelength were observed for the reduced sample. The blue (Bi^{3+}) luminescence from the reduced sample was less intense compared to the sample annealed in air, which may be due to reduction of some Bi^{3+} ions to non-luminescent Bi atoms [38] or to enhanced evaporation loss of Bi from the surface when annealed in the reducing atmosphere.

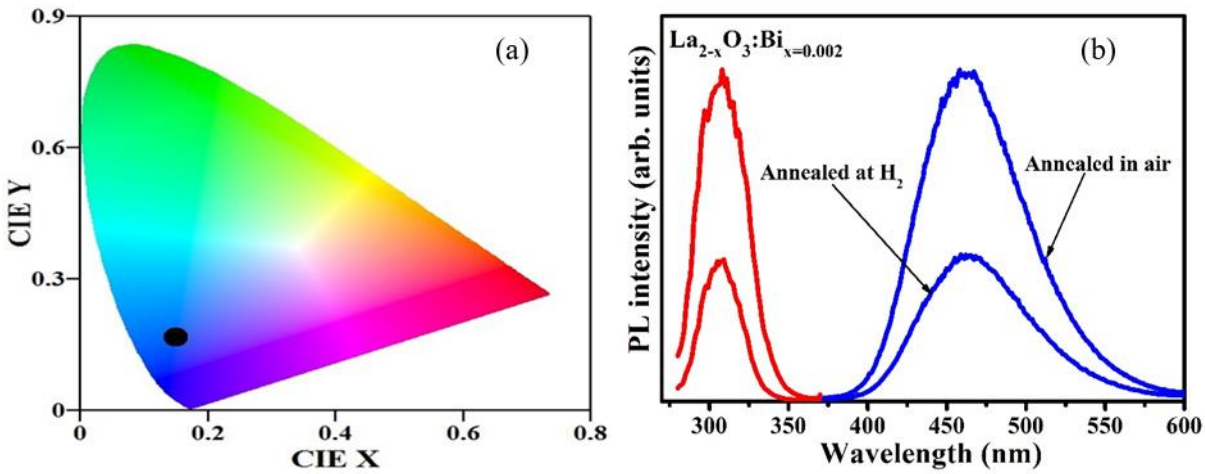

Figure 4.9: (a) CIE coordinate diagram for $La_{2-x}O_3:Bi_{x=0.002}$ powder phosphor. (b) Comparison of the excitation and emission spectra of $La_2O_3:Bi_{x=0.002}$ annealed at 1200 °C in air and in reducing atmosphere (5% H_2 and 95% Ar gas mixture).

4.4. Conclusion

$La_{2-x}O_3:Bi_x$ has been successfully synthesized via the sol-gel combustion method. The XRD patterns confirmed the formation of the pure La_2O_3 hexagonal phase. SEM images showed that the grain size increased with increasing annealing temperature. The diffuse reflectance spectra for the doped sample showed two absorption bands, one located at 308 nm and another at shorter wavelengths (250 nm and less). The band located at 308 nm was only present in the doped samples and was therefore attributed to absorption by Bi^{3+} ions. The shorter wavelength absorption was due to the MMCT absorption of the Bi^{3+} ions and the

indirect band gap absorption. From reflectance data of the pure host sample the band gap of La_2O_3 was found to be 5.1 eV. A broad band of blue fluorescence emission centered at 462 nm was observed when excited at 308 nm, which was attributed to the $^3P_1 \rightarrow {}^1S_0$ transition of Bi^{3+} ions. The emission intensity was measured as a function of Bi doping concentration, with the maximum occurring for x = 0.002. The concentration quenching at this relatively low doping concentration was attributed to strong interaction of the Bi^{3+} ions allowing energy migration between them, which also was responsible for the decrease in the average lifetime observed with increasing doping concentration. The reported properties show that $La_{2-x}O_3:Bi_x$ can be used as a blue emitting phosphor and clarify the energy level diagram for this material.

4.5. References

1. Xing Wang, Hongxia Liu, Lu Zhao, Chenxi Fei, Xingyao Feng, Shupeng Chen, Yongte Wang. Structural Properties Characterized by the Film Thickness and Annealing Temperature for La_2O_3 Films Grown by Atomic Layer Deposition. *Nanoscale Research Letters* 12 (2017) 233 (7 pages). https://doi.org/10.1186/s11671-017-2018-8
2. M. Méndez, J.J. Carvajal, L.F. Marsal, P. Salagre, M. Aguiló, F. Díaz, P. Formentín, J. Pallarès, Y. Cesteros. Effect of the $La(OH)_3$ Preparation Method on the Surface and Rehydroxylation Properties of Resulting La_2O_3 Nanoparticles. *Journal of Nanoparticle Research* 15 (2013) 1479 (16 pages). https://doi.org/10.1007/s11051-013-1479-7
3. Lixin Song, Pingfan Du, Jie Xiong, Xiaona Fan, Yuxue Jiao. Preparation and Luminescence Properties of Terbium-Doped Lanthanum Oxide Nanofibers by Electrospinning. *Journal of Luminescence* 132 (2012) 171–174. https://doi.org/10.1016/j.jlumin.2011.08.007
4. M. Méndez, J.J. Carvajal, Y. Cesteros, M. Aguiló, F. Díaz, A. Giguère, D. Drouin, E. Martínez-Ferrero, P. Salagre, P. Formentín, *et al.* Sol-Gel Pechini Synthesis and Optical Spectroscopy of Nanocrystalline La_2O_3 doped with Eu^{3+}. *Optical Materials* 32 (2010) 1686–1692. https://doi.org/10.1016/j.optmat.2010.02.018
5. G. Chen, J.R. Peterson. Systematics of the Phase Behavior in Lanthanide Sesquioxides. *Journal of Alloys and Compounds* 186 (1992) 233–239. https://doi.org/10.1016/0925-8388(92)90009-X
6. Koichi Momma, Fujio Izumi. VESTA 3 for Three-Dimensional Visualization of Crystal, Volumetric and Morphology Data. *Journal of Applied Crystallograph* 44 (2011)1272–1276. https://doi.org/10.1107/S0021889811038970

7. L. Armelao, M. Pascolini, G. Bottaro, G. Bruno, M.M. Giangregorio, M Losurdo, G Malandrino, R. Lo Nigro, M.E. Fragalà, E. Tondello. Microstructural and Optical Properties Modifications Induced by Plasma and Annealing Treatments of Lanthanum Oxide Sol-Gel Thin Films. *The Journal of Physical Chemistry C* 113 (2009) 2911–2918. https://doi.org/10.1021/jp809824e

8. Jun Ding, Qiuhong Yang, Zaifeng Tang, Jun Xu, Liangbi Su. Investigation of the spectroscopic properties of $(Y_{0.92-x}La_{0.08}Nd_x)_2O_3$ transparent ceramics. *Journal of the Optical Society of America B* 24 (2007) 681–684. https://doi.org/10.1364/JOSAB.24.000681

9. B. Pu, Z. Mo, C. Jiang, R. Guo. Synthesis and Luminescence Properties of Rod-Shaped $La_2O_3:Eu^{3+}$ Nanocrystalline Using Carbon Nanotubes as Templates. *Synthesis and Reactivity in Inorganic, Metal-Organic and Nano-Metal Chemistry* 45 (2015) 988–992. https://doi.org/10.1080/15533174.2013.843547

10. Toshihiro Miyata, Jun Ichi Ishino, Keiichi Sahara, Tadatsugu Minami. Color Control of Emissions from Rare Earth Co-Doped La_2O_3:Bi Phosphor Thin Films Prepared by Magnetron Sputtering. *Thin Solid Films* 519 (2011) 8095–8099. https://doi.org/10.1016/j.tsf.2011.04.236

11. A.K Singh, S. Singh, D. Kumar, D.K. Rai, S.B. Rai, K. Kumar. Light-into-heat conversion in $La_2O_3:Er^{3+}$-Yb^{3+} phosphor: an incandescent emission. *Optics Letters* 37 (2012) 776–778. https://doi.org/10.1364/OL.37.000776

12. Xiao Zhang, Piaoping Yang, Dong Wang, Jie Xu, Chunxia Li, Shili Gai, Jun Lin. $La(OH)_3:Ln^{3+}$ and $La_2O_3:Ln^{3+}$ (Ln = Yb/Er, Yb/Tm, Yb/Ho) Microrods: Synthesis and Up-Conversion Luminescence Properties. *Crystal Growth & Design* 12 (2012) 306–312. https://doi.org/10.1021/cg201091u

13. Qiangbing Guo, Beibei Xu, Dezhi Tan, Juechen Wang, Shuhong Zheng, Wei Jiang, Jianrong Qiu, Shifeng Zhou. Regulation of Structure Rigidity for Improvement of the Thermal Stability of Near-Infrared Luminescence in Bi-Doped Borate Glasses. *Optics Express* 21 (2013) 27835–27840. https://doi.org/10.1364/OE.21.027835

14. G. Blasse, A. Bril. Investigations on Bi^{3+} Activated Phosphors. *The Journal of Chemical Physics* 48 (1968) 217–222. https://doi.org/10.1063/1.1667905

15. Roy H.P. Awater, Pieter Dorenbos. The Bi^{3+} 6s and 6p Electron Binding Energies in Relation to the Chemical Environment of Inorganic Compounds. *Journal of Luminescence* 184 (2017) 221–231. https://doi.org/10.1016/j.jlumin.2016.12.021

16. R.M. Jafer, E. Coetsee, A. Yousif, R.E. Kroon, O.M. Ntwaeaborwa, H.C. Swart. X-Ray Photoelectron Spectroscopy and Luminescent Properties of $Y_2O_3:Bi^{3+}$ phosphor. *Applied*

Surface Science 332 (2015) 198–204. https://doi.org/10.1016/j.apsusc.2015.01.009

17. Tadatsugu Minami, Toshihiro Miyata, Kouhei Ueda, Shun Matsui, Haruki Fukada. PL and EL Characteristics in New Blue Emitting La_2O_3:Bi Phosphor Thin Films. *ECS Transactions* 16 (2009) 39–45. https://doi.org/10.1149/1.3106670

18. W.A.I. Tabaza, H.C. Swart, R.E. Kroon. Optical properties of Bi and energy transfer from Bi to Tb in $MgAl_2O_4$ phosphor. *Journal of Luminescence* 148 (2014) 192–197. https://doi.org/10.1016/j.jlumin.2013.12.018

19. A. Yousif, R. M. Jafer, S. Som, M.M. Duvenhage, E. Coetsee, H.C. Swart. Ultra-broadband luminescent from a Bi doped CaO matrix. *RSC Advances* 5 (2015) 54115–54122. https://doi.org/10.1039/C5RA09246A

20. R.D. Shannon. Revised Effective Ionic Radii and Systematic Studies of Interatomie Distances in Halides and Chaleogenides. *Acta Crystallographica Section A* 32 (1976) 751–767. https://doi.org/10.1107/S0567739476001551

21. GoCIE V2, K. R. Justin Thomas, Department of chemistry, Indian Institute of Technology Rookee, India, 2009. http://faculty.iitr.ac.in/~krjt8fcy/gocie.html

22. R.E. (Ted) Kroon. Nanoscience and the Scherrer equation versus the 'Scherrer–Gottingen equation'. *South African Journal of Science* 109(5/6) (2013) Art. #a0019 (2 pages). https://dx.doi.org/10.1590/sajs.2013/a0019

23. Yayuk Astuti, Arnelli Arnelli, Pardoyo Pardoyo, Amilia Fauziyah, Siti Nurhayati, Arum Dista Wulansari, Rizka Andianingrum, Hendri Widiyandari, Gaurav A. Bhaduri. Studying Impact of Different Precipitating Agents on Crystal Structure, Morphology and Photocatalytic Activity of Bismuth Oxide. *Bulletin of Chemical Reaction Engineering & Catalysis* 12 (2017) 478–484. https://doi.org/10.9767/bcrec.12.3.1144.478-484

24. Riya Dey, Anurag Pandey, Vineet Kumar Rai. The Er^{3+}-Yb^{3+} codoped La_2O_3 phosphor in Finger Print Detection and Optical Heating. *Spectrochimica Acta Part A* 128 (2014) 508–513. https://doi.org/10.1016/j.saa.2014.02.175

25. Rosendo López, Ricardo Gómez. Band-Gap Energy Estimation from Diffuse Reflectance Measurements on Sol-Gel and Commercial TiO_2: A Comparative Study. *Journal of Sol-Gel Science and Technology* 61 (2012) 1–7. https://doi.org/10.1007/s10971-011-2582-9

26. Aman Pandey, Gunisha Jain, Divya Vyas, Silvia Irusta, Sudhanshu Sharma. Nonreducible, Basic La_2O_3 to Reducible, Acidic $La_{2-x}Sb_xO_3$ with Significant Oxygen Storage Capacity, Lower Band Gap, and Effect on the Catalytic Activity. *The Journal of Physical Chemistry C* 121 (2017) 481–489. https://doi.org/10.1021/acs.jpcc.6b10821

27. Chen Yang, Huiqing Fan, Shaojun Qiu, Yingxue Xi, Yunfei Fu. Microstructure and Dielectric Properties of La_2O_3 films Prepared by Ion Beam Assistant Electron-Beam Evaporation. *Journal of Non-Crystalline Solids* 355 (2009) 33–37. https://doi.org/10.1016/j.jnoncrysol.2008.09.029

28. F.J. Jing, N. Huang, Y.W. Liu, W. Zhang, X.B. Zhao, R.K.Y. Fu, J.B. Wang, Z.Y. Shao, J.Y. Chen, Y.X. Leng, *et al.* Hemocompatibility and Antibacterial Properties of Lanthanum Oxide Films Synthesized by Dual Plasma Deposition. *Journal of Biomedical Materials Research - Part A* 87 (2008) 1027–1033. https://doi.org/10.1002/jbm.a.31838

29. Yi Zhao, Koji Kita, Kentaro Kyuno, Akira Toriumi. Band Gap Enhancement and Electrical Properties of La_2O_3 Films Doped with Y_2O_3 as High-k Gate Insulators. *Applied Physics Letters* 94 (2009) 042901 (3 pages). https://doi.org/10.1063/1.3075954

30. Liu Qi-Ya, Ze-Bo Fang, Ting Ji, Shi-Yan Liu, Yong-Sheng Tan, Jia-Jun Chen, Yan-Yan Zhu. Band Alignment and Band Gap Characterization of La_2O_3 Films on Si Substrates Grown by Radio Frequency Magnetron Sputtering. *Chinese Physics Letters* 31 (2014) 027702 (4 pages). https://doi.org/10.1088/0256-307X/31/2/027702

31. G. Boulon. Processus de Photoluminescence Dans Les Oxydes et Les Orthovanadates de Terres Rares Polycristallins Activés Par l'ion Bi^{3+}. *Journal de Physique* 32 (1971) 333–347. https://doi.org/10.1051/jphys:01971003204033300

32. Lili Wang, Qiang Sun, Qingzhi Liu, Jinsheng Shi. Investigation and Application of Quantitative Relationship between sp Energy Levels of Bi^{3+}ion and Host Lattice. *Journal of Solid State Chemistry* 191 (2012) 142–46. https://doi.org/10.1016/j.jssc.2012.03.015

33. Philippe Boutinaud. Revisiting the Spectroscopy of the Bi^{3+} Ion in Oxide Compounds. *Inorganic Chemistry* 52 (2013) 6028–6038. https://doi.org/10.1021/ic400382k

34. R.M. Jafer, H.C. Swart, A. Yousif, Vinod Kumar, E. Coetsee. The Effect of Annealing Temperature on the Luminescence Properties of Y_2O_3 phosphor Powders Doped with a High Concentration of Bi^{3+}. *Journal of Luminescence* 180 (2016) 198–203. https://doi.org/10.1016/j.jlumin.2016.08.042

35. D.L. Dexter, James H. Schulman. Theory of Concentration Quenching in Inorganic Phosphors. *The Journal of Chemical Physics* 22 (1954) 1063–1070. https://doi.org/10.1063/1.1740265

36. Mingying Peng, Benjamin Sprenger, Markus A. Schmidt, Harald G. L. Schwefel, Lothar Wondraczek. Broadband NIR photoluminescence from Bi-doped $Ba_2P_2O_7$ crystals: Insights into the nature of NIR-emitting Bismuth centers. *Optics Express* 18 (2010) 12852–12863. https://doi.org/10.1364/OE.18.012852

37. Mathijs de Jong, Andries Meijerink. Color Tuning of Bi^{2+} luminescence in Barium Borates. *Journal of Luminescence* 170 (2016) 240–247. https://doi.org/10.1016/j.jlumin.2015.10.036

38. Renping Cao, Fangteng Zhang, Chenxing Liao, Jianrong Qiu. Yellow-to-Orange Emission from Bi^{2+}-doped RF_2 (R = Ca and Sr) Phosphors. *Optics Express* 21 (2013) 15728–15733. https://doi.org/10.1364/OE.21.015728

Chapter 5

Stability of Bi doped La_2O_3 powder phosphor and PMMA composites

5.1. Introduction

Lanthanum oxide (La_2O_3) is an important industrial material which is used extensively for catalysts, in the glass industry, for metal alloys (particularly rechargeable battery alloys) and for ceramics [1]. La_2O_3 has also been investigated as a phosphor host for lanthanide ions [2]. However, La_2O_3 must be handled with consideration due to its sensitivity to the atmosphere, since it reacts relatively quickly with the moisture (water) in the air to form lanthanum hydroxide ($La(OH)_3$) and can also react with atmospheric carbon dioxide in the presence of moisture to form carbonates [3]. Although a number of reports of the poor stability and atmospheric degradation of undoped La_2O_3 have been published previously [4, 5, 6], this important factor is only occasionally considered in papers dealing with La_2O_3 phosphors (e.g. for La_2O_3:Eu [7, 8] and La_2O_3:Ho [9]). In other phosphor studies of La_2O_3 it is often neglected (e.g. recently [10, 11, 12, 13]) and requires further attention. Research papers for applications of La_2O_3 other than phosphors also generally neglect its instability in the atmosphere and its reaction with water, most notably ongoing research on the biological effects of La_2O_3 [14, 15, 16] where an important consideration for understanding the interactions must be the initial transformation of La_2O_3 to $La(OH)_3$ in an aqueous environment [17].

In this work blue emitting La_2O_3:Bi phosphor powder was prepared by the sol-gel combustion method [18]. The product was annealed at 1200 °C and then exposed to atmosphere at 20 °C and 40% relative humidity for 7 days to assess its environmental stability. Although the La_2O_3 powder converted to $La(OH)_3$ within a few days, which was studied by X-ray diffraction (XRD), Fourier transform infrared spectroscopy (FTIR), photoluminescence (PL) and X-ray photoelectron spectroscopy (XPS), this could be prevented by simply storing the samples in a vacuum desiccator; or the crystal structure transformation could be easily reversed by annealing, which was investigated. Degradation of the La_2O_3 powder could be effectively slowed, but was not completely eliminated, by encapsulation in poly(methyl methacrylate) (PMMA) polymer. Unlike for La_2O_3:Eu [7, 8] and La_2O_3:Ho [9] phosphors for which the transformation of the host from oxide to hydroxide

affected the luminescence, but did not quench it entirely, the luminescence of La_2O_3:Bi was completely quenched. Simply the presence of its luminescence can be used to indicate that the transformation is not yet complete, which may be useful in monitoring the possible transformation during other applications of La_2O_3, e.g. ceramics and catalysis.

5.2. Experimental

A powder sample of $La_{2-x}O_3:Bi_{x=0.002}$ was prepared by the citric acid sol-gel combustion method [18] according to the reaction (neglecting waters of hydration)

$$[4\text{-}2x]La(NO_3)_3 + [2x]Bi(NO_3)_3 + 8C_6H_8O_7 \rightarrow 2La_{2-x}O_3{:}Bi_x + 6NO + 48CO + 32H_2O + 3N_2$$

where the Bi was assumed to substitute for La and the concentration was chosen for optimal luminescence based on our previous work [19]. An additional sample with higher Bi concentration (x = 0.01) was used for the XPS studies because low dopant concentrations are generally difficult to detect using this technique. Chemicals were used as purchased from Sigma Aldrich, with the purity of the nitrates being 99.999% and the citric acid being 99.5%. Following the combustion reaction, the resulting powder was first annealed in air at 1200 °C for 2 h prior to initial characterization. The environmental stability was studied by leaving the freshly prepared powder in the open atmosphere for 7 days at 20 °C and 40% relative humidity, during which time PL and XRD measurements were performed almost daily to investigate the hydroxylation process

$$La_2O_3 + 3H_2O \rightarrow 2La(OH)_3.$$

Scanning electron microscopy (SEM), FTIR and XPS measurements were performed only on the freshly prepared samples and after exposure to the atmosphere for a number of days (degraded samples). A portion of the freshly prepared sample was stored in a vacuum desiccator, instead of open to the atmosphere, to assess the effectiveness of this precaution in preventing hydroxylation. In addition, part of the degraded sample was re-annealed at various temperatures between 500 and 800 °C to investigate the reversal of the effects of hydroxylation.

Part of the freshly prepared $La_{2-x}O_3:Bi_{x=0.002}$ powder was encapsulated in PMMA polymers as follows: either 5 g, or 10 g, of PMMA was dissolved in 20 ml of chloroform and then 0.5 g of

$La_{2-x}O_3:Bi_{x=0.002}$ in 10 ml of chloroform was added. The mixed solution was kept in a bath maintained at 50 °C with continuous stirring using a magnetic agitator for 1 h until the solution turned into a transparent sticky gel. The gel was dried by direct heating on a hot plate maintained at 150 °C for 12 h. The resulting products were white films of composite material.

The phase composition of samples was characterized by XRD measurements using a Bruker D8 Advance diffractometer for which the Cu Kα X-rays (λ = 0.154 nm) were generated at an accelerating voltage of 40 kV with a current of 40 mA. The luminescence was measured at room temperature using a Cary Eclipse fluorescence spectrophotometer equipped with a 150 W xenon flash lamp. A JSM-7800F SEM was used to analyse the particle morphology. FTIR spectra of the powders were obtained using a Thermo Scientific Nicolet 6700 FT-IR instrument, for which pellets were prepared by mixing 0.002 g of sample with 0.2 g of KBr (heated in a drying oven at 70 °C for 12 h to eliminate moisture). The electronic states and chemical compositions were analysed using a PHI 5000 Versaprobe XPS system. The spectra were obtained by using a monochromatic Al Kα X-ray beam (1486.6 eV) generated by a 25 W, 15 kV electron beam. Scans were generally recorded with a pass energy of 23 eV (or 59 eV for the Bi dopant) after 2 min of sputter cleaning with a 2 kV Ar ion gun and Multipack software was used to analyse the different binding energy peaks using Gaussian fits. To compensate for charging, the binding energies were referenced to the C 1s peak of adventitious C at 284.5 eV as standard.

5. 3. Results and discussion

The XRD pattern of the freshly prepared $La_{2-x}O_3:Bi_{x=0.002}$ powder is shown in figure 5.1(a), together with data from JCPDS card #05-0602 for La_2O_3. The good match of all the observed peaks revealed that La_2O_3, with its hexagonal crystal structure, had been successfully synthesized with no impurity phases. From the Scherrer equation [20], using the average of eight diffraction peaks, the crystallite size was estimated as 87 ± 4 nm as shown in Table 5.1. The sample was exposed to the atmosphere at 20 °C and 40% relative humidity and remeasured daily for 5 days, for which the results are also given in figure 5.1(a). By comparing the patterns with the standard for $La(OH)_3$ (JCPDS card #05-0685), it was observed that mixed phases of the oxide and hydroxide existed with an increasing proportion of hydroxide from days 1 to 4, and that on day 5 (i.e. 120 h) the XRD pattern no longer contained any visible peaks from the oxide i.e. the sample had been completely transformed to $La(OH)_3$:Bi. The average crystallite size of the hydroxide was estimated as 22 ± 4 nm, as

shown in Table 5.1. Note that when the freshly prepared sample was stored in a vacuum desiccator, it did not show any perceptible degradation over a similar period, as shown by figure 5.1(b). Fleming *et al.* [5] examined the reactivity of lanthanum oxide powders in air and reported that La_2O_3 rapidly transformed to $La(OH)_3$ after exposure to atmosphere for 24 h at room temperature. Mendez *et al.* [6] studied the hydroxylation of La_2O_3 nanoparticles and reported a complete transformation to $La(OH)_3$ after 80 h. Long *et al.* [21] studied the stability of La_2O_3 produced by an ethanolamine-nitrate combustion process and reported that La_2O_3 changed completely to $La(OH)_3$ after 24 h. In this study, the conversion time (120 h) was slightly longer than previous reports. Although this may have been as a result of doping, this is considered unlikely, because Mendez *et al.* [7] also reported on the hydroxylation of La_2O_3:Eu nanoparticles and found complete hydroxylation after 35 h, which was shorter than the time they had reported for undoped samples. During the transformation from oxide to hydroxide the average crystallite size was significantly reduced (from ~87 to ~22 nm), showing that several crystallites of $La(OH)_3$ were formed from each crystallite of La_2O_3.

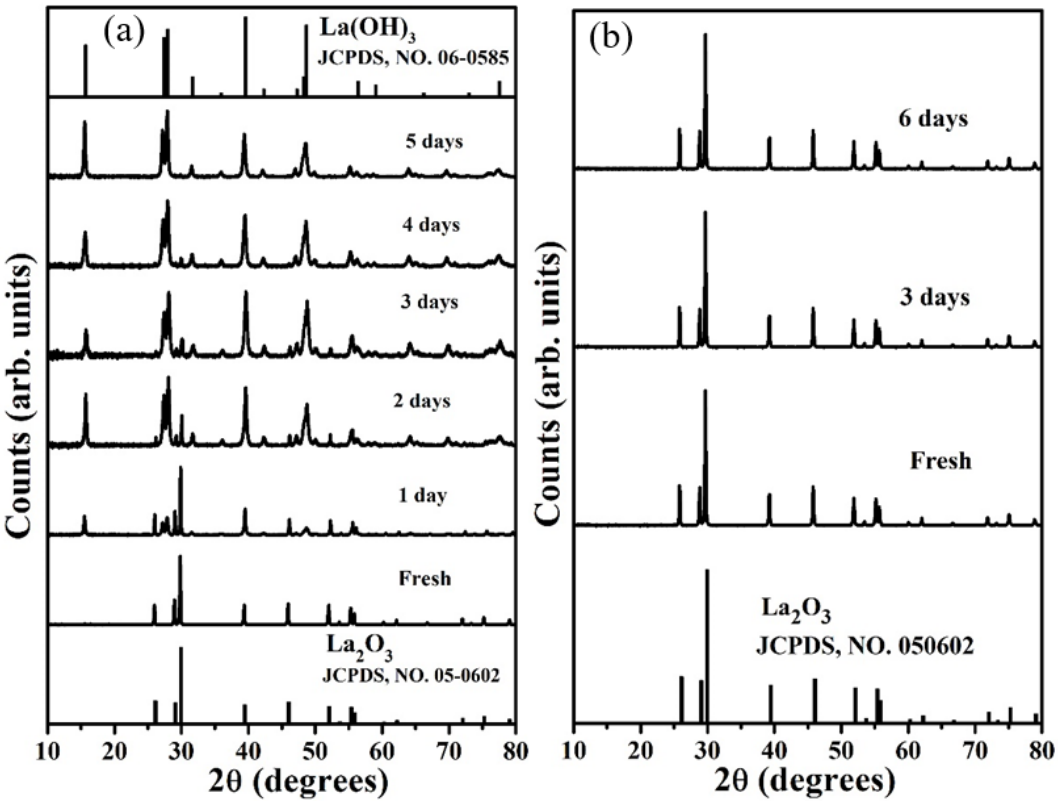

Figure 5.1: (a) XRD patterns of freshly prepared $La_{2-x}O_3$:$Bi_{x=0.002}$ powder initially and on subsequent days, when exposed to the atmosphere. The standards for La_2O_3 and $La(OH)_3$ are shown on the bottom and top, respectively. (b) XRD patterns of the same sample stored in a vacuum desiccator.

Table 5.1: Crystallite sizes calculated from the Scherrer equation.

Freshly prepared sample (oxide)		**Degraded sample after 5 days (hydroxide)**	
Diffraction peak	**Crystallite size (nm)**	**Diffraction peak**	**Crystallite size (nm)**
100	92	100	27
002	85	110	21
011	93	101	24
012	88	200	27
110	88	201	21
103	81	211	12
112	84	220	23
201	88	311	21
Average	**87 ± 4**	**Average**	**22 ± 4**

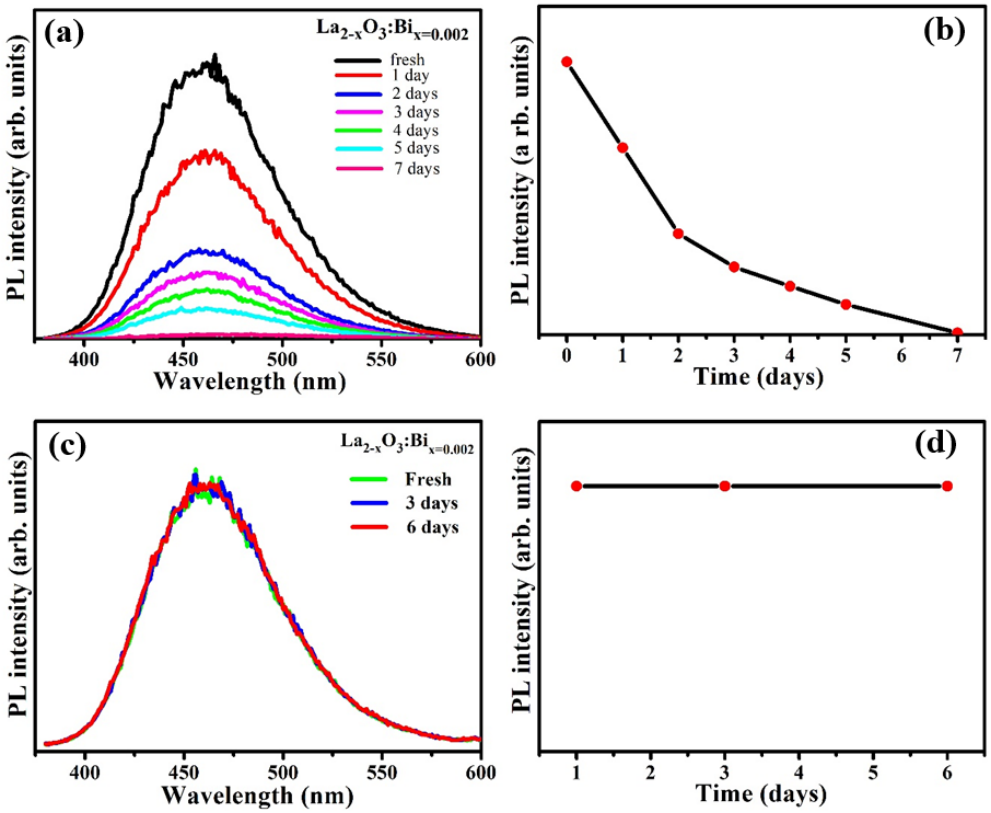

Figure 5.2: (a) PL emission spectra of freshly prepared $La_{2-x}O_3:Bi_{x=0.002}$ initially and on subsequent days, for 7 days. (b) Peak intensity as a function of time. (c,d) PL emission spectra and intensity as a function of time for the phosphor stored in a vacuum desiccator.

Figure 5.2(a) shows the PL emission spectra of the freshly prepared $La_{2-x}O_3:Bi_{x=0.002}$ phosphor powder initially and over time. The phosphor powder produced a broad band of blue fluorescence emission centred at 462 nm, when excited by 308 nm which was attributed to transitions from $^3P_1$ to $^1S_0$ levels in Bi^{3+} ions [22]. It was observed that the PL emission decreased daily and there was negligible remaining luminescence after 7 days. Figure 5.2(c) presents the PL emission of the freshly prepared sample stored in a vacuum desiccator, with figure 5.2(d) showing the peak intensity as a function of time. The PL intensity did not change, indicating that the phosphor does not degrade measurably when stored in a vacuum desiccator and that the phosphor can be stored effectively in this manner.

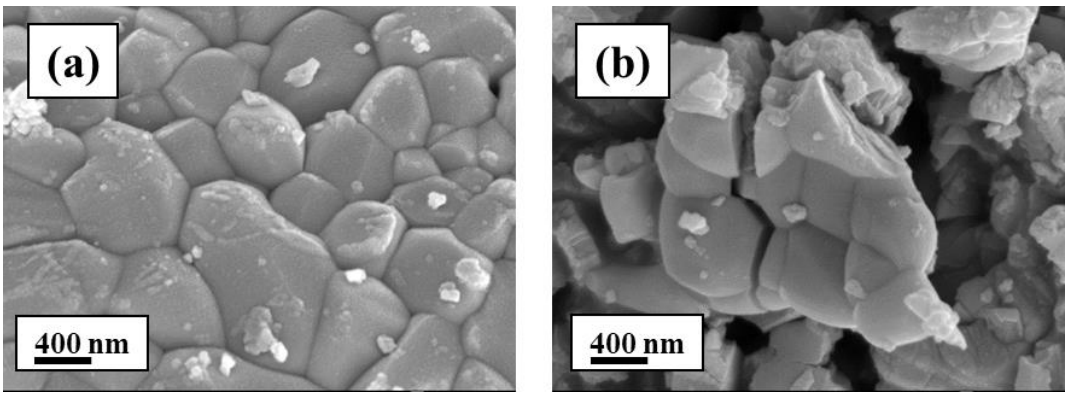

Figure 5.3: SEM micrographs of (a) freshly prepared La_2O_3 and (b) degraded sample after 5 days.

The surface morphology of the freshly prepared La_2O_3 powder phosphor and the degraded sample after 5 days was compared using SEM as shown in figure 5.3. The particles of La_2O_3 had an irregular shape and the average particle size was estimated to be about 620 nm, which is larger than the crystallite size estimated from XRD. Therefore each particle contains many crystallites. Figure 5.3(b) shows the morphology of the degraded sample. It consisted of smaller grains (about 485 nm) which were agglomerated, but fractures were present. The volume of La_2O_3 has been reported to increase significantly (~40-60% [5]) as it absorbs moisture and transforms to a hydroxide, which is considered as a possible cause of the fracturing. At the same time, the XRD results of this study showed that there was a significant reduction of the crystallite size. As a result of these opposing effects, the change in morphology during the transformation is expected to be complex. The origin of the small bright particles on the surface of the grains could be small pieces of material that resulted

from the breaking of particles when the sample was crushed. As the particles break, they might result in tiny fragments as seen in this image.

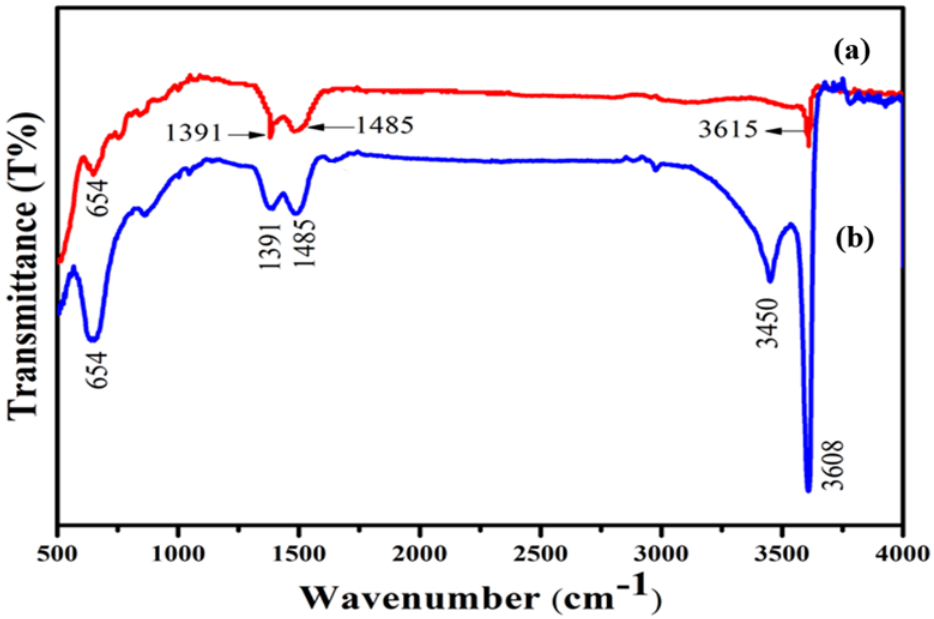

Figure 5.4: FTIR spectra of (a) freshly prepared La_2O_3 and (b) degraded sample after 5 days.

The FTIR spectra of the freshly prepared La_2O_3 powder and a degraded sample are shown in figure 5.4. The FTIR spectrum of the fresh sample in figure 5.4(a) revealed several absorption bands in the range 500 – 4000 cm^{-1}. Denning and Ross [23] measured the infrared absorption of La_2O_3 (taking care to avoid degradation) and reported peaks at 242, 386 and 435 cm^{-1}, which are all outside the range of the present measurement. Also spectra of La_2O_3 measured in the range 400 – 4000 cm^{-1} only showed absorption at the edge near 400 cm^{-1} [24]. This indicates that all of the peaks in figure 5.4(a) are due to impurities in the La_2O_3. The absorption bands centred at 1391 and 1485 cm^{-1} can be attributed to the presence of carbonates [25, 26, 27]. Although carbonates may form during degradation, since La_2O_3 can react with the CO_2 in the air, this was unexpected for the freshly prepared sample and instead the carbonates are likely to have been formed during synthesis using the combustion method with organic fuel and not have been completely eliminated by annealing, although being present in low enough concentration not to result in XRD peaks. The bands at 654 and 3615 cm^{-1} are due to bending and stretching modes of La-O-H groups [28], showing that even for the freshly prepared sample some hydroxide was present. This could have formed in the short time in contact with the environment, while mixing with KBr to form the pellet for measurement may also have introduced some moisture despite the precaution of drying the

KBr. In comparison to the fresh sample, the degraded sample showed similar carbonate peaks but much stronger absorption at 654 and 3608 cm^{-1} associated with the hydroxyl groups, revealing that degradation was mainly as a result of interaction of moisture from the atmosphere and that reaction with CO_2 was limited. The degraded sample also contained an absorption band at 3450 cm^{-1} not present in the fresh sample, which may result from the stretching mode of adsorbed water or from hydroxycarbonate phases [28] These observations confirmed the hydroxide formation after exposed to air as found by XRD (figure 5.1(a)), but showed that the XRD results were limited in that carbonate phases were below its detection limit.

Photoelectron spectra of lanthanum compounds are very complex [29] because photoionization of La^{3+} ions creates not only La^{4+} ions with a 3d core hole (state I), but also La^{3+} ions having a 3d core hole and a 4f electron transferred from neighbouring ligands (state II). The state II, which has higher binding energy than state I, splits into antibonding (IIa) and bonding (IIb) components [30] which are described as satellite peaks. Additionally, a plasmon peak also generally occurs at higher binding energy. All four of these peaks occur as doublets due to spin-orbit coupling, which causes $3d_{5/2}$ and $3d_{3/2}$ peaks having area ratio 3:2. Therefore four doublet peaks may occur for each bonding state of La^{3+} ions in the sample. Furthermore, when using an Al Kα X-ray source for XPS, the broad La $M_{4,5}N_{4,5}N_{4,5}$ Auger electron peak overlaps the higher binding energy region where the La $3d_{3/2}$ peaks occur and should ideally be subtracted before XPS fitting, as done by Sunding *et al.* [30]. Figure 5.5(a) and (e) show the measured La 3d binding energy regions for the freshly prepared and a sample degraded for 7 days, respectively, with the spin-orbit splitting of doublets being 16.8 eV. Amongst the background fits provided by the Multipak software, the Shirley background is the best, but still inadequate since it cuts through the measured spectrum near ~842 eV, which was also the case for Ogugua *et al.* [31]. The broad Auger band, which elevates the measured counts in the higher binding energy range (down to roughly 640 eV), hampers the background fitting algorithms, therefore we only fit the binding energy region less than 842 eV. This excludes all the La $3d_{3/2}$ peaks, as well as the La $3d_{5/2}$ plasmon peak, leaving only the La $3d_{5/2}$ state I, IIa and IIb peaks per unique site of La^{3+} ions in the sample. Although not all the La ions in La_2O_3 and $La(OH)_3$ are in equivalent environments, this is neglected and we consider only La ions in the oxide or hydroxide as possible states, therefore fitting six possible peaks. We further constrained the fitting model by fixing the binding energy separations based on the data of Sunding *et al.* [30] which are given in Table 5.2.

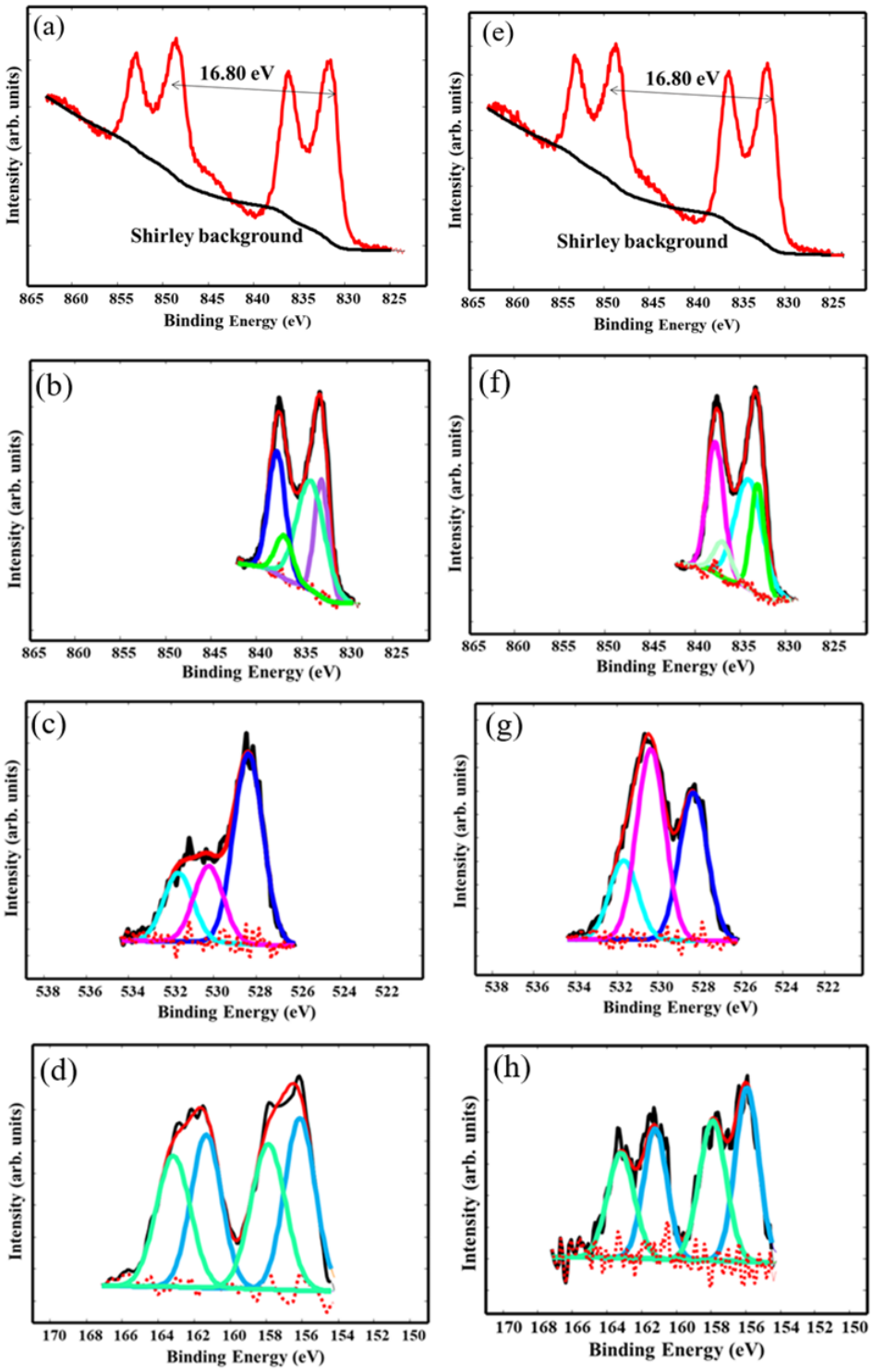

Figure 5.5: XPS spectra of freshly prepared $La_{2-x}O_3:Bi_{x=0.01}$ (a) La 3d (b) fit of lower binding energy part of the La 3d region (c) O 1s (d) Bi 4f. Similar spectra are shown in (e-h) for the degraded sample.

Figure 5.5(b) shows the resulting fit for the freshly prepared sample, for which the total areas corresponding to the oxide and hydroxide related peaks were found to be 89% and 11%,

respectively, which is consistent with La_2O_3 having a small amount of initial degradation due to a short exposure to the atmosphere when loading the sample. Figure 5.5(f) shows a fit using the same peak positions and widths for the degraded sample. The total of the hydroxide related peaks was 31%, which is higher than for the fresh sample although a value close to 100% was expected since the XRD and PL results had indicated a complete conversion of the degraded sample from oxide to hydroxide. This unexpected result may be due to limitations of the model used or challenges in fitting the six unresolved and closely separated peaks, while the X-ray beam or high vacuum environment may also cause the surface layer to convert from hydroxide to oxide [30]. Further work will be required for a better understanding to overcome the challenges of applying the La 3d XPS data for differentiating between La oxide and hydroxide. Instead, Fleming *et al.* [5] considered using the O 1s peak.

Table 5.2: Peak positions and areas for the freshly prepared and degraded samples.

	La_2O_3			**$La(OH)_3$**		
	I	**IIa**	**IIb**	**I**	**IIa**	**IIb**
Binding energy (eV)	832.8	834.0	837.7	833.0	834.9	836.9
Shift relative to La_2O_3 I state (eV)*	-	1.2	4.9	0.2	2.1	4.1
Area (%): fresh sample	21%	40%	28%	0	0	11%
	Total: 89%			Total: 11%		
Area (%): degraded sample	0	40%	29%	20%	2%	9%
	Total: 69%			Total: 31%		

*Fixed from the data of Sunding *et al.* [30].

Fleming *et al.* [5] modelled the O 1s binding energy region in terms of two peaks separated by 2.0 eV, with the lower binding energy peak attributed to O in La_2O_3 and the higher binding energy peak for O in $La(OH)_3$. Although this gave a plausible explanation of their data, Sunding *et al.* [30] reported that La_2O_3 alone produced two O 1s peaks having this separation and that $La(OH)_3$ produced an additional single peak at an intermediate binding energy. Note that Fleming *et al.* [5] had found both peaks in their sample which they had freshly removed from the oven and immediately placed in the XPS machine, but attributed the second peak to a reaction with atmospheric moisture and formation of some hydroxide during this short exposure time. In the crystal structure of La_2O_3 there are two possible La-O

bond lengths of ~2.34 and 2.71 Å, which differ significantly by about 15%, while in $La(OH)_3$ the possible La-O bond lengths are almost the same, namely 2.593 and 2.596 Å [32]. This gives a physical basis for the more complex model proposed by Sunding *et al.* [30] and therefore this was used to fit our measured data presented in figure 5.5 (c) and (g) for the fresh and degraded samples, respectively. In both cases the fitting indicated a mixture of oxide and hydroxide material, but as expected the middle peak corresponding to the hydroxide phase was much larger for the degraded sample than the freshly prepared one. Considering the surface sensitivity of the XPS technique, the presence of some hydroxide in the freshly prepared sample may be attributed to partial hydroxylation of the surface during the short time the sample was exposed to the atmosphere, while the unexpected remaining peaks associated with oxide in the degraded sample could be due to conversion of hydroxide to oxide on the surface due to the X-ray beam in the high vacuum environment [30]. These factors create significant uncertainty and mean that the XPS results can only be interpreted qualitatively. Figures 5.5 (d) and (h) show the Bi 4f binding energy regions for the freshly prepared and degraded samples, respectively. These can be fitted by two pairs of doublets, each having the expected spin-orbit separation of 5.3 eV [33]. The energy separation between the two doublets is almost 2 eV, while the Bi $4f_{7/2}$ binding energy in different oxide materials generally lies in a much smaller range of ~1 eV (between ~159-160 eV [33]). Therefore Bi^{3+} ions substituting La^{3+} ions in different sites of La_2O_3 or $La(OH)_3$ are extremely unlikely to have such a large binding energy difference. The Bi 4f binding energy of metallic Bi^0 is ~2 eV less than for Bi_2O_3 [34], suggesting that one of the doublets corresponds to Bi^{3+} ions and the other corresponds to metallic Bi nanoparticles. Such nanoparticles may have been formed by segregating Bi during annealing when the samples were initially annealed during preparation, or possibly as a result of Ar ion sputter cleaning of the samples. The co-existence of Bi_2O_3 and metallic Bi nanoparticles in pulsed laser deposited thin films which was reported by Eom *et al.* [35] produced similar XPS results.

Figure 5.6 presents XRD patterns of the degraded sample and portions of it that were re-annealed at different temperatures between 500 °C and 800 °C in air for 2 h. Annealing at 500 °C did not remove all hydroxide phase from the phosphor, but when the temperature increased to 600 °C the structure changed to pure La_2O_3 phases. The peaks became sharper (FWHM decreased) by increasing the annealing temperature, indicating that the crystallite size increased by increasing the annealing temperature. No measurements were made above

800 °C, since for that temperature the XRD data indicated good crystallinity and that the structure had reverted completely to La_2O_3.

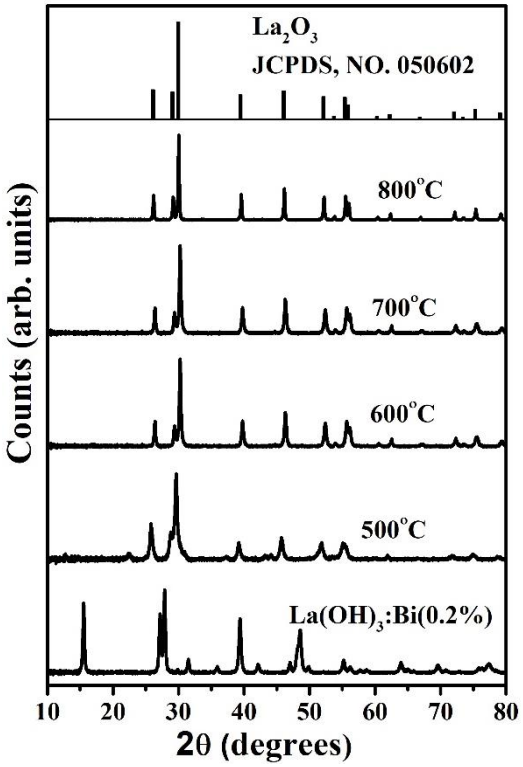

Figure 5.6: XRD pattens of the degraded sample and portions of it which were re-annealed at different temperatures in air for 2 h.

Figure 5.7 (a) shows PL emission spectra of portions of the degraded sample which were re-annealed at temperatures between 500 °C and 800 °C in air for 2 h. The PL emission intensity increased with increasing annealing temperature. For the highest temperature (800 °C) it was found that the blue PL emission was once again observed at about one third of the intensity of the freshly prepared samples. Figure 5.7(b) presents the PL emission intensity as a function of annealing temperature. It is unclear why the luminescence did not fully recover, suggesting that some residual defects which act as quenching sites remain despite the phase purity suggested by the XRD results. This is consistent with the carbonates revealed by FTIR (figure 5.4(a)) despite no impurity phases being observed in the sample. Alternatively, this may be caused by segregation of Bi ions to non-luminescent metallic Bi nanoparticles during annealing.

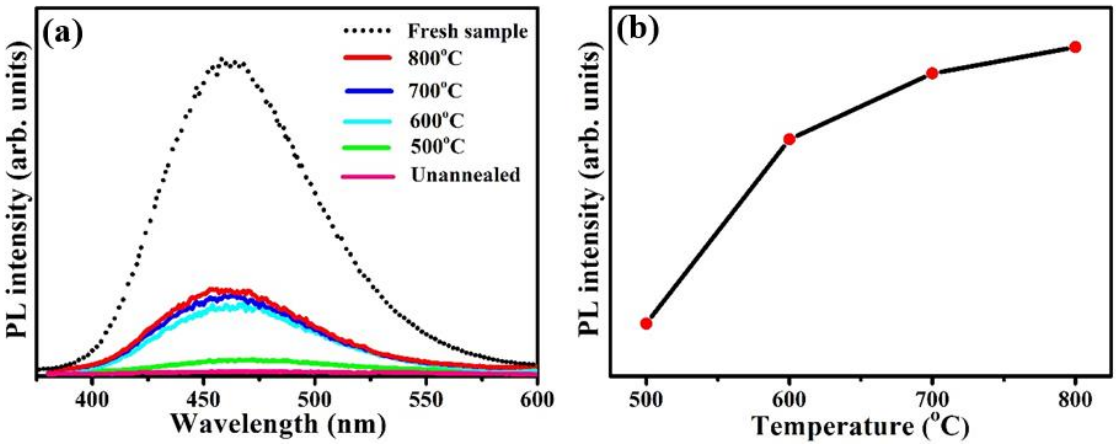

Figure 5.7: (a) PL emission spectra of the degraded sample immediately after re-annealing at different temperatures in air for 2 h. (b) Peak intensity as a function of annealing temperature.

Since for many applications it is impractical to store the phosphor in a vacuum desiccator or regularly anneal it, a trial was made to see if it could be effectively protected from atmospheric moisture by encapsulation in a polymer. PMMA was used to encapsulate the freshly prepared phosphor in order to protect it from the moisture in the atmosphere because PMMA is transparent and weather resistant [36]. Figure 5.8 shows the PL emission of a fixed mass (0.5 g) of phosphor powder mixed with either 5 g or 10 g of PMMA, respectively. For the sample mixed with 5 g of PMMA the PL emission intensity decreased significantly with time. However, by further increasing the PMMA up to 10 g, the PL emission intensity decreased rather more slowly. Although the degradation could not be eliminated, it was reduced significantly and further optimization studies or the use of other polymers may allow better results to be achieved in future.

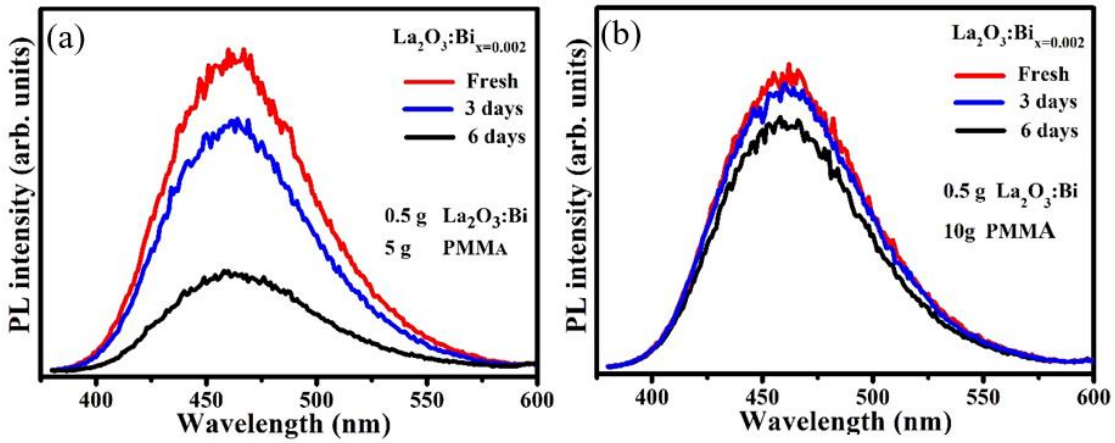

Figure 5.8: PL of $La_{2-x}O_3:Bi_{x=0.002}$ phosphor powder mixed with (a) 5 g (b) 10 g of PMMA.

5.4. Conclusion

Bi doped La_2O_3 was successfully synthesized by the sol-gel combustion method and a broad band of blue fluorescence emission centered at 462 nm was observed for excitation at 308 nm. The La_2O_3 host was found to be unstable under ambient conditions and converted to more stable $La(OH)_3$ due to its hygroscopic nature when exposed to the atmosphere. The change in crystal phase was confirmed by XRD and FTIR and was accompanied by a loss of luminescence. The O 1 s XPS spectra could be qualitatively explained by the formation of a new peak corresponding to $La(OH)_3$ in the degraded sample occurring at a binding energy between those of the double peak associated with La_2O_3. The degraded samples were re-annealed and it was found that the structure could be reverted completely to La_2O_3, while the blue PL emission was once again observed at about one third of the intensity as for the freshly prepared sample. For samples stored in a vacuum desiccator for one week, no change for XRD and PL were observed. Initial trials showed that the degradation was reduced significantly by encapsulation of the phosphor in a PMMA polymer. Although $La_{2-x}O_3:Bi_x$ can be used as a blue emitting phosphor, it is only suitable for applications where it will not be exposed to moisture in the atmosphere. Therefore, it may have an application as a moisture sensor, because while the luminescence remains high it is evidence that it has not been exposed to the atmosphere.

5.5. References

1. Georgios Charalampides, Konstantinos I. Vatalis, Baklavaridis Apostoplos, Benetis Ploutarch-Nikolas. Rare Earth Elements: Industrial Applications and Economic Dependency of Europe. *Procedia Economics and Finance* 24 (2015) 126–135. https://doi.org/10.1016/S2212-5671(15)00630-9

2. Zhenhe Xu, Shasha Bian, Jiaqi Wang, Tao Liu, Liming Wang, Yu Gao. Preparation and Luminescence of $La_2O_3:Ln^{3+}$ (Ln^{3+} = Eu^{3+}, Tb^{3+}, Dy^{3+}, Sm^{3+}, Er^{3+}, Ho^{3+}, Tm^{3+}, Yb^{3+}/Er^{3+}, Yb^{3+}/Ho^{3+}) Microspheres. *RSC Advances* 3 (2013) 1410–1419. https://doi.org/10.1039/c2ra22480a

3. Elena Haibel, Stefan Berendts, Dirk Walter. Thermogravimetric and X-Ray Diffraction Investigation on Carbonated Lanthanum Oxide and Lanthanum Hydroxide Formed in Humid CO_2 atmosphere. *Journal of Thermal Analysis and Calorimetry* 134 (2018) 261–267. https://doi.org/10.1007/s10973-018-7256-1

4. S. Bernal, F. J. Botana, R. García, J. M. Rodríguez-Izquierdo. Behaviour of Rare Earth Sesquioxides Exposed to Atmospheric Carbon Dioxide and Water. *Reactivity of Solids*

4 (1987) 23–40. https://doi.org/10.1016/0168-7336(87)80085-2

5. Peter Fleming, Richard A. Farrell, Justin D. Holmes, Michael A. Morris. The Rapid Formation of $La(OH)_3$ from La_2O_3 Powders on Exposure to Water Vapor. *Journal of the American Ceramic Society* 93 (2010) 1187–1194. https://doi.org/10.1111/j.1551-2916.2009.03564.x

6. M. Méndez, J. J. Carvajal, L. F. Marsal, P. Salagre, M. Aguiló, F. Díaz, P. Formentín, J. Pallarès, Y. Cesteros. Effect of the $La(OH)_3$ Preparation Method on the Surface and Rehydroxylation Properties of Resulting La_2O_3 Nanoparticles. *Journal of Nanoparticle Research* 15 (2013) 1479. https://doi.org/10.1007/s11051-013-1479-7

7. Maria Méndez, Yolanda Cesteros, Lluís Francesc Marsal, Alexandre Giguère, Dominique Drouin, Pilar Salagre, Pilar Formentín, Josep Pallarès, Magdalena Aguilo, Francesc Dìaz, *et al.* Effect of Thermal Annealing on the Kinetics of Rehydroxylation of Eu^{3+}:La_2O_3 Nanocrystals. *Inorganic Chemistry* 51 (2012) 6139–6146. https://doi.org/10.1021/ic300108f

8. Vesna Đorđević, Željka Antić, Marko G. Nikolić, Miroslav D. Dramićanin. Comparative Structural and Photoluminescent Study of Eu^{3+}-Doped La_2O_3 and $La(OH)_3$ nanocrystalline Powders. *Journal of Physics and Chemistry of Solids* 75 (2014) 276–282. https://doi.org/10.1016/j.jpcs.2013.10.004

9. Muhammad Ajmal, Tauseef Ali, Mohammad Adil Khan, Safeer Ahmad, Shabeer Ahmad Mian, Abdul Waheed, Sardar Ali. Structural and Optical Properties of La_2O_3:$Ho^{3+}$and $La(OH)_3$:Ho^{3+}crystalline Particles. *Materials Today: Proceedings* 4 (2017) 4900–4905. https://doi.org/10.1016/j.matpr.2017.04.093

10. Riya Dey, Vineet Kumar Rai. Yb^{3+} Sensitized Er3+ Doped La_2O_3 Phosphor in Temperature Sensors and Display Devices. *Dalton Transactions* 43 (2014) 111–118. https://doi.org/10.1039/c3dt51773j

11. Sk. Khaja Hussain, Goli Nagaraju, E. Pavitra, G. Seeta Rama Raju, Jae Su Yu. La(OH)3:Eu^{3+} and La_2O_3:Eu^{3+} Nanorod Bundles: Growth Mechanism and Luminescence Properties. *CrystEngComm* 17 (2015) 9431–9442. https://doi.org/10.1039/c5ce01688f

12. R. Jbeli, A. Boukhachem, I. Ben Jemaa, N. Mahdhi, F. Saadallah, H. Elhouichet, S. Alleg, M. Amlouk, H. Ezzaouïa. An Enhancement of Photoluminescence Property of Ag Doped La_2O_3 Thin Films at Room Temperature. *Spectrochimica Acta - Part A: Molecular and Biomolecular Spectroscopy* 184 (2017) 71–81. https://doi.org/10.1016/j.saa.2017.04.072

13. Neha Jain, Rajan Kr Singh, Amit Srivastava, S. K. Mishra, Jai Singh. Prominent Blue Emission through Tb^{3+} Doped La_2O_3 Nano-Phosphors for White LEDs. *Physica B:*

Condensed Matter 538 (2018) 70–73. https://doi.org/10.1016/j.physb.2018.03.014V

14. Brabu Balusamy, Burcu Ertit Taştan, Seyda Fikirdesici Ergen, Tamer Uyar, Turgay Tekinay. Toxicity of Lanthanum Oxide (La_2O_3) Nanoparticles in Aquatic Environments. *Environmental Sciences: Processes and Impacts* 17 (2015) 1265–1270. https://doi.org/10.1039/c5em00035a

15. Jing Liu, Ge Wang, Li Lu, Yuming Guo, Lin Yang. Facile Shape-Controlled Synthesis of Lanthanum Oxide with Different Hierarchical Micro/Nanostructures for Antibacterial Activity Based on Phosphate Removal. *RSC Advances* 7 (2017) 40965–40972. https://doi.org/10.1039/c7ra07521a

16. Lin Zhang, Lingyan Zhou, Qing X. Li, Hong Liang, Huaming Qin, Stephen Masutani, Brandon Yoza. Toxicity of Lanthanum Oxide Nanoparticles to the Fungus Moniliella Wahieum $Y12^T$ isolated from Biodiesel. *Chemosphere* 199 (2018) 495–501. https://doi.org/10.1016/j.chemosphere.2018.02.032

17. Mahnaz Ghiasi, Azim Malekzadeh. Synthesis, Characterization and Photocatalytic Properties of Lanthanum Oxy-Carbonate, Lanthanum Oxide and Lanthanum Hydroxide Nanoparticles. *Superlattices and Microstructures* 77 (2015) 295–304. https://doi.org/10.1016/j.spmi.2014.09.027

18. A. Yousif, R. M. Jafer, S. Som, M. M. Duvenhage, E. Coetsee, H. C. Swart. Ultra-Broadband Luminescent from a Bi Doped CaO Matrix. *RSC Advances* 5 (2015) 54115–54122. https://doi.org/10.1039/c5ra09246a

19. See chapter 4.

20. Kroon RE. Nanoscience and the Scherrer equation versus the 'Scherrer–Gottingen equation'. *South African Journal of Science* 109(5/6) (2013) Art. #a0019 (2 pages). http://dx.doi. org/10.1590/sajs.2013/a0019

21. Long Yulin, Jun Yang, Xiaoci Li, Weiya Huang, Yu Tang, Yuanming Zhang. Combustion Synthesis and Stability of Nanocrystalline La_2O_3 via Ethanolamine-Nitrate Process. *Journal of Rare Earths* 30 (2012) 48–52. https://doi.org/10.1016/S1002-0721(10)60637-0

22. Tadatsugu Minami, Toshihiro Miyata, Kouhei Ueda, Shun Matsui, Haruki Fukada. PL and EL Characteristics in New Blue Emitting La_2O_3:Bi Phosphor Thin Films. *ECS Transactions* 16 (2009) 39-45. https://doi.org/10.1149/1.3106670

23. J. H. Denning, S. D. Ross. The Vibrational Spectra and Structures of Rare Earth Oxides in the A Modification. *Journal of physics C: solid state physics* 11 (1972) 1123-1133. 1123 (1972). https://doi.org/10.1088/0022-3719/5/11/008

24. R. Paul Taylor, Glenn L Schrader. Lanthanum Catalysts for CH_4 Oxidative Coupling: A Comparison of the Reactivity of Phases. *Industrial & Engineering Chemistry Research* 30 (1991) 1016–1023. https://doi.org/10.1021/ie00053a025

25. R.P. Turcotte, J.O. Sawyer, L. Eyring. On the Rare Earth Dioxymonocarbonates and Their Decomposition. *Inorganic Chemistry* 8 (1969) 238–246. https://doi.org/10.1021/ic50072a012

26. T. Le Van, M. Che, J. M. Tatibouet, M. Kermarec. Infrared Study of the Formation and Stability of $La_2O_2CO_3$ During the Oxidative Coupling of Methane on La_2O_3. *Journal of Catalysis*, 142 (1993) 18-26. https://doi.org/10.1006/jcat.1993.1185

27. B. Klingenberg, M. Albert Vannice. Influence of Pretreatment on Lanthanum Nitrate, Carbonate, and Oxide Powders. *Chemistry of Materials* 8 (1996) 2755–2768. https://doi.org/10.1021/cm9602555

28. S. Bernal, F. J. Botana, R. García, J. M. Rodríguez-Izquierdo. Behaviour of Rare Earth Sesquioxides Exposed to Atmospheric Carbon Dioxide and Water. *Reactivity of Solids* 4 (1987) 23–40. https://doi.org/10.1016/0168-7336(87)80085-2

29. D. F. Mullica, C. K. Lok, H. O. Perkins, X-ray photoelectron final-state screeningin La(OH)3: a multiplet structural analysis, *Phys. Rev. B* 31 (1985) 4039–4042. https://doi.org/10.1103/PhysRevB.31.4039

30. M.F. Sunding, K. Hadidi, S. Diplas, O.M. Løvvik, T.E. Norby, A.E. Gunnæs. XPS Characterisation of in Situ Treated Lanthanum Oxide and Hydroxide Using Tailored Charge Referencing and Peak Fitting Procedures. *Journal of Electron Spectroscopy and Related Phenomena* 184 (2011):399–400. https://doi.org/10.1016/j.elspec.2011.04.002

31. Simon N. Ogugua, Hendrik C Swart, Odireleng M Ntwaeaborwa. The Dynamics of the Photoluminescence of Pr^{3+} in Mixed Lanthanum Yttrium Oxyorthosilicate Hosts. *Sensors & Actuators: B. Chemical* 250 (2017) 285-299. https://doi.org/10.1016/j.snb.2017.04.181

32. Vesna Đorđević, Željka Antićn, Marko G. Nikolić, Miroslav D. Dramićanin. Erratum to "Comparative structural and photoluminescent study of Eu^{3+}-doped La_2O_3 and $La(OH)_3$ nanocrystalline powders". *Journal of Physics and Chemistry of Solids* 75 (2014) 276–282. https://doi.org/10.1016/j.jpcs.2013.12.002

33. John F. Moulder, William F. Stickle, Peter E. Sobol, Kenneth D. Bomben. Jill Chastain (Editor). Handbook of X-ray Photoelectron Spectroscopy. Revised Edition. Perkin Elmer Corporation, Eden Prairie, Minnetsoa, USA (1992). ISBN: 978-0-9627026-2-4

34. Wenhua Zuo, Weihua Zhu, Dengfeng Zhao, Yunfei Sun, Yuanyuan Li, Jinping Liu and Xiong Wen (David) Lou. Bismuth oxide: a versatile high-capacity electrode material for

rechargeable aqueous metal-ion batteries. *Energy & Environmental Science* 9 (2016) 2881–2891. https://doi.org/10.1039/C6EE01871H

35. Ji-ho Eom, Hyun-june Jung, Jun-hee Han, Jeong-yong Lee, Soon-gil Yoon. Formation of Bismuth Nanocrystals in Bi_2O_3 Thin Films Grown at 300 K by Pulsed Laser Deposition for Thermoelectric Applications. *ECS Journal of Solid State Science and Technology* 3 (2014) 315–319. https://doi.org/10.1149/2.0101410jss

36. R.K. Goyal, S.S. Katkade, D.M. Mule. Dielectric, mechanical and thermal properties of polymer/$BaTiO_3$ composites for embedded capacitor. *Composites: Part B* 44 (2013) 128–132. http://dx.doi.org/10.1016/j.compositesb.2012.06.019

Chapter 6

Optical properties and stability of Bi doped La_2O_2S

6.1. Introduction

The luminescence of Bi^{3+} ions in different host materials varies from ultraviolet to green, making them attractive as activators for phosphors, and a recent survey of spectroscopic data for 117 hosts illustrates the continued interest in Bi-based luminescent materials [1]. Bi doped La_2O_3 was reported to have blue emission at 2.73 eV (454 nm) [1], but this host is unstable in the atmosphere and degrades over a period of about a day to form $La(OH)_3$ [2]. La_2O_2S (figure 6.1) has a similar crystal structure to La_2O_3, but with S replacing the O at Wyckoff site 1*a* [3]. It is sold as a commercial phosphor when doped with Eu and Tb, motivating us to investigate the optical properties and stability of Bi doped La_2O_2S and to compare the results with those reported for La_2O_3. The new spectroscopic data for La_2O_2S:Bi adds to the extensive listing [1] and provides additional information for considering quantitative models for the energies of excitation bands of Bi^{3+} ions [4, 5]. In some systems Bi doping may be considered as a possible alternative to Ce doping (e.g. as a sensitiser for Tb^{3+} ions [6]) and therefore it is also of value to consider the luminescence of Bi^{3+} ions in hosts such as La_2O_2S in which Ce^{3+} emission does not occur [7].

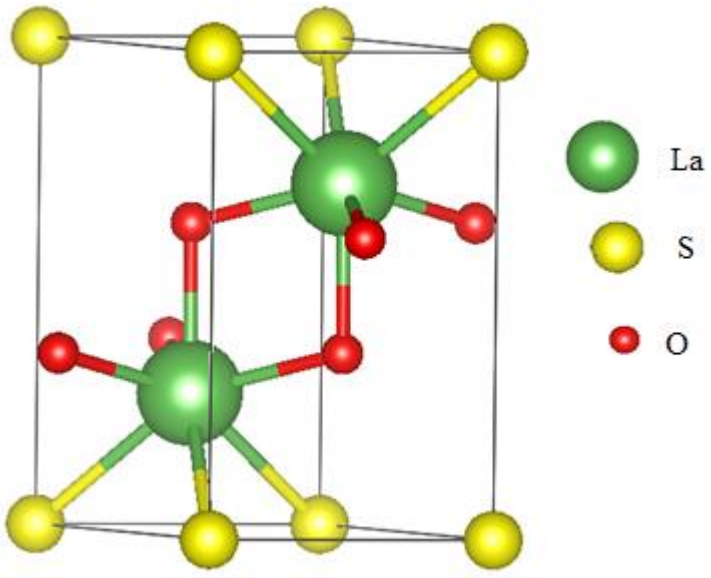

Figure 6.1: The unit cell of La_2O_2S drawn with the Vesta software [8].

Rare earth oxysulphide phosphors have been synthesized by various methods, such as the direct sulphidation of rare-earth oxides by a sulphur-containing gas (H_2S or CS_2) [9] and the reduction of the rare earth sulphates by H_2 or CO gas [10]. However, these gases are potentially harmful for human health and fine crystalline material can rarely be obtained by these methods [11]. In this study, La_2O_2S:Bi powder was prepared by the ethanol-assisted solution combustion method [12], using ethanol as a pre-ignition fuel and inexpensive thioacetamide as the sulphur-containing organic fuel. Its luminescence and environmental stability were measured and discussed in comparison to La_2O_3:Bi. Lifetime measurements to investigate the persistent luminescence of La_2O_2S:Bi are also presented.

6.2. Experimental

Powder samples of $La_{2-x}O_2S:Bi_x$ (x = 0, 0.001, 0.002, 0.003, 0.004, 0.006, 0.008 and 0.01) were prepared via the ethanol-assisted solution combustion method. Thioacetamide was employed as inexpensive sulphur containing organic fuel and was used with excess sulphur in the proportion S:La = 4:1 as described in the literature [12]. For the undoped host sample 1.2990 g of lanthanum nitrate ($La(NO_3)_3 \cdot 6H_2O$, 99.999%, purchased from Sigma Aldrich), 0.9015 g of thioacetamide (CH_3CSNH_2, Sigma-Aldrich, ≥ 99.0 %), 2.5 ml of ethanol and 7.5 ml of distilled water were mixed in a small glass beaker. Since Bi dopant was expected to be inserted by replacement of La, for doped samples an appropriate amount of $La(NO_3)_3 \cdot 6H_2O$ was substituted by an equal amount of bismuth nitrate ($Bi(NO_3)_3.5H_2O$, 99.999% purchased from Sigma Aldrich). The reaction beaker was heated at 80 °C under vigorous stirring for 10-15 minutes, after which about 6 ml of gel remained. This was transferred to a porcelain crucible which was placed into a muffle furnace maintained at 400 °C for 15 min. The combustion reaction created white fumes and a white powder was formed as the product. This as-prepared powder was annealed for 2 h in a reducing atmosphere (5% H_2 in Ar gas) at temperatures between 500 °C and 1000 °C.

The phase composition was characterized by X-ray diffraction (XRD) measurements using a Bruker D8 Advance diffractometer. The Cu Kα X-ray source was operated at an accelerating voltage of 40 kV and a current of 40 mA and emitted characteristic X-rays with wavelength 0.154 nm. XRD patterns were measured between $2\theta = 20°$ and 80° with a step of 0.02°. A JSM-7800F scanning electron microscope (SEM) was used to analyse the particle morphology. Inside the SEM the chemical composition was determined by energy dispersive X-ray spectroscopy (EDS) using an X-Max^{N}80 detector from Oxford Instruments. Diffuse

reflectance spectra were recorded using a Lambda 950 UV-vis spectrophotometer from PerkinElmer with a spectralon integrating sphere accessory. Initial photoluminescence (PL) properties of the powders were measured at room temperature using a Cary Eclipse spectrophotometer equipped with a 150 W xenon flash lamp and monochromator as excitation source, operating in phosphorescence mode with a delay time of 0.2 ms and gate time of 5 ms. Additional steady-state PL measurements were made using an FLS980 spectrometer from Edinburgh Instruments with a continuous 450 W xenon lamp. This instrument was also used to measure decay curves in the millisecond range using a xenon flashlamp, as well as in the nanosecond range using pulsed fixed wavelength light emitting diodes.

6.3. Results and discussion

6.3.1. Structural, morphology and chemical composition analysis

Figure 6.2(a) shows the XRD patterns of undoped La_2O_2S samples, both as-prepared and annealed at temperatures between 500 °C and 1000 °C, together with reference data for La_2O_2S (JCPDS no. 270263). The as-prepared sample showed a small amount of lanthanum oxysulphate ($La_2O_2SO_4$) impurity phase (marked with #, JCPDS no. 160501). Annealing at (or below) 800 °C did not remove this contaminant from the phosphor, but the sample annealed at 900 °C formed a pure La_2O_2S phase. Annealing at a higher temperature (1000 °C) caused formation of La_2O_3 (marked with *, JCPDS no. 050602). Therefore the doped samples of $La_{2-x}O_2S:Bi_x$ were annealed only at 900 °C and the XRD patterns of these samples are shown in figure 6.2(b). No additional diffraction peaks of other phases were detected, revealing that the Bi^{3+} ions had been successfully incorporated into the La_2O_2S host lattice. Also, no obvious shifting of the peak positions was observed for the doped samples, as seen from the magnified region near the 101 peak in figure 6.2(c). The crystallite sizes D of samples annealed at 900 °C were estimated from the full-width at half-maximum β of the more prominent diffraction peaks using the Scherrer equation [14] $D = \frac{0.9\lambda}{\beta cos\theta}$, where λ is the X-ray wavelength and θ is the Bragg angle. The results are summarized in Table 6.1 and show that the average crystallite size (~ 26 nm) was in the nanoscale region and not significantly affected by doping.

Table 6.1: Crystallite sizes (nm) of the $La_{2-x}O_2S:Bi_x$ samples annealed at 900 °C.

Peak	x = 0	x = 0.001	x = 0.002	x = 0.004	x = 0.006	x = 0.008	x = 0.01
101	28	28	25	28	27	28	26
102	29	29	26	27	26	26	27
110	28	28	27	26	27	28	26
103	25	25	26	23	25	23	24
200	24	21	25	21	21	27	21
201	27	27	30	25	28	25	27
Average	**27±2**	**26±2**	**26±2**	**25±2**	**25±2**	**26±2**	**25±2**

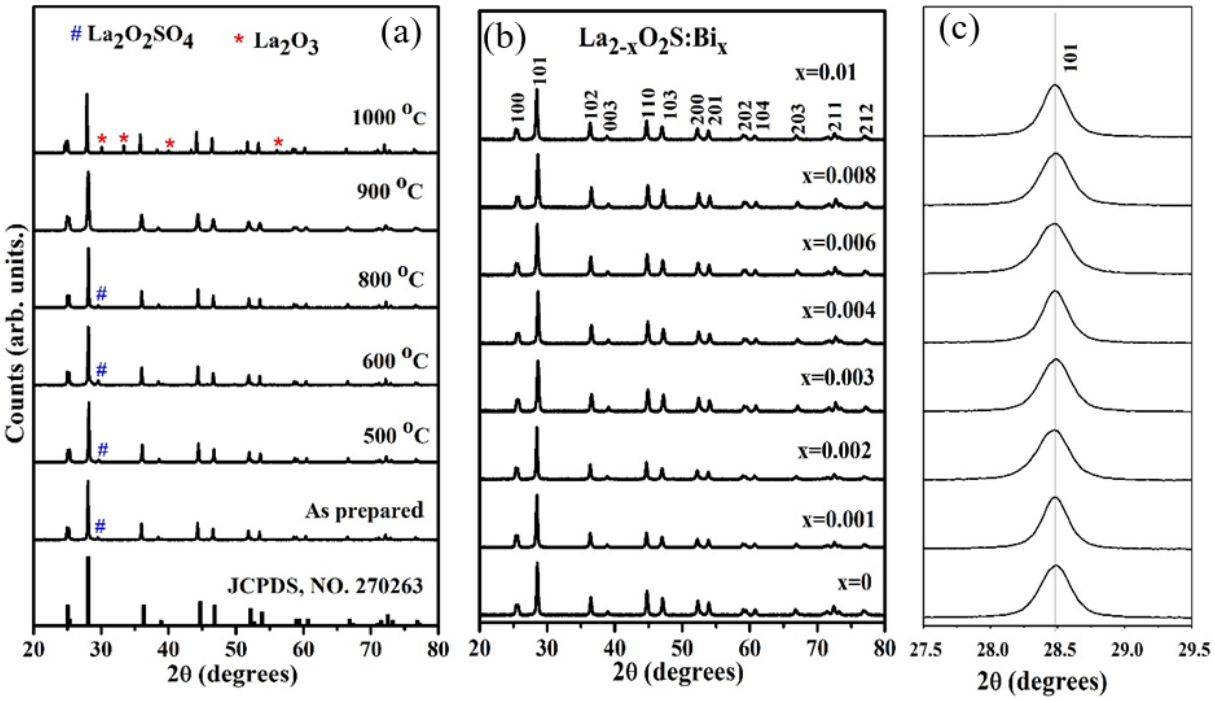

Figure 6.2: (a) XRD patterns for the undoped La_2O_2S samples, as-prepared and annealed, together with reference data of La_2O_2S (JCPDS card no. 270263). (b) XRD patterns of doped $La_{2-x}O_2S:Bi_x$ powders annealed at 900 °C. (c) Magnified view of the 101 main diffraction peak for doped samples.

Figure 6.3 shows the SEM images of (a) undoped La_2O_2S and (b) doped $La_{2-x}O_2S:Bi_{x=0.01}$ phosphor powders annealed at 900 °C, together with their EDS spectra in (c) and (d) respectively. For the undoped sample (figure 6.3(a)) the particles aggregated and had irregular shapes. When the Bi^{3+} ions were incorporated in the La_2O_2S host lattice (figure 6.3(b)) the particle size and morphology were similar to the undoped sample. The EDS

spectrum of the undoped sample (figure 6.3(c)) confirmed the presence of all the host elements (La, S and O) as expected, while that of the doped sample (figure 6.3(d)) was similar to the host sample. Although Bi X-rays of energy 2.419 keV may be expected, this, however, overlaps with the high-energy side of the S peak as indicated by the black line in figure 6.2(d) and the Bi was not detected due to its low concentration.

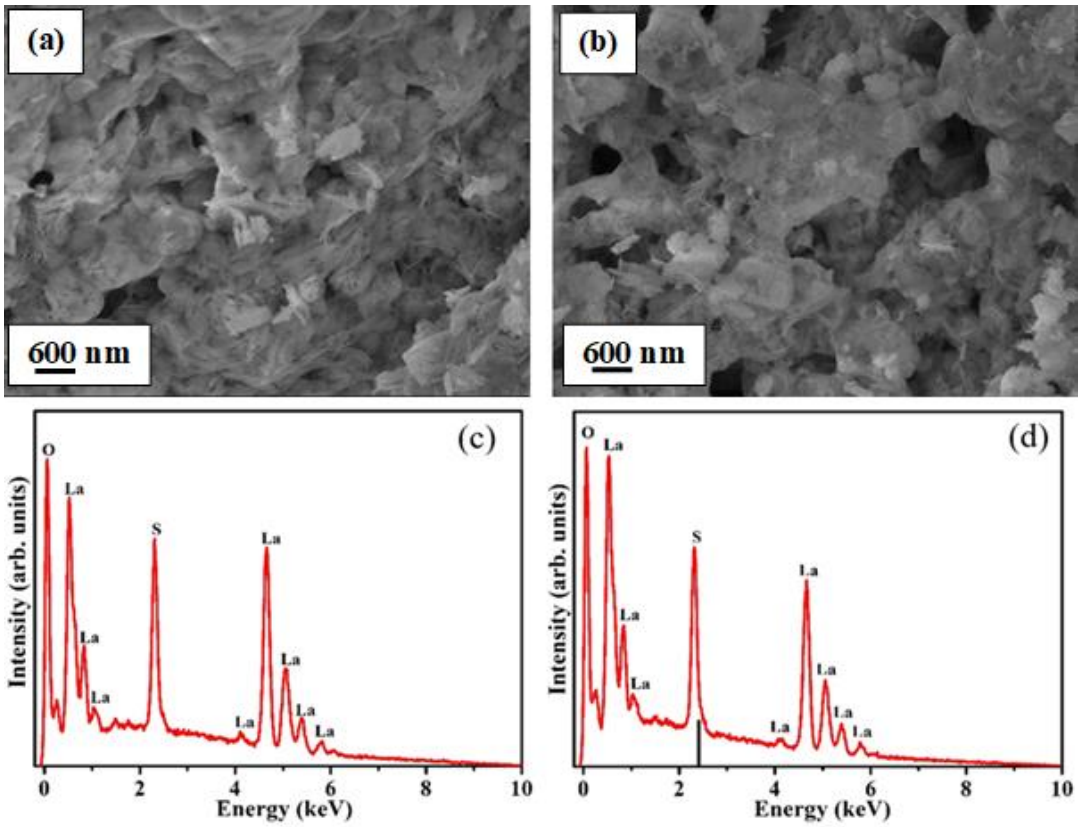

Figure 6.3: SEM images of (a) La_2O_2S and (b) $La_{2-x}O_2S:Bi_{x=0.01}$ phosphor powders annealed at 900 °C. Below the figures are the EDS spectra corresponding to (c) La_2O_2S and (d) $La_{2-x}O_2S:Bi_{x=0.01}$ respectively. The line located at 2.419 eV shows the expected position of the Bi dopant peak.

6.3.2. Diffuse reflectance spectra and band gap calculation

Diffuse reflectance spectroscopy was used to study the absorption characteristics of the La_2O_2S pure host and the effects of Bi when incorporated in the host lattice, as presented in Figure 6.4(a). For the host as well as doped samples the diffuse reflection (R_∞) decreased dramatically below 253 nm, which was attributed to absorption above the band gap. An absorption band centered at 344 nm was only present in the doped samples and was therefore attributed to absorption by the Bi^{3+} ions. The Kubelka-Munk function $F(R_\infty) = \frac{(1-R_\infty)^2}{2R_\infty}$ can

be used to convert the diffuse reflectance measurements to values proportional to the absorption [15]. For an indirect band gap material such as La_2O_2S, a Tauc plot of $[F(R_\infty)h\nu]^{1/2}$ versus $h\nu$ (the photon energy) can then be used to determine the optical band gap by fitting a linear region and extrapolating this to where it cuts the horizontal (energy) axis [16]. Such a plot is shown in figure 6.4(b) for the La_2O_2S host, from which the band gap was estimated to be 4.90 eV. The band gap of La_2O_2S was previously determined to be 4.6 eV by Jingbao *et al.* [17], while Vali reported it to be 4.35 eV [18]. The differences in band gap values may be due to the different preparation methods which influence the particle size, morphology and defects.

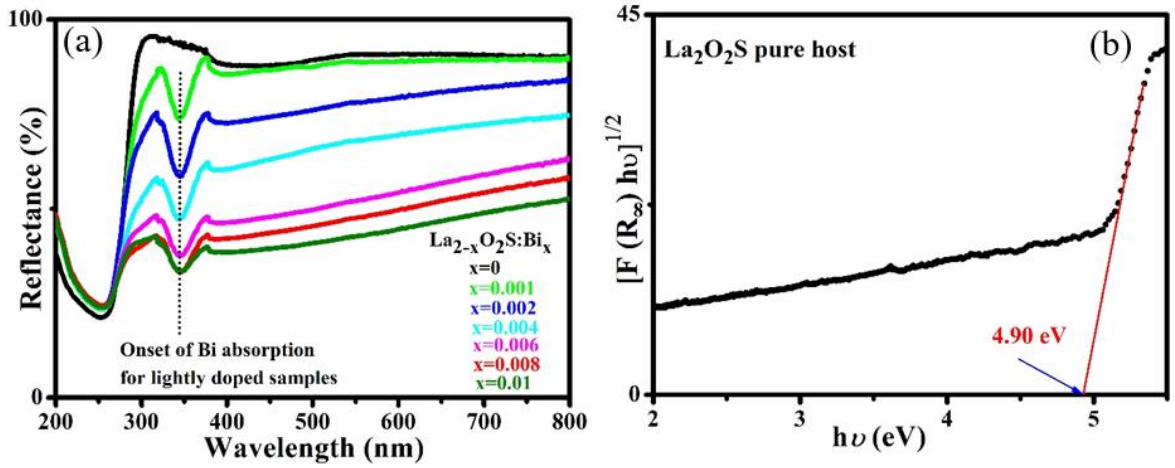

Figure 6.4(a) Diffuse reflectance spectra of La_2O_2S pure host and doped samples. (b) A Tauc plot to obtain the indirect optical band gap of undoped La_2O_2S.

6.3. 3. Photoluminescence (PL) analysis

Figure 6.5(a) shows the steady-state PL excitation spectra of $La_{2-x}O_2S:Bi_x$ activated with different Bi concentrations for blue emission at 456 nm. Two main peaks centred at 260 nm and 344 nm occur, with a shoulder at 298 nm. The excitation at 344 nm corresponds to the absorption band of the dopant observed in the reflectance spectra of figure 6.4(a) and exciting the sample at 260 nm (figure 6.5(b)) or 344 nm (figure 6.5(c)) both produced a similar broad blue emission band in the range 360 nm – 700 nm, centred at 456 nm. Figure 6.5(d) shows the emission intensity of the samples excited at 260 nm and 344 nm as a function of Bi doping concentration. For an excitation of 344 nm the maximum emission occurring for the lowest doping concentration considered (x = 0.001), but when the phosphor excited by 260 nm the emission was always stronger and the maximum occurred for x = 0.002, which is therefore considered the optimal Bi doping concentration. The relatively low optimal

concentration (within the range 0.001 to 0.01) suggests a strong electric dipole or quadrupole interaction between the Bi^{3+} ions for the model where concentration quenching is the result of migration of energy between the activators [19].

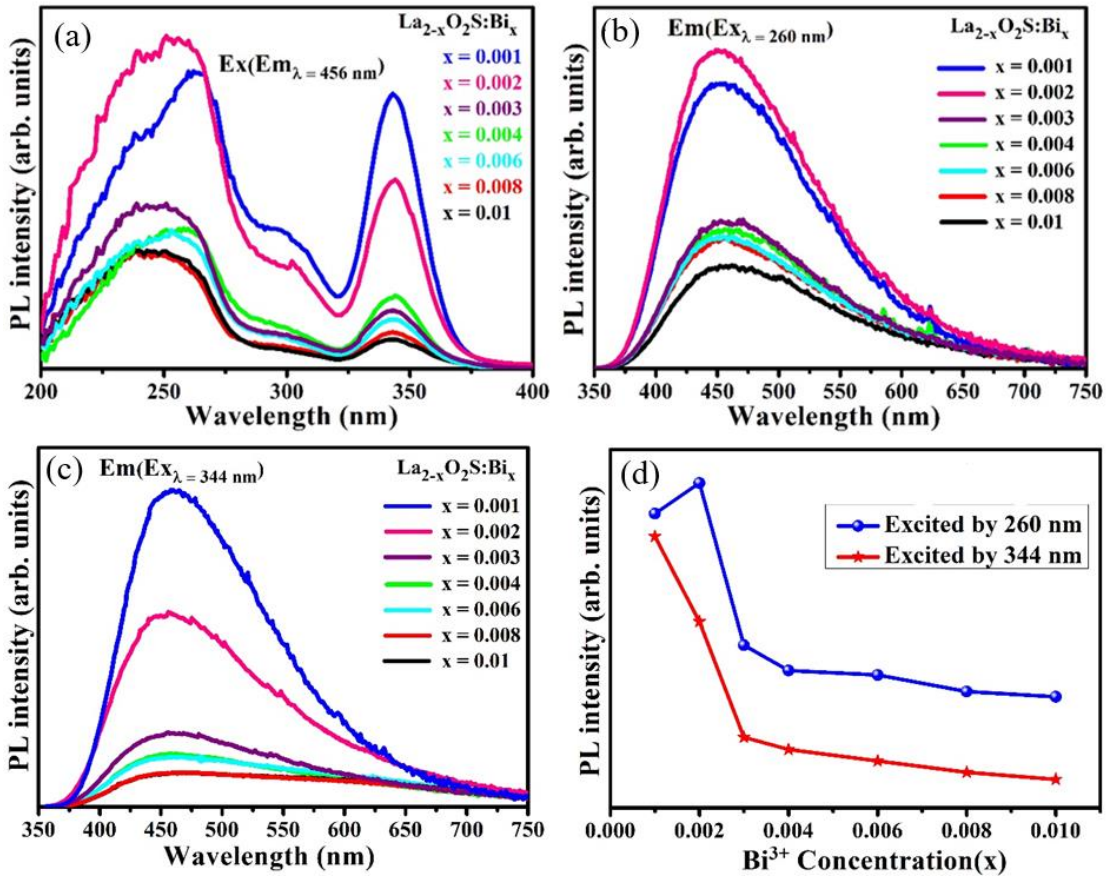

Figure 6.5: (a) Excitation spectra of $La_{2-x}O_2S:Bi_x$ doped with various Bi^{3+} ion concentrations. Corresponding PL emission spectra under the excitation of (b) 260 nm and (c) 344 nm. (d) Emission peak intensity as a function of Bi concentration.

The ground state of the Bi^{3+} ion $6s^2$ configuration is $^1S_0$, while the excited $6s^16p^1$ configuration has four energy levels, namely $^3P_0$, $^3P_1$, $^3P_2$ and $^1P_1$, in order of increasing energy. Although transitions from the $^1S_0$ ground state to the ^3P_J excited states are spin-forbidden, spin-orbit coupling of the $^1P_1$ and $^3P_1$ levels means that transitions to the $^3P_1$ become possible and absorption from $^1S_0$ to $^3P_1$ (A band) and $^1P_1$ (C band) levels are generally observed for Bi^{3+} ions. An intermediate absorption band (B band) corresponding to transitions from $^1S_0$ to $^3P_2$ is made possible by coupling with unsymmetrical lattice vibrational modes, although the $^1S_0$ to $^3P_0$ transition is strongly forbidden [20]. In addition, a charge transfer (D band) may also occur. In this context, the emission at 456 nm (2.72 eV) is

attributed to emission from the excited $^3P_1$ level to the ground state, while the excitation at 344 nm (3.60 eV) is attributed to the A band absorption, giving a Stokes shift of 0.88 eV. The weak excitation at 298 nm (4.16 eV) and the stronger excitation at 260 nm (4.77 eV) may then be tentatively associated with the B and C bands respectively. To motivate this, note that Lili Wang *et al.* [21] obtained a relationship between the energies of the A and C bands, namely $E_C = 3.236 + 2.290(E_A - 2.972)^{0.856}$ for values in eV. Taking $E_A = 3.60$ eV gives $E_C = 4.78$ eV, which is in good agreement with the experimental value of 4.77 eV assigned to the C band, the peak position of which varies somewhat unsystematically with doping concentration in figure 6.5(a). The theoretical position of the D band, corresponding to a metal-to-metal charge transfer (MMCT) from the Bi^{3+} ion to the La^{3+} cations of the host and giving the energy from the ion ground state to the host conduction band, can be calculated using the theory of Boutinaud [5], namely $E_{MMCT} = 55\,000 - 45\,500\chi/d$ (in cm^{-1}), where χ is the electronegativity of the host cations and d is the distance between the Bi^{3+} and host cations (in Å). The electronegativity of 7-coordinated La^{3+} ions was taken as $\chi = 1.301$ [22], while the distance between the La^{3+} cations in La_2O_2S is 3.853 Å [23]. This value was used as the La^{3+}-Bi^{3+} separation, since there is negligible difference of the ionic radii of these ions which can be taken as identical [5]. Therefore $E_{MMCT} = 39\,600 \pm 3000$ cm^{-1} (corresponding to 254 ± 19 nm or 4.91 ± 0.37 eV) with the error estimate being taken from Boutinaud [5]. The estimated energy of the MMCT transition, although having quite a large uncertainty, is therefore only slightly larger than the energy of the C band (4.78 eV) and the short wavelength excitation peak in figure 6.5(a) is probably as a result of both these sources.

The luminescence and reflectance data measured in this work allowed the construction of an energy level diagram for Bi doped La_2O_2S. Figure 6.6 shows a schematic diagram of the energy levels involved in the optical properties of $La_{2-x}O_2S:Bi_x$. The band gap, from the diffuse reflection results, was taken as 4.90 eV. From the calculation of the MMCT energy, the bottom of the $^1S_0$ level was located at about 4.91 ± 0.37 eV below the host conduction band, therefore based on this the $^1S_0$ level was taken to coincide with the valence band and used as the reference level. The excitation energies of the A, B and C bands (3.60, 4.16 and 4.77 eV, respectively) were then used to estimate the positions of the $^3P_1$, $^3P_2$ and $^1P_1$ energy parabolas, such that the Stokes shift and emission wavelength matched the experimental values. Although the position of the $^3P_0$ level parabola could not be established from the data in this study, it is generally located at an energy only very slightly below the $^3P_1$ level [24] and has been drawn accordingly.

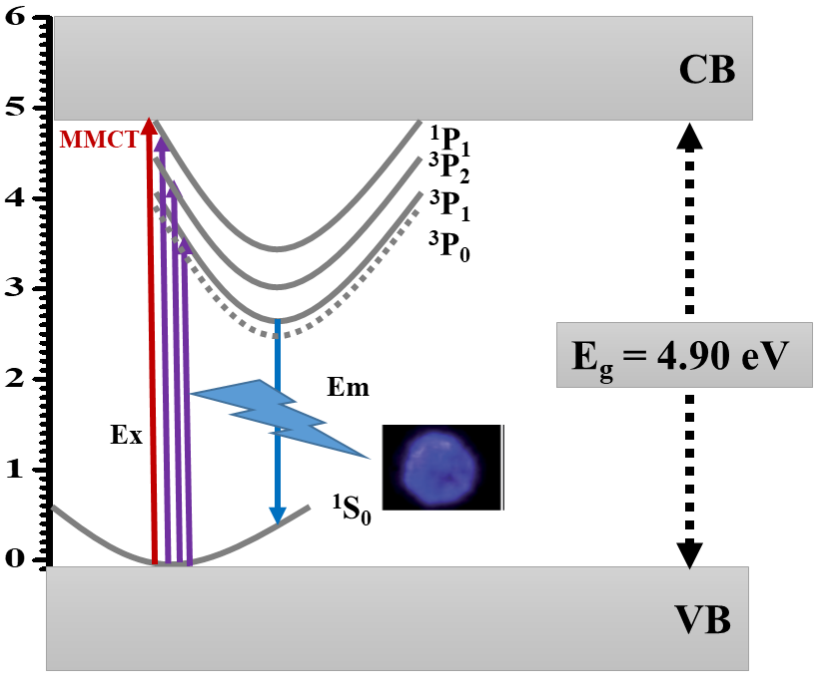

Figure 6.6: Energy level diagram for Bi doped La_2O_2S.

In addition to having similar crystal structures, La_2O_2S and La_2O_3 have approximately the same maximum phonon energies of ~400 cm^{-1} [25] and it is of interest to compare them as phosphor hosts. Joon Jae Oh *et al.* [26] reported that Eu^{3+} doped La_2O_2S exhibited stronger emission intensities than La_2O_3, which they attributed to a greater spontaneous emission rate associated with the crystal field resulting from mixed anions. Since the oxysulphide host exhibits an additional charge transfer band for Eu^{3+} associated with S (together with the charge transfer band associated with O), together with the fact that the La_2O_3 sample in that study was contaminated with $La(OH)_3$, makes a clear comparison of the hosts difficult. Figure 6.7 compares the steady-state PL excitation and emission properties of the $La_2O_2S:Bi_{x=0.002}$ powder of this study to an optimized Bi-doped La_2O_3 sample from our previous work [27], both having the same Bi doping concentration. The emission wavelength of Bi^{3+} ions in the La_2O_3 host was only marginally longer (462 nm) and the emission band was less broad: the colours are compared on the Commission internationale de l'éclairage (CIE) diagram in figure 6.7(b). La_2O_2S:Bi phosphor was found to have similar emission colour as La_2O_3:Bi, although less pure and closer to the centre of the CIE diagram. While La_2O_2S:Bi has an excitation maximum at 260 nm via the C band (with the MMCT transition also probably making a contribution to this excitation band) and can also be excited at 344 nm via the A band, the maximum excitation of La_2O_3 is via its A band at 308 nm, while its

weaker excitation at shorter wavelength was attributed only to its MMCT band rather than its C band. Therefore significant differences exist in the excitation spectra of Bi^{3+} ions in these hosts. The maximum luminescence intensity for Bi^{3+} in the La_2O_2S host was about half that in La_2O_3. Note that the oxysulphide samples were annealed in a reducing atmosphere, while the oxide material was annealed in air, so for the La_2O_2S some Bi^{3+} ions may have been reduced to Bi^{2+} ions which have been reported to emit in the yellow-orange region [28, 29] or to non-luminescent Bi atoms with possible evaporation loss of Bi from the surface when annealed in the reducing atmosphere. Alternatively, the broader emission band of La_2O_2S:Bi may be due to greater perturbations at the Bi^{3+} ions being induced by the crystal field of La_2O_2S compared to La_2O_3 [26] due to it having mixed anions.

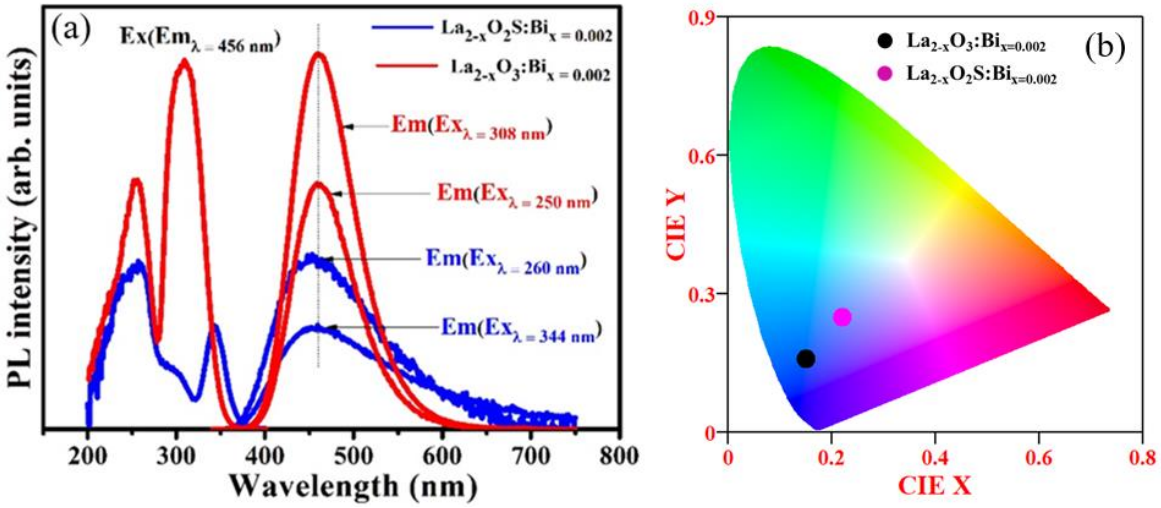

Figure 6.7: Comparison of (a) the excitation and emission spectra and (b) CIE coordinates of $La_2O_2S:Bi_{x=0.002}$ annealed in a reducing atmosphere at 900 °C with $La_2O_3:Bi_{x=0.002}$ annealed in air at 1200 °C, both for 2 h..

Although the maximum emission intensity of La_2O_3:Bi exceeded that of La_2O_2S:Bi, it degrades when exposed to the atmosphere [30]. Figure 6.8(a) shows the PL emission spectra of the $La_{2-x}O_2S:Bi_{x=0.002}$ sample from this study monitored for 60 days after its synthesis, showing that the oxysulphide host is stable and has negligible environmental degradation. Its maximum intensity versus time is compared with that of the optimum $La_2O_3:Bi_{x=0.002}$ sample in figure 6.8(b). This shows that using La_2O_2S:Bi instead of La_2O_3:Bi will allow one to obtain a fairly similar emission while avoiding the serious problem of degradation.

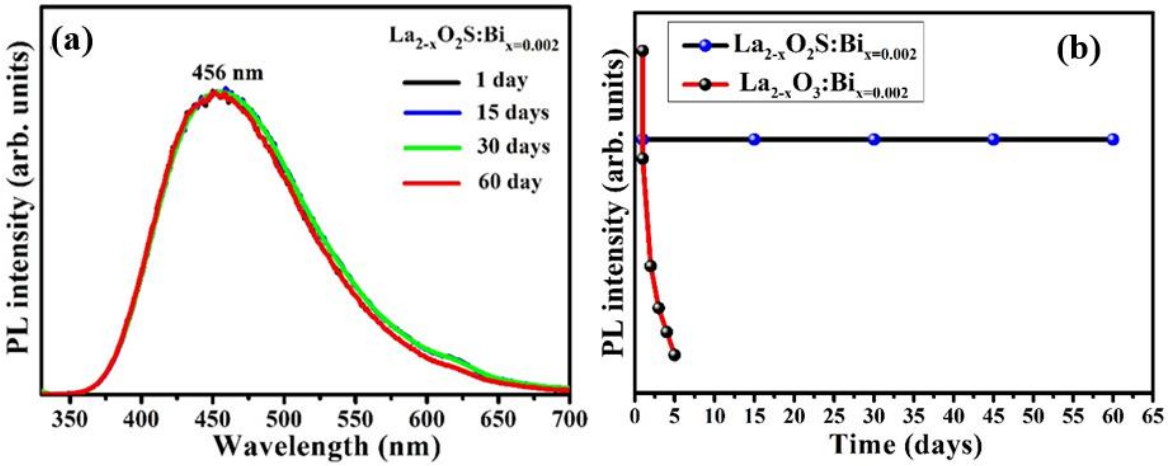

Figure 6.8: (a) PL emission of $La_{2-x}O_2S:Bi_{x=0.002}$ excited at 260 nm exposed to air for 60 days. (b) PL intensity of $La_{2-x}O_2S:Bi_{x=0.002}$ with time, compared to $La_{2-x}O_3:Bi_{x=0.002}$ which is unstable and shows rapid degradation.

The lifetime of the $^3P_1 \rightarrow {}^1S_0$ transition of Bi^{3+} ions is generally between 10 ns and 1 μs [31], but phosphorescence-mode measurements of $La_2O_2S:Bi$ using a Cary Eclipse spectrophotometer for a delay time of 200 μs still showed significant luminescence for which the emission and excitation spectra are presented in Figure 6.9(a). The form of emission curves matched those measured under steady-state excitation given in figure 6.5 and the peak positions in the excitation curves shown in figure 6.9(a) were similar to that for steady-state measurements, although their relative intensity was changed – with the longer wavelength excitation being relatively smaller. Figure 6.9(b) shows the emission intensity of the samples excited at 255 nm and 344 nm as a function of Bi doping concentration, having a similar trend to the steady-state measurements (figure 6.5(d)). The unexpected long lifetime emission from the $La_2O_2S:Bi$ samples, which did not occur for $La_2O_3:Bi$ samples, prompted measurements of the decay curve characteristics for the oxysulphide based phosphors.

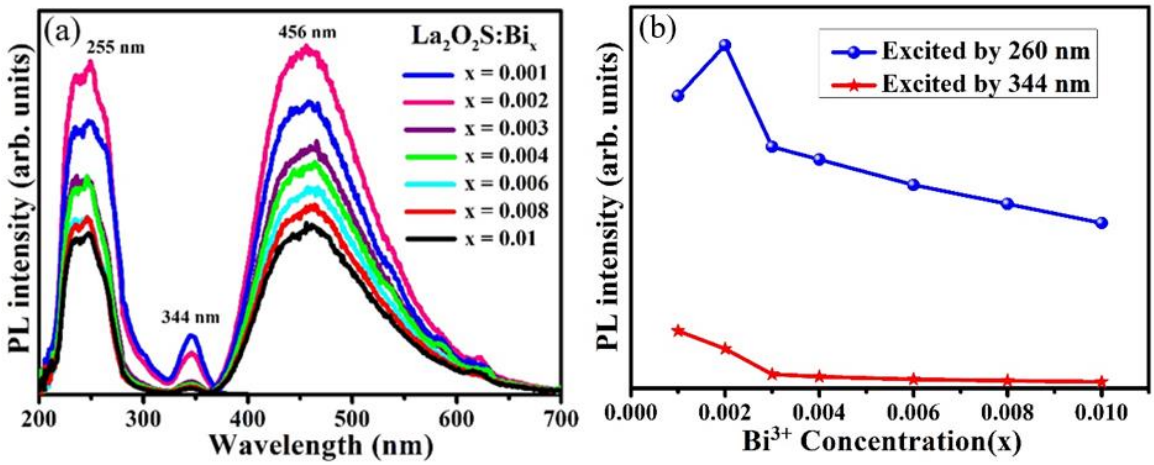

Figure 6.9: (a) Phosphorescence excitation and emission spectra of La_2O_2S doped with different Bi concentrations annealed at 900 °C in a reducing atmosphere (5% H_2 in Ar gas) for 2 h. (b) Emission peak intensity as a function of Bi concentration.

Decay curves for emission at 456 nm were measured with the FLS980 fluorescence spectrometer using two time scales. For the longer time period (100 ms) a pulsed xenon lamp with pulse width ~2 μs flashing at 10 Hz was used as the light source and data was collected using multi-channel scaling. The lamp was set to flash 0.5 ms into each cycle and the detector was gated to begin measurement 0.1 ms after the flash, for 99 ms. The decay curves were almost identical for different Bi doping concentrations and are shown for x = 0.002 and x = 0.006 in figure 6.10(a). The negligible detector dark counts signal is also shown for comparison, illustrating that the samples were still emitting after 100 ms. Challenges in fitting the decay curves of the well-know persistent luminescence phosphor $SrAl_2O_4:Eu^{2+},Dy^{3+}$ have been surveyed by Tsai *et al.* [32] and a quantitative analysis for La_2O_2S:Bi will only be attempted in later work. The similarity of the excitation spectra for persistent luminescence (figure 6.9(a)) and steady-state luminescence (figure 6.5(a)) indicates that the traps could be activated by exciting the Bi^{3+} ions directly (344 nm, A band), but more strongly by exciting at 255 nm (C band), which may also have resulted in MMCT (D band) transitions. This excitation energy is also very close to the band gap. These different activation processes may have affected the trapping state densities, which resulted in slightly different forms of decay curves for the two excitation wavelengths shown in figure 6.10(a). The shorter time period (5000 ns) decay curves were obtained by exciting the samples with fixed wavelength light emitting diodes of bandwidths ~10 nm centred at 258 nm and 342 nm. These weak sources had pulse widths less than 1 ns and were flashed at 200 kHz while data was collected using time correlated single photon counting. Due to the long collection times,

the detector dark counts were estimated and subtracted, after which the data was normalized and is shown in figure 6.10(b). Following an initial fast decay for all the samples, those excited at higher energy (shorter wavelength) exhibited a long lifetime component indicating persistent luminescence, while the samples excited at the lower energy had a faster decay and negligible counts at the end of the 5 μs measurement window. This correlates with the low excitation peak measured at 344 nm compared to 255 nm in phosphorescence mode data (figure 6.9(a)) and shows that the traps responsible for the persistent luminescence were much more readily activated by short wavelength irradiation. In contrast, decay curves for La_2O_3:Bi [27] were close to straight lines for a logarithmic vertical scale and corresponded to lifetimes of ~250 ns. The emission related to traps in La_2O_2S:Bi has a complex time dependence down to the nanosecond scale and it is not easy to distinguish this from decay of the Bi^{3+} ions themselves. Further work will be required to understand the kinetics of the La_2O_2S:Bi luminescence better.

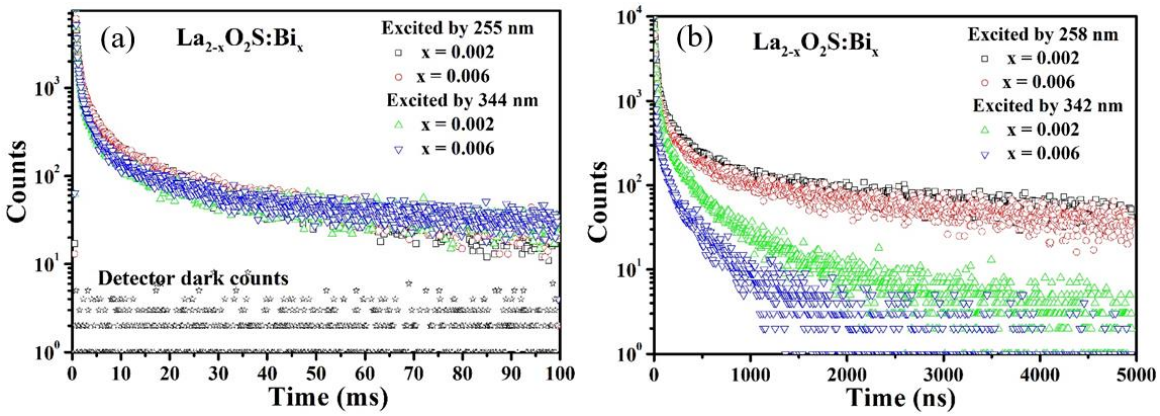

Figure 6.10: Decay curves of $La_{2-x}O_2S:Bi_x$ phosphor powders emitting at 456 nm for (a) 100 ms time window for excitation by a xenon flashlamp, and (b) 5 μs time window for excitation by pulsed light emitting diodes.

It is of interest that La_2O_2S was first synthesized in 1947 during experiments intended to produce La_2S_3 and to test it as a host for infrared-stimulated phosphors [33], i.e. a host having traps from which charge carriers would be released under infrared radiation to result in visible luminescence (not infrared-stimulated upconversion). Subsequently energy storage was studied in La_2O_2S:Eu [34, 35] and the mechanism was proposed to be excitation of Eu^{3+} to its charge transfer state and its disassociation into Eu^{2+} and a hole which was trapped in the host [36]. Persistent luminescence lasting a few minutes was also reported from La_2O_2S:Sm [37]. Recently, Luo *et al.* [38] considered charge trapping in rare-earth oxysulphides and

concluded that Ce^{3+}, Pr^{3+} and Tb^{3+} acted as hole traps at which recombination can occur when electrons trapped by host intrinsic defects are released, whereas Ti^{4+} and Eu^{3+} acted as electron traps at which recombination can occur when trapped holes are released. Therefore the host defects in such materials can trap both electrons and holes. Trivalent lanthanide ions having ground states levels close above the valance band may act as hole trapping centres [38] and, from figure 6, it has been established that the ground state of Bi^{3+} in La_2O_2S is very close to the valence band. For excitation corresponding to the MMCT process, the Bi^{3+} ion may dissociate into Bi^{4+} and an electron, which could be trapped by host intrinsic defects. Later detrapping of the electron would result in persistent luminescence. The low temperature thermoluminescence glow curves of Luo *et al.* [38] for Tb^{3+} and Pr^{3+} doped La_2O_2S indicated that electron de-trapping occurred below room temperature, which would explain why the room temperature persistent luminescence of La_2O2_S:Bi is relatively short. This suggests that introduction of a co-dopant which provides stronger electron trapping sites may improve the persistent luminescence of La_2O_2S:Bi. The assignment here of Bi^{3+} as a hole trap at which recombination may occur is in contrast to the suggestion that it functions as an electron trap in $MgGeO_3$ [39] and further research of persistent phosphors containing Bi is required.

6.4. Conclusion

Bi doped La_2O_2S was successfully synthesized by the ethanol-assisted solution combustion method. X-ray diffraction data confirmed that La_2O_2S crystallized in a hexagonal lattice. SEM images showed that the particles were aggregated and had irregular shapes. The reflectance spectra of the $La_{2-x}O_2S:Bi_x$ phosphor powder exhibited two absorption bands centred at 250 nm and 344 nm. The absorption band at 250 nm was observed for both undoped and Bi doped La_2O_2S and was attributed to absorption above the band gap. The weaker band at 344 nm was only present in the doped sample and was therefore attributed to absorption by Bi ions. From reflectance data of the pure host sample the band gap of La_2O_2S was found to be 4.90 eV. A broad band of blue emission at 456 nm, attributed to the $^3P_1 \rightarrow {}^1S_0$ transition of Bi^{3+} ions, was observed. The three excitation bands located at 260 nm, 298 nm and 344 nm were attributed to the $^1S_0 \rightarrow {}^1P_1$, $^1S_0 \rightarrow {}^3P_2$ and $^1S_0 \rightarrow {}^3P_1$ transitions of Bi^{3+} ions, respectively. Although the maximum luminescence intensity (for $La_{2-x}O_2S:Bi_{x=0.02}$) was only about a half of the maximum intensity that could be obtained for an optimized La_2O_3:Bi sample, the La_2O_2S:Bi phosphor was found to be stable when exposed to the atmosphere and

did not degrade like La_2O_3:Bi. The La_2O_2S:Bi samples showed long lifetime emission which did not occur for La_2O_3:Bi samples and this was attributed to Bi^{3+} acting as a hole trap.

6.5. References

1. Roy H.P. Awater, Pieter Dorenbos. The Bi^{3+} 6s and 6p Electron Binding Energies in Relation to the Chemical Environment of Inorganic Compounds. *Journal of Luminescence* 184 (2017) 221–231. https://doi.org/10.1016/j.jlumin.2016.12.021
2. Maria Méndez, Yolanda Cesteros, Lluís Francesc Marsal, Alexandre Giguère, Dominique Drouin, Pilar Salagre, Pilar Formentín, Josep Pallarès, Magdalena Aguiló, Francesc Dıaz, *et al.* Effect of Thermal Annealing on the Kinetics of Rehydroxylation of Eu^{3+}:La_2O_3 Nanocrystals. *Inorganic Chemistry* 51 (2012) 6139–6146. https://doi.org/10.1021/ic300108f
3. Noha Hakmeh, Christophe Chlique, Odile Merdrignac-Conanec, Bo Fan, François Cheviré, Xianghua Zhang, Xianping Fan, Xusheng Qiao. Combustion Synthesis and Up-Conversion Luminescence of La_2O_2S:Er^{3+},Yb^{3+} nanophosphors. *Journal of Solid State Chemistry* 226 (2015) 255–261. https://doi.org/10.1016/j.jssc.2015.02.015
4. Lili Wang, Qiang Sun, Qingzhi Liu, Jinsheng Shi. Investigation and Application of Quantitative Relationship between sp Energy Levels of Bi^{3+} ion and Host Lattice. *Journal of Solid State Chemistry* 191 (2012) 142–46. https://doi.org/10.1016/j.jssc.2012.03.015
5. Philippe Boutinaud. Revisiting the Spectroscopy of the Bi^{3+} Ion in Oxide Compounds. *Inorganic Chemistry* 52 (2013) 6028–6038. https://doi.org/10.1021/ic400382k
6. W.A.I. Tabaza, H.C. Swart, R.E. Kroon. Optical Properties of Bi and Energy Transfer from Bi to Tb in $MgAl_2O_4$ phosphor. *Journal of Luminescence* 148 (2014) 192–197. https://doi.org/10.1016/j.jlumin.2013.12.018
7. G. Blasse, W. Schipper, J.J. Hamelink. On the Quenching of the Luminescence of the Trivalent Cerium Ion. *Inorganica Chimica Acta* 189 (1991) 77–80. https://doi.org/10.1016/S0020-1693(00)80392-8
8. Koichi Momma, Fujio Izumi. VESTA 3 for Three-Dimensional Visualization of Crystal, Volumetric and Morphology Data. *Journal of Applied Crystallography* 44 (2011) 1272–1276. https://doi.org/10.1107/S0021889811038970
9. Douglas W. Ormond, Ephrain Banks. Synthesis of rare earth oxysulfide phosphors. *Journal of the Electrochemical Society* 122 (1975) 152–154. https://doi.org/10.1149/1.2134145

10. Markus Koskenlinna, M. Leskela, L. Niinisto. Synthesis and luminescence properties of europium-activated yttrium oxysulfide phosphors. *Journal of the Electrochemical Society* 123 (1976) 75–78. https://doi.org/10.1149/1.2132770

11. Lixi Wang, Xiaojuan Yang, Qitu Zhang, Bo Song, Chingping Wong. Luminescence Properties of $La_2O_2S:Tb^{3+}$ phosphors and Phosphor-Embedded Polymethylmethacrylate Films. *Materials and Design* 125 (2017) 100–108. https://doi.org/10.1016/j.matdes.2017.04.003

12. Xi-xian Luo, Wang-he Cao. Ethanol-Assistant Solution Combustion Method to Prepare La_2O_2S:Yb,Pr Nanometer Phosphor. *Journal of Alloys and Compounds* 460 (2008) 529–534. https://doi.org/10.1016/j.jallcom.2007.06.011

13. R.D. Shannon. Revised Effective Ionic Radii and Systematic Studies of Interatomie Distances in Halides and Chaleogenides. *Acta Crystallographica Section A* 32 (1976) 751–767. https://doi.org/10.1107/S0567739476001551

14. R.E. (Ted) Kroon. Nanoscience and the Scherrer equation versus the Scherrer–Gottingen equation. *South African Journal of Science* 109(5/6) (2013) Art. #a0019 (2 pages). http://dx.doi. org/10.1590/sajs.2013/a0019

15. Rosendo López, Ricardo Gómez. Band-Gap Energy Estimation from Diffuse Reflectance Measurements on Sol-Gel and Commercial TiO_2: A Comparative Study. *Journal of Sol-Gel Science and Technology* 61 (2012) 1–7. https://doi.org/10.1007/s10971-011-2582-9

16. Aman Pandey, Gunisha Jain, Divya Vyas, Silvia Irusta, Sudhanshu Sharma. Nonreducible, Basic La_2O_3 to Reducible, Acidic $La_{2-x}Sb_xO_3$ with Significant Oxygen Storage Capacity, Lower Band Gap, and Effect on the Catalytic Activity. *The Journal of Physical Chemistry C* 121 (2017) 481–489. https://doi.org/10.1021/acs.jpcc.6b10821

17. Jingbao Lian, Bingxin Wang, Ping Liang, Feng Liu, Xuejiao Wang. Fabrication and Luminescent Properties of $La_2O_2S:Eu^{3+}$ translucent Ceramic by Pressureless Reaction Sintering. *Optical Materials* 36 (2014) 1049–1053. https://doi.org/10.1016/j.optmat.2014.01.024

18. R. Vali. Electronic, Dynamical, and Dielectric Properties of Lanthanum Oxysulfide. *Computational Materials Science* 37 (2006) 300–305. https://doi.org/10.1016/j.commatsci.2005.08.007

19. D.L. Dexter, James H. Schulman. Theory of Concentration Quenching in Inorganic Phosphors. *The Journal of Chemical Physics* 22 (1954) 1063–1070. https://doi.org/10.1063/1.1740265.

20. A.M. Srivastava, S.J. Camardello. Concentration Dependence of the Bi^{3+} luminescence in $LnPO_4$ (Ln = Y^{3+}, Lu^{3+}). *Optical Materials* 39 (2015) 130–133. https://doi.org/10.1016/j.optmat.2014.11.011.

21. Lili Wang, Qiang Sun, Qingzhi Liu, Jinsheng Shi. Investigation and Application of Quantitative Relationship between sp Energy Levels of Bi^{3+} ion and Host Lattice. *Journal of Solid State Chemistry* 191 (2012) 142–146. https://doi.org/10.1016/j.jssc.2012.03.015

22. Keyan Li, Dongfeng Xue. Estimation of Electronegativity Values of Elements in Different Valence States. *Journal of Physical Chemistry A* 110 (2006) 11332–11337. https://doi.org/10.1021/jp062886k

23. B. Morosin. La_2O_2S structure refinement and crystal field. *Acta Crystallographica Section B* 29 (1973) 2647–2648. https://doi.org/10.1107/S0567740873007284

24. G. Blasse, A.C. van der Steen. Luminescence Characteristics of Bi^{3+}-Activated Oxides. *Solid State Communications* 31 (1979) 993–994. https://doi.org/10.1016/0038-1098(79)90016-4.

25. J. Zarembowitch, J. Gouteron, A.M. Lejus. Raman Spectra of Lanthanide Sesquioxide Single Crystals with A-type Structure. *physica status solidi (b)* 94 (1979) 249–256. https://doi.org/10.1002/pssb.2220940128

26. Joon Jae Oh, Byeong Kyou Jin, Woon Jin Chung, Dong Wook Shin, Yong Gyu Choi. Wavelength Conversion Characteristics of Eu^{3+}/Yb^{3+}-Activated La_2O_2S Luminophor. *Current Applied Physics* 11 (2011) S15–S18. https://doi.org/10.1016/j.cap.2011.01.047

27. See chapter 4.

28. Renping Cao, Fangteng Zhang, Chenxing Liao, Jianrong Qiu. Yellow-to-Orange Emission from Bi^{2+}-doped RF_2 (R = Ca and Sr) Phosphors. *Optics Express* 21 (2013) 15728–15733. https://doi.org/10.1364/OE.21.015728

29. Mingying Peng, Jincheng Lei, Liyi Li, Lothar Wondraczek, Qinyuan Zhang, Jianrong Qiu. Site-Specific Reduction of Bi^{3+} to Bi^{2+} in Bismuth-Doped over-Stoichiometric Barium Phosphates. *Journal of Materials Chemistry C* (2013) 5303–5308. https://doi.org/10.1039/c3tc31069h

30. See chapter 5.

31. Fengwen Kang, Xiaobao Yang, Mingying Peng, Lothar Wondraczek, Zhijun Ma, Qinyuan Zhang, Jianrong Qiu. Red Photoluminescence from Bi^{3+} and the Influence of the Oxygen-Vacancy Perturbation in $ScVO_4$: A Combined Experimental and Theoretical Study. *Journal of Physical Chemistry C* 118 (2014) 7515–7522. https://doi.org/10.1021/jp4081965

32. Chi-Yang Tsai, Jeng Wen Lin, Yih Ping Huang, Yung Chieh Huang. Modeling and

Assessment of Long Afterglow Decay Curves. *Scientific World Journal* 2014 (2014) 102524 (8 pages). https://doi.org/10.1155/2014/102524

33. John J. Pitha, Arthur L. Smith, Roland Ward. The Preparation of Lanthanum Oxysulfide and Its Properties as a Base Material for Phosphors Stimulated by Infrared. *Journal of the American Chemical Society* 69 (1947) 1870–1871. https://doi.org/10.1021/ja01200a009

34. H. Forest, A. Cocco, H. Hersh. Energy Storage in $La_2O_2S:Eu^{+3}$ with Direct $4f^6$ Eu^{+3} Excitation. *Journal of Luminescence* 3 (1970) 25–36. https://doi.org/10.1016/0022-2313(70)90005-0

35. G.A. Webster, H.G. Drickamer. High Pressure Study of Slow Phosphorescence in $La_2O_2S:Eu$. *The Journal of Chemical Physics* 72 (1980) 4661–4663. https://doi.org/10.1063/1.439799

36. C.W. Struck, W.H. Fonger. Dissociation of Eu^{+3} Charge-Transfer State in Y_2O_2S and La_2O_2S into Eu^{+2} and free hole. *Physical Review B* 4 (1971) 22–34. https://doi.org/10.1103/PhysRevB.4.22

37. Guodong Liu, Qinghong Zhang, Hongzhi Wang, Yaogang Li. A Reddish La_2O_2S-Based Long-Afterglow Phosphor with Effective Absorption in the Visible Light Region. *Materials Science and Engineering B* 177 (2012) 316–320. https://doi.org/10.1016/j.mseb.2011.12.045

38. Hongde Luo, Adrie J.J. Bos, Pieter Dorenbos. Charge Carrier Trapping Processes in RE_2O_2S (RE = La, Gd, Y, and Lu). *Journal of Physical Chemistry C* 121 (2017) 8760–8769. https://doi.org/10.1021/acs.jpcc.7b01577

39. Yumiko Katayama, Jumpei Ueda, Setsuhisa Tanabe. Effect of Bi_2O_3 Doping on Persistent Luminescence of $MgGeO_3:Mn^{2+}$ Phosphor. *Optical Materials Express* 4 (2014) 613–623. https://doi.org/10.1364/OME.4.000613

Chapter 7

Cathodoluminescence degradation of Bi doped La_2O_3 and La_2O_2S phosphor powders

7.1. Introduction

Lanthanum oxide (La_2O_3) and lanthanum oxysulphide (La_2O_2S) have attracted significant research interest due to their prospective use as catalytic materials and for their thermal, chemical, electrical, magnetic, ceramic and optical properties [1, 2]. Tb and Eu doped La_2O_2S powders are commercially available as X-ray phosphors, while La_2O_2S:Tb can also be used as a cathode ray tube (CRT) phosphor (P44-GX). La_2O_3:Tb has been investigated for photoluminescence (PL) and cathodoluminescence (CL) applications [3], while Sun Woog Kim *et al.* [4] recently reported an improvement in emission intensity of La_2O_2S:Tb synthesized by thermal decomposition in a molten eutectic Li_2SO_4–Na_2SO_4 flux mixture. La_2O_2S has the same hexagonal crystal structure as La_2O_3, but with S replacing the O at Wyckoff site 1*a* [5], so that the La is coordinated to three S atoms and four O atoms. Both of these hosts are wide band gap semiconductors with band gap energies of ~5 eV: the measured band gap of La_2O_2S (4.9 eV) is slightly less than for La_2O_2S (5.1 eV), which is consistent with the expectation from numerically modelling of these materials [6, 7]. Both have maximum phonon energies of ~400 cm^{-1} [8, 9], which is lower than most oxides and beneficial for phosphors to minimize nonradiative losses while maximizing the radiative emissions [10]. They also share the interesting property that Ce^{3+} emission is quenched in both of these hosts [11]. Although reports of various luminescent ions in each of these hosts occur in the literature, almost no studies have been reported which directly assess the same radiative centre in both of these hosts, making a comparison between them in terms of a phosphor host difficult. In the particular case of Eu^{3+} doping, where PL excitation is via the charge transfer band, the excitation range of La_2O_2S:Eu extends to longer wavelengths compared to La_2O_3:Eu [12]. This is due to the charge transfer from Eu^{3+} to S^{2-} in addition to charge transfer from Eu^{3+} to O^{2-} ions, the former taking place at lower energies. This gives an advantage of La_2O_2S:Eu over La_2O_3:Eu in the case where relatively long wavelength excitation is desired e.g. for white light emitting diode phosphors. However, this cannot be generalized to other ions (e.g. Tb^{3+}) when the excitation is not via the charge transfer mechanism. Joon Jae Oh *et al.* [13] reported that the spontaneous emission rate of Eu^{3+} in La_2O_2S was greater than in La_2O_3, resulting in stronger emission from the oxysulphide based

phosphor, which they attributed to greater perturbations being induced by the crystal field of La_2O_2S having mixed anions on the Eu^{3+} ions, thereby allowing the forbidden f-f transitions to become possible. However, they acknowledged that the La_2O_3 powders were difficult to prepare without $La(OH)_3$ contamination and this was likely to have reduced the emission intensity of the Eu^{3+} ions, since hydroxyl ions are known luminescence quenchers [14].

Luminescent materials activated by Bi^{3+} ions exhibit interesting optical properties due to a strong interaction with the surrounding host lattice [15]. La_2O_3:Bi was reported to have blue emission at 2.73 eV (454 nm) [16], but this host has been found to be hygroscopic and converted to a hydroxide within days after exposure to the atmosphere [17]. We have found that the luminescence intensity of freshly prepared La_2O_3:Bi exceeded that of La_2O_2S:Bi, although for La_2O_3:Bi exposed to the atmosphere hydroxylation occurs and the luminescence then degrades quickly to become less intense than that of La_2O_2S:Bi. This suggested that La_2O_3:Bi may be superior for PL in an inert or vacuum environment and motivated us to compare the CL emissions of Bi doped La_2O_3 and La_2O_2S in this study. Although we are unaware of any reports dealing with the CL of La_2O_2S:Bi, Miyata *et al.* [14, 18] investigated the PL and electroluminescence of La_2O_3:Bi thin films prepared by magnetron sputtering. At the turn of the century CRT phosphors all had sulphide (or oxysulphide) based host materials, namely ZnS:Ag,Cl (P22B) for blue, ZnS:Cu,Au,Al (P22G) for green and Y_2O_2S:Eu (P22R) for red [19]. However, sulphur-containing phosphors undergo changes in surface chemistry due to interaction of residual vacuum gases with the electron beam, which may lead to degraded CL brightness. More demanding applications, such as field emission displays (FEDs) which must operate at lower voltages and poorer vacuum, prompted investigations of oxide-based phosphors [19, 20] which may be considered more chemically and thermodynamically stable than sulphide-based phosphors, as well as more environmentally friendly. Following earlier studies on the CL degradation of ZnS based phosphors [21, 22], there was evidence that a layer of ZnO was formed on top of ZnS due to an electron-stimulated surface chemical reaction [23, 24] and more recent studies have been made of the degradation of ZnO [25, 26] and CaO:Bi [27]. In this work we present CL emission spectra of La_2O_3:Bi and La_2O_2S:Bi phosphor powders prepared by the sol-gel combustion synthesis and the ethanol-assisted solution combustion method, respectively. These are compared to PL emission from these samples, followed by CL degradation studies during which the elemental surface composition and_chemistry changes resulting from the electron bombardment were monitored using Auger electron spectroscopy (AES) and X-ray photoelectron spectroscopy

(XPS). These phosphors were evaluated and compared for possible application in flat panel information displays such as FEDs.

7.2. Experimental

The $La_{2-x}O_3:Bi_{x=0.002}$ phosphor powder was synthesized by the sol-gel combustion method at 250 °C using citric acid as the fuel. The product power was annealed at 1200 °C in air for 2 h and then stored in a vacuum desiccator to protect it from hydroxylation due to the moisture in the atmosphere [28]. The $La_{2-x}O_2S:Bi_{x=0.002}$ phosphor powder was prepared via the ethanol-assisted solution combustion method, followed by annealing for 2 h at 900 °C in a reducing atmosphere (5% H_2 in Ar gas). The Bi doping concentration for both samples was the same and the optimal value for maximum PL emission was used. The PL properties of the powders were measured using an FLS980 spectrometer from Edinburgh Instruments, having a continuous 450 W xenon lamp and double monochromator as excitation source. The CL and Auger measurements were carried out in an ultra-high vacuum chamber at the base pressure of $1.3x10^{-8}$ Torr with a PHI model 549 system. The CL data were collected with a PC2000-UV Spectrometer type using OOI Base32 software. The phosphor powder was irradiated with a beam of electrons with an energy of 2.5 keV and a beam current of 4 μA. AES and CL spectra were collected simultaneously and used to monitor the change of the CL intensity and the elemental changes on the surface of the sample. The chemical compositions and electronic states were analysed using XPS before and after degradation using a PHI 5000 Versaprobe system. The spectra were obtained by using a monochromatic Al Kα X-ray beam (1486.6 eV) generated by a 25 W, 15 kV electron beam. The binding energy scale was shifted so that the C 1s peak of adventitious C occurred at 284.5 eV to compensate for possible charging.

7.3. Results and discussion

7.3.1. CL emission of La_2O_3:Bi and La_2O_2S:Bi phosphor powders

Figure 7.1 compares the PL and CL emission spectra of the (a) La_2O_3:Bi and (b) LaO_2S:Bi powder phosphors. The PL was excited at different wavelengths corresponding to the maximum emission intensity determined from our previous work, namely 308 nm for La_2O_3:Bi and 260 nm for LaO_2S:Bi, while CL was measured under identical conditions as given in section 7.2. The data has been normalized since the intensities measured from the PL and CL systems cannot be directly compared. For both PL and CL the maximum emission

intensity of the La_2O_3:Bi was approximately double that of the LaO_2S:Bi. Figure 7.1(a) shows that for La_2O_3:Bi there was a shift in the peak position between the PL and CL maximum intensity positions from 462 nm to 485 nm. The full width at half-maximum (FWHM) of the PL emission band was 76 nm, but using an electron beam as excitation source resulted in a broader emission band with a FWHM of 91 nm. A similar red-shift and broadening was reported, for electroluminescence emission compared to PL, for La_2O_3:Bi thin films prepared by magnetron sputtering as reported by Miyata *et al.* [14, 18]. Figure 7.1(b) shows the CL emission spectrum of La_2O_2S:Bi centred at 500 nm, significantly red-shifted in comparison to the PL emission which had a maximum at 456 nm. The PL and CL emission spectra of La_2O_2S:Bi were significantly broader than the corresponding emission spectra of La_2O_3:Bi, having FWHM values of 139 nm and 134 nm, respectively. Therefore the CL spectrum of La_2O_2S:Bi was red-shifted but approximately the same broadness as the PL spectrum.

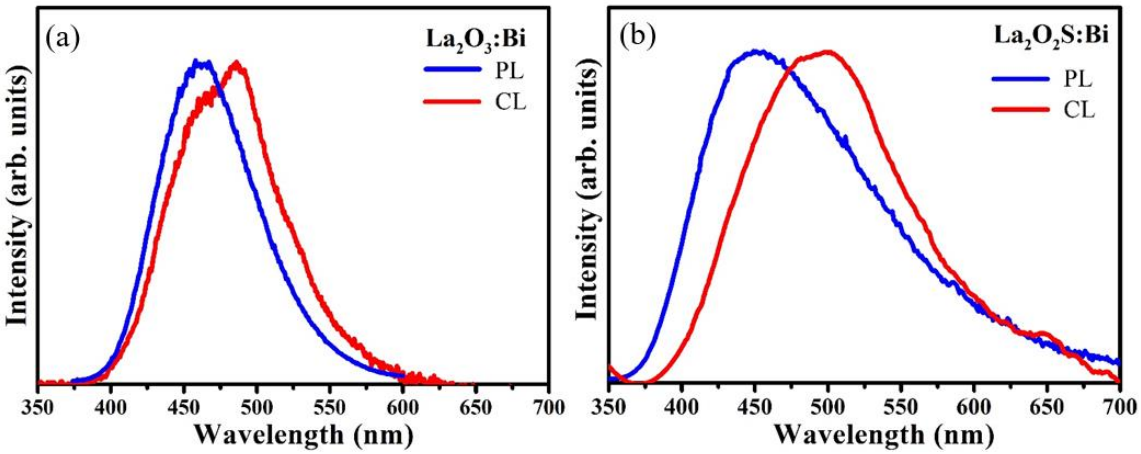

Figure 7.1: PL and CL emission spectra of (a) La_2O_3:Bi (b) La_2O_2S:Bi.

The ground state of the Bi^{3+} ion $6s^2$ configuration is $^1S_0$, while the excited $6s^16p^1$ configuration has four energy levels, namely $^3P_0$, $^3P_1$, $^3P_2$ and $^1P_1$ in order of increasing energy [29]. Although transitions from the $^1S_0$ ground state to the ^3P_J excited states are spin-forbidden, spin-orbit coupling of the $^1P_1$ and $^3P_1$ levels means that transitions to the $^3P_1$ become possible and absorption from $^1S_0$ to $^3P_1$ and $^1P_1$ levels are generally observed for Bi^{3+} ions. An intermediate absorption band corresponding to transitions from $^1S_0$ to $^3P_2$ is made possible by coupling with unsymmetrical lattice vibrational modes, although the $^1S_0$ to $^3P_0$ transition is normally considered as strongly forbidden [29]. The PL emissions can be attributed to the $^3P_1 \rightarrow {}^1S_0$ transitions in Bi^{3+} ions. Despite the different environments of the

Bi^{3+} ions, which substitute for La^{3+} ions in the hosts, the PL peak emission wavelengths are less than 10 nm different. The difference between PL and CL may be attributed to the large energy difference of the incident photons (4.03 eV for La_2O_3:Bi and 4.77 eV for La_2O_2S:Bi) compared to the electrons (2.5 keV) and hence the different mechanisms for the excitation. The luminescent Bi^{3+} centres were directly excited by the photons, exciting electrons from the ground state to the excited state. However, under the much higher energy electron beam irradiation during CL, luminescent centres in the phosphors may be excited by either direct or indirect excitation. When an electron penetrates the surface of a phosphor, it causes ionization of the host lattice atoms, freeing many secondary electrons which can also cause ionization and create further secondary electrons [30]. When lower energy secondary electrons reach the luminescent centres, they may directly excite the luminescent centres. Also, these secondary electrons generate many electron-hole pairs (EHs) by collision with lattice ions. Generated EHs may act as mobile carriers in the material and recombine at luminescent centres or may decay non-radiatively [31]. The energetic excitation caused by the electron beam may therefore lead to an increase in the FWHM and other changes to the emission spectra, although in the present case emission from higher excited states of the Bi^{3+} ion were not observed. The similar red shift in the emission reported by Miyata *et al.* for La_2O_3:Bi thin films, when observing electroluminescence compared to PL, was attributed to relaxation of the selection rule forbidding the lowest energy $^3P_0 \rightarrow {}^1S_0$ transition of Bi^{3+} ions as a result of the high electric field [32]. This transition, which may dominate at low temperature [33], has been reported in Bi doped SrO, CaS and CaO [34].

7.3.2. CL degradation of La_2O_3:Bi phosphor powder

Figure 7.2 shows the CL intensity maximum at 485 nm for La_2O_3:Bi as a function of electron dose exposure in vacuum at the base pressure of 1.3×10^{-8} Torr for 18 h. The CL intensity initially decreased but remained steady after 60 C/cm^2, so that at the end of the measurement the CL intensity was about 70% of the initial value. The CL emission spectra before and after the degradation process are shown in the inset. The peak position and shape of the CL spectrum remained the same before and after degradation, with only a small decrease in the intensity.

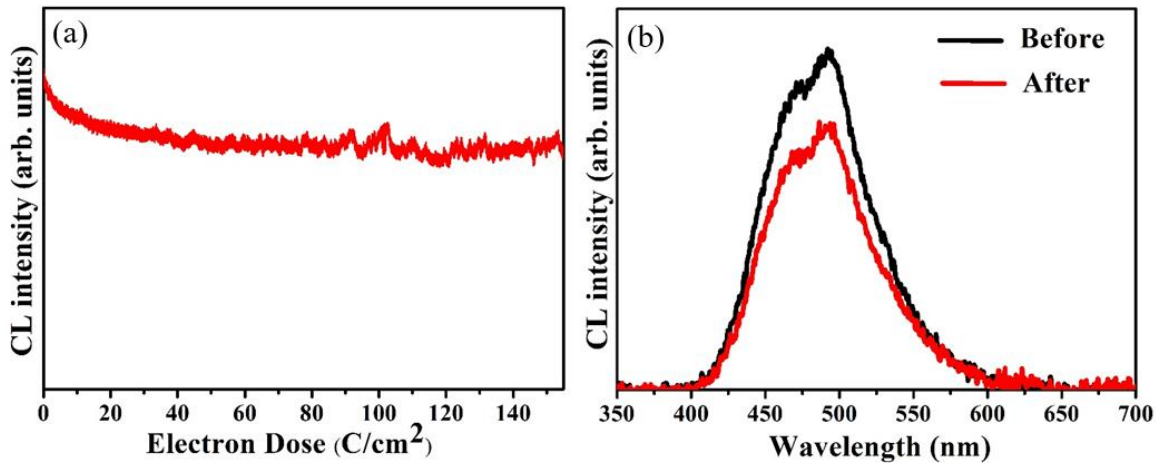

Figure 7.2: (a) CL Intensity of La_2O_3:Bi as a function of electron dose in vacuum at a base pressure of $1.3x10^{-8}$ Torr for 18 h. and (b) represents the CL spectra before and after degradation.

Figure 7.3(a) shows the AES spectra of the La_2O_3:Bi phosphor powder before and after degradation. The Auger peaks of the principle elements were observed at 82 eV and 629 eV for La and at 515 eV for O. Bi was not detected due to its low concentration, but the main peak will be expected at 101 eV [35], overlapping the strong low energy La1 peak. In addition, the impurity elements C and Cl were also detected in the Auger spectrum before degradation. These were attributed to adventitious impurity species on the surface due to handling and exposure to the atmosphere [36]. The small Cu peak was present due to the use of a Cu sample holder. Figure 7.3(b) shows the Auger peak-to-peak heights (APPH) of various signals (La2 at 629 eV, O at 515 eV and C at 272 eV) as a function of electron dose. The surface impurity (C) was removed during electron beam exposure and the C APPH had decreased to almost zero when the electron dose reached ~45 C/cm^2. Generally the other Auger signals associated with the host elements (i.e. La and O) are expected to increase as the C is removed from the surface, as reported for the degradation of ZnO [25, 26] and SrO:Bi [34]. Therefore it is unusual for the O APPH signal to decrease during this initial phase, especially between the electron dose of ~20 to 45 C/cm^2 as observed in this study. The C signal is generally associated with hydrocarbon contamination, but the correlation of C and O APPH signals in figure 7.3(b) suggests that carbonates may be present on the surface and are removed during electron beam exposure. This is consistent with the fact that La_2O_3 is known to react with CO_2 in the atmosphere to form carbonates [28]. Additionally, citric acid was used during the combustion synthesis and may result in contamination by carbonates, since infrared absorption measurements of both freshly prepared samples and those exposed to the

atmosphere contained peaks at 1391 and 1485 cm^{-1} associated with carbonates. Therefore the decrease in the C APPH signal is believed to be due to removal of predominantly adventitious C contamination up to a dose of ~20 C/m^2 (where the O signal shows little change) and thereafter predominantly carbonate contamination existing in the sample for the dose range of ~20 - 45 C/m^2 (where the O signal decreases). The removal of carbonates from the surface of phosphors during degradation may occur due to electron-stimulated surface chemical reactions (ESSCR) as reported by Swart *et al*. [37] and result in CO_2 release into the vacuum chamber. After the electron dose exceeds ~45 C/cm^2 the CL intensity and APPH signals remain fairly constant, indicating that no further degradation occurs. The La_2O_3:Bi is therefore becomes stable, after these initial effects, for long term electron bombardment, which makes it suitable as a blue emitting phosphor for use in FEDs.

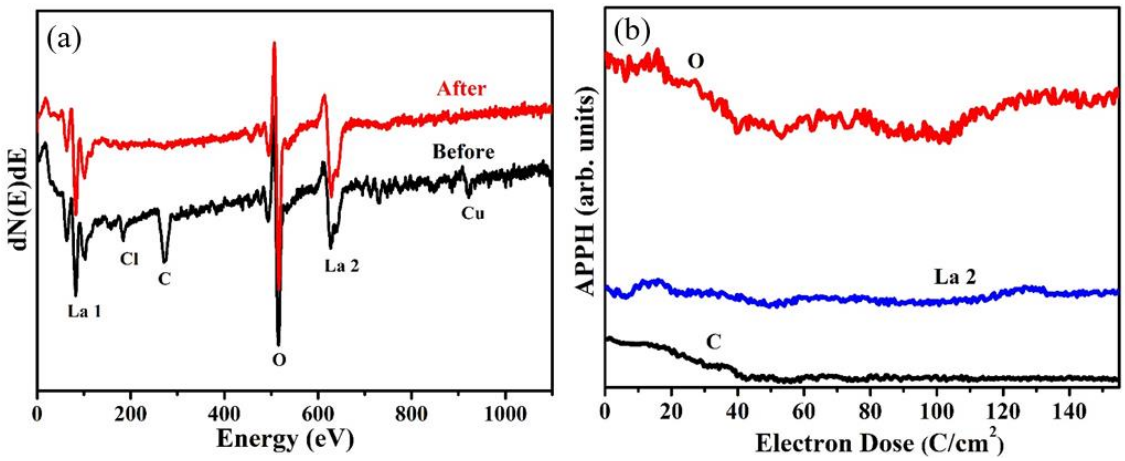

Figure 7.3: (a) AES spectra of La_2O_3:Bi phosphor powder before and after electron beam bombardment in a vacuum base pressure of $1.3x10^{-8}$ Torr, (b) Auger peak-to-peak heights of La, O and C as a function of electron dose.

Figure 7.4 shows high resolution XPS spectra of La_2O_3:Bi phosphor powders for various binding energy ranges associated with the C 1s, La 3d, O 1s, Bi 4d and Bi 4f electrons. The spectra are given before sputter cleaning (red) and after 2 min of sputter cleaning with a 2 kV Ar ion gun (blue). Although the AES data, previously discussed, showed clearly that C was removed from the surface during degradation, the degraded sample nevertheless displayed a strong C 1s XPS peak before sputter cleaning, which shows that adventitious C contamination occurred on the degraded sample surface between removal from the Auger system and loading in the XPS system. Although the main peak at 284.5 eV, attributed to hydrocarbons, decreased substantially after the sputter cleaning as expected, the small peak

with binding energy 289.5 eV was not reduced. This binding energy corresponds to C in carbonates [38, 39] and indicated that these are present inside the sample at low concentration. This peak also occurs for the degraded sample after sputter cleaning, suggesting that the removal of C observed during Auger measurements occurred only near the surface.

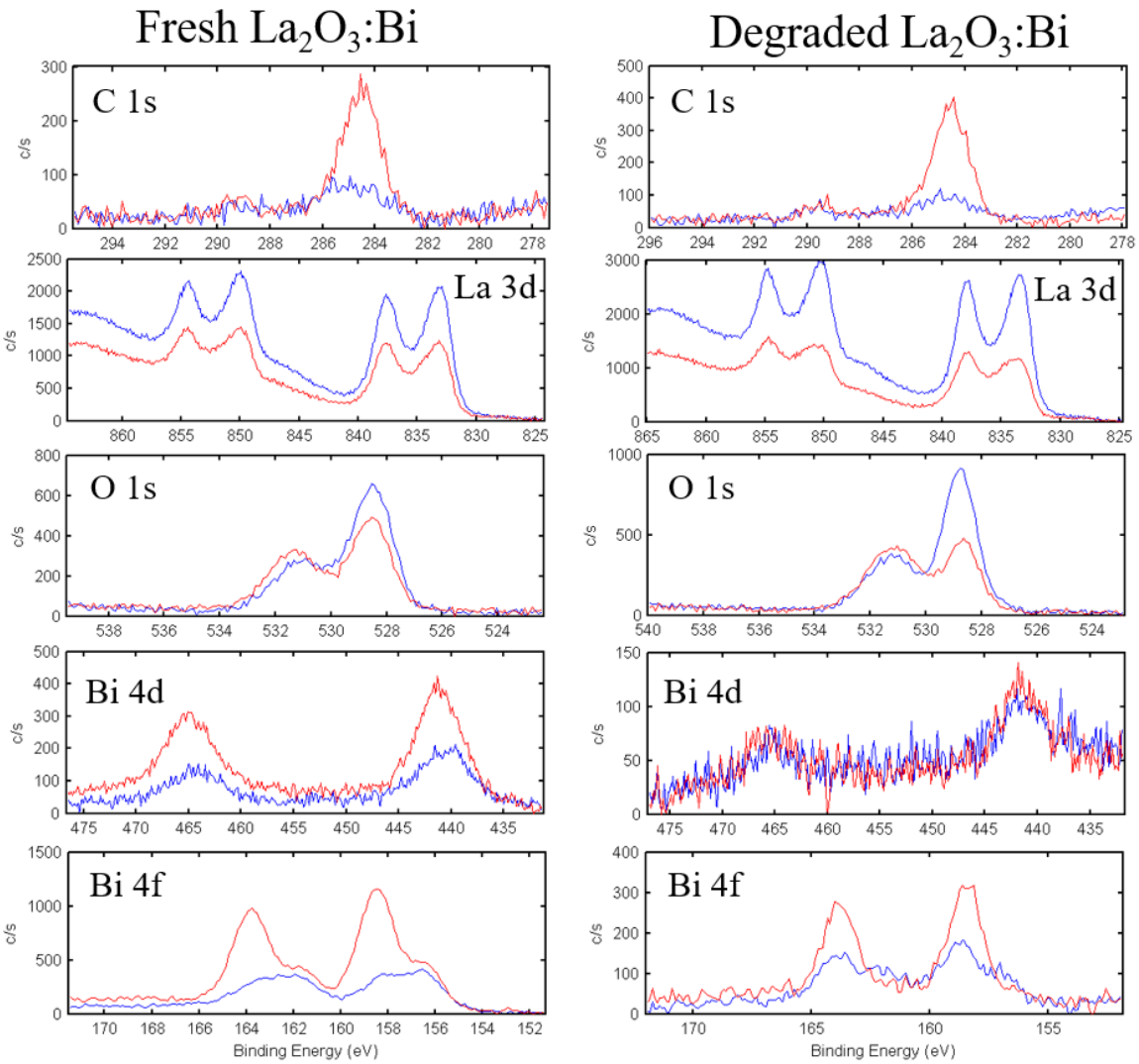

Figure 7.4: XPS spectra of La_2O_3:Bi phosphor powder for freshly prepared (left) and degraded (right) samples. The red curves are the measurements before sputter cleaning and the blue curves are the measurements after sputter cleaning.

La 3d photoelectron spectra are complicated [38, 40], generally consisting of four doublet peaks with 16.8 eV spin-orbit splitting for each bonding state of the La^{3+} ions. In addition, background fitting is made difficult by the fact that the broad La $M_{4,5}N_{4,5}N_{4,5}$ Auger peak

overlaps part of the binding energy range when using an Al Kα X-ray source [38]. Figure 7.4 shows that after sputtering the intensity of the La peaks increased, due to removal of the surface contamination. Qualitatively, the La 3d XPS spectra, after sputtering, for the freshly prepared and degraded samples are similar to one another and a quantitative fitting of the entire range was not performed. The lower binding energy region ~838 – 842 eV could be fit with three Gaussian peaks, as shown in figure 7.5(a) for the degraded sample after sputtering, which is expected in this limited range when all the La^{3+} ions have the same environment, as in the case of La_2O_3. However, the shift of La 3d peaks in different materials is small (e.g. the peak shifts between La in La_2O_3 and La in $La(OH)_3$ [38] are only a fraction of the peak's widths) and small quantities of La^{3+} ions in different environments would be challenging to detect using the La 3d XPS signal. Significant changes to the O 1s XPS spectra occurred before and after sputter cleaning. Considering spectra from the cleaned samples, they are similar in form, both consisting of two distinct peak separated by about 2 eV with the lower binding energy peak roughly twice as intense as the other. This is consistent with the O 1s spectra for La_2O_3 presented in Sunding *et al.* [38]. Considering the spectra before sputtering, they may be described by the same two peaks but with varying intensity ratio. This implies the presence of a third peak almost coinciding with one of the original peaks. Possibilities of O containing surface contamination include carbonates and hydroxides, which are known to form for La_2O_3 when exposed to the atmosphere and have similar O binding energies [39]. The C 1s spectra suggested that a low level of carbonates was present, but this was relatively unchanged by sputter cleaning and therefore these were suggested to be inside the bulk and result from the citric acid used during synthesis. This indicates that the most likely source of the O contamination is the formation of $La(OH)_3$ on the surface. Since XPS is a surface sensitive technique and hydroxylation of La_2O_3 occurs quickly, the formation of a surface layer of hydroxide may occur during the short times when samples are exposed to the atmosphere, which would be impossible to avoid without more elaborate sample handling facilities. The data presented by Sunding *et al.* [38] suggested that the binding energy for O in $La(OH)_3$ was between the two binding energies of O at its two sites in La_2O_3 and this was previously used to fit the O peak in La_2O_3/$La(OH)_3$ samples exposed to the atmosphere for extended times during which complete hydroxylation occurred. However, the present results suggest that the hydroxide-related peak has a binding energy which is very close to the higher binding energy peak of the oxide related pair. Hence only two peaks are observed, but the higher binding energy peak has contributions from the oxide and hydroxide and grows relative to the lower energy peak as more hydroxide is present. Fitting of the O 1s peak using

this alternative model, for the degraded sample before and after sputtering, is shown in figures 7.5(b) and (c) respectively. This model is similar to that of Fleming *et al.* [41] and Baškys *et al.* [42] who used two peaks separated by 2.0 eV, with the lower binding energy peak attributed to O in La_2O_3 and the higher binding energy peak for O in $La(OH)_3$. The difference is that we consider the higher binding energy peak to be a degenerate peak made up of signals from O in $La(OH)_3$ as well as O in La_2O_3. Physically, we expect O in La_2O_3 to produce two peaks because the O atoms are coordinated at two significantly different distances from the La. These two different coordination distances also resulted in an energy splitting and two peaks in the density of states for the valence band of La_2O_3 computed by Alemany *et al.* [43]. This model would additionally clarify why the higher energy peak of the pair was never eliminated despite attempts to produce pure oxide samples with no hydroxide [38, 41, 42].

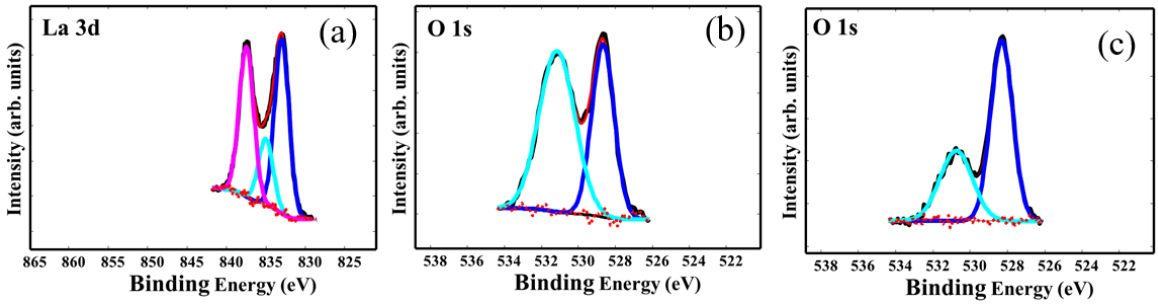

Figure 7.5: Fitting of selected XPS spectra of degraded samples given in figure 7.4. (a) La 3d, after sputtering. (b) O 1s, before sputtering. (c) O 1s, after sputtering.

Figure 7.4 also presents the XPS spectra for the Bi 4d and 4f binding energy regions. Considering particularly the Bi 4f spectra, which have a stronger signal, there is a marked decrease in the intensity of the Bi peaks after sputter cleaning. This shows that the surfaces of both the freshly prepared and degraded samples were enriched with Bi before sputter cleaning. External contamination from Bi is not considered possible. Surface enrichment of Bi for the freshly prepared sample has occurred due to segregation of Bi from the bulk during annealing. Although the signal from the degraded sample is weaker (with increased noise-to-signal ratio), its surface was also enriched with Bi, which was therefore not removed completely from the surface during CL degradation. Figure 7.6 presents fitting of the Bi 4f spectra for the sputter cleaned samples. These can be fitted by two pairs of doublets with spin-orbit separation of 5.3 eV as expected [39]. The large energy separation of the doublets (~2 eV), similar to that reported by Eom *et al.* [44] for pulsed laser deposited Bi_2O_3 thin

films, suggest that they originate from Bi^{3+} ions substituting La^{3+} ions in the host and from metallic Bi nanoparticles on the surface. The lower binding energy doublet corresponds to metallic Bi and is weaker for the degraded sample after sputtering, suggesting that the amount of Bi on the surface may be reduced during CL degradation. Elemental Bi is known to form a thick native oxide when exposed to air, giving rise to vivid colouration of such samples, therefore the existence of metallic Bi was unexpected and it may be that Bi nanoparticles are embedded near the surface in the host. Comparing figure 7.4 with figure 7.6, it can be seen that sputter cleaning more strongly reduced the peaks corresponding to the higher binding energy doublet, i.e. that corresponding to Bi^{3+} ions. Therefore this peak may have contributions from both Bi^{3+} ions substituting La^{3+} ions in the host as well as Bi in Bi_2O_3 formed by oxidation of segregated Bi on the surface. However, the Bi on the surface did not appear to play a critical role in the CL degradation of the La_2O_3:Bi phosphor powder.

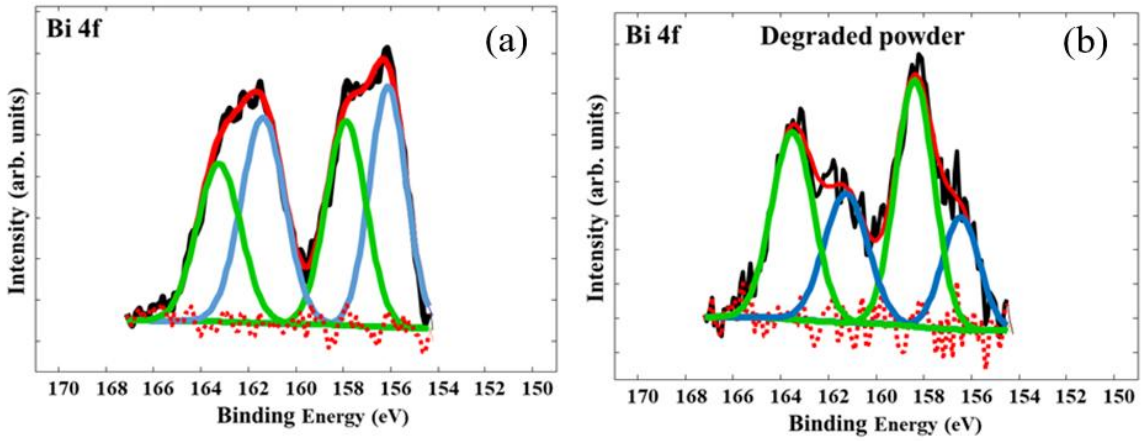

Figure 7.6: Fitting of the Bi 4f XPS spectra obtained after sputter cleaning of the (a) fresh sample. (b) Degraded sample.

7.3.3. CL degradation of La_2O_2S:Bi phosphor powder

Figure 7.7(a) shows the height of the CL intensity maximum at 500 nm for the La_2O_2S:Bi phosphor powder as a function of electron dose exposure in vacuum, at a base pressure of $1.3x10^{-8}$ Torr, for 22 h._The CL emission spectra before and after the degradation process shown in figure 7.7(b). The peak position and shape of the CL spectrum remained the same before and after degradation. The CL intensity decreased continuously (seemingly exponentially) so that at the end of the measurements it was only about 30% of the initial value. Hence a 22 h exposure to 2.5 keV electrons significantly reduced the CL intensity and

the sample was not resistant to degradation. It would therefore not be suitable for application as a CRT or FED phosphor.

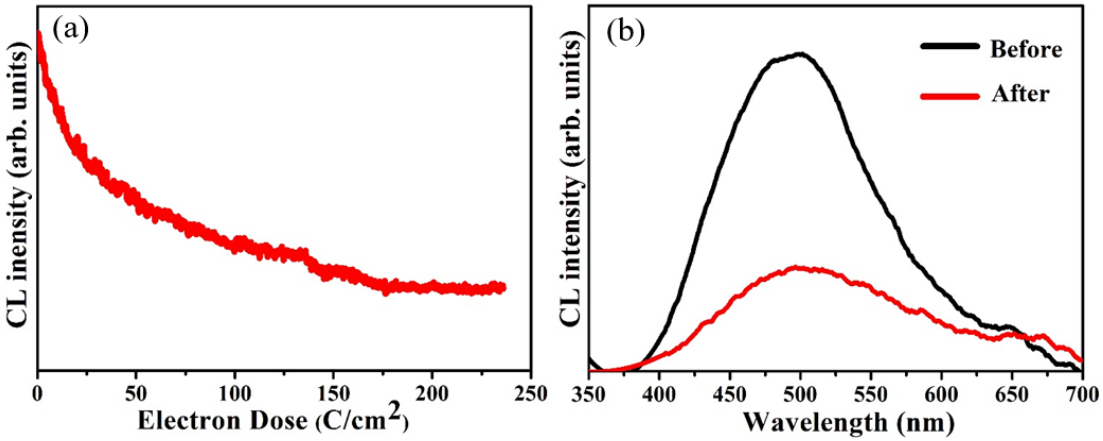

Figure 7.7: (a) CL intensity of La_2O_2S:Bi as a function of electron dose in vacuum, at base pressure of $1.3x10^{-8}$ Torr, for 22 h. (b) The CL spectrum before and after degradation.

Figure 7.8 shows the AES spectra of the La_2O_2S:Bi powder phosphor before and after CL degradation. The Auger spectrum before degradation showed peaks of all the host elements (La at 82 eV and 629 eV, O at 515 eV and S at 155 eV), as well as a small amount of surface contamination by carbon (C) and chlorine (Cl) which were attributed to adventitious impurity species due to handling and atmospheric exposure. As for the case of La_2O_3:Bi, the Bi dopant was not detected. After degradation the peak corresponding to S became much smaller, but was still present. This indicates that exposure to the electron beam had been accompanied by loss of S, which suggests the formation of a non-luminescent La_2O_3 layer on the surface causing degradation, rather than the formation of a S containing compound e.g. a sulphate layer. Dolo *et al.* [45] similarly found that CL degradation of Gd_2O_2S:Tb phosphor powder was accompanied by a loss of S from the surface and attributed the degradation to the formation of a non-luminescent (dead) layer of GdO_x on the surface. During degradation the Auger signals from the C and Cl contaminants were reduced to almost the noise level. Figure 7.8(b) shows the APPHs of La, O, S, and C as a function of electron dose. During the electron bombardment on the phosphor the S peak decreased, but stabilized at about 30 C/cm^2 and did not reduce to zero, while the APPH signals corresponding to the other elements remained constant. A few minutes elapsed between measurement of the Auger spectrum before degradation and the recording of the APPH signals, during which some degradation occurred. Therefore the decrease of the C peak was not captured and the initial

APPH signal for S is less than what would be expected from the Auger spectrum. The decrease of S on the surface was expected to be linked to the increase of some other Auger signal (e.g. O if La_2O_2S was converted to La_2O_3), but this was not observed.

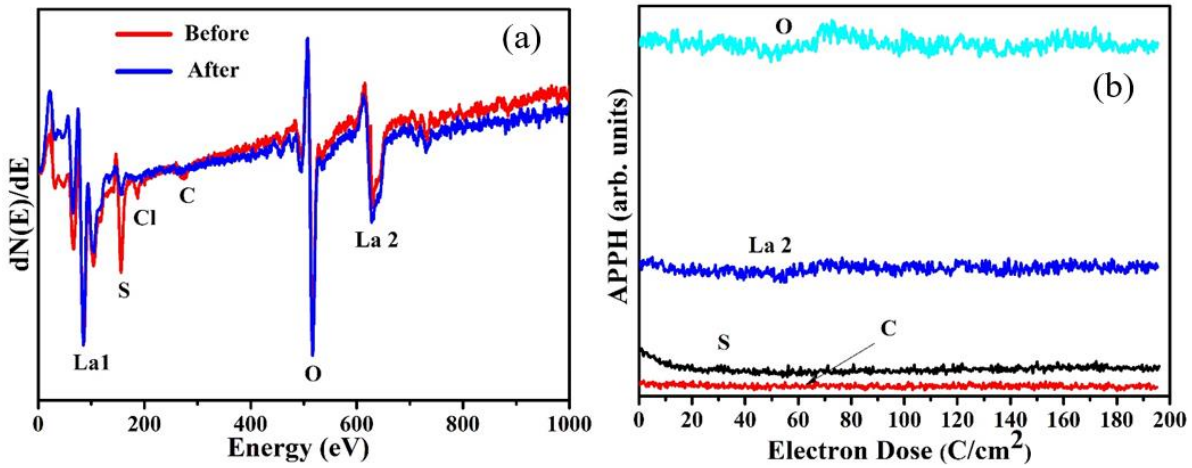

Figure 7.8: (a) AES spectra of La_2O_2S:Bi powder phosphor before and after electron beam bombardment in a vacuum base pressure of $1.3x10^{-8}$ Torr, (b) Auger peak-to-peak heights of La, O, S and C as a function of electron dose during degradation.

Figure 7.9 shows the high resolution XPS spectra of the fresh and degraded La_2O_2S:Bi phosphor powders for the binding energy ranges of C 1s, La 3d, O 1s, Bi 4d and S 2p. Spectra obtained before sputter cleaning are shown in red and those after sputter cleaning are shown in blue. There is no signal in the binding energy range for Bi 4d, indicating that the Bi on the surface was below the detection limit. This is fortuitous since the Bi 4f binding energy range overlaps the S 2p region shown in the bottom panels of figure 7.9 and would have complicated the S 2p spectrum if it had been present. It is a significant difference between La_2O_3:Bi and La_2O_2S:Bi that for the first there is Bi segregation to the surface, while for the second no Bi was detected on the surface. This suggests that the diffusion of Bi in the oxysulphide is inhibited.

For both the fresh and degraded samples adventitious C due to hydrocarbons was detected on the surface and reduced by sputter cleaning. However, the signal from C for the degraded sample was less than for the fresh sample. A small peak near 289.5 eV corresponding to carbonates was present (as also found for the La_2O_3:Bi) and is attributed to carbonates formed within the host during synthesis involving organic precursors.

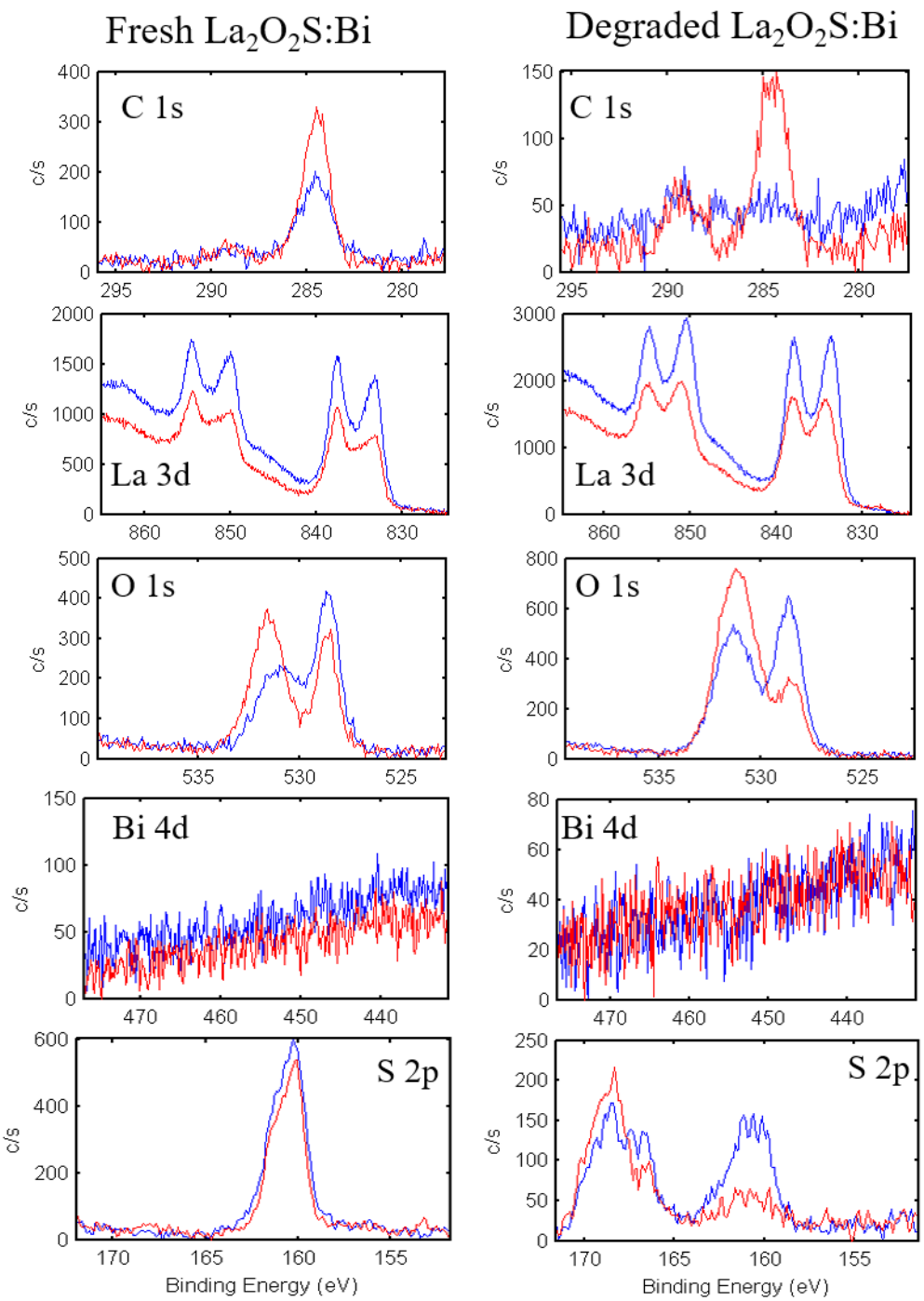

Figure 7.9: XPS spectra La_2O_2S:Bi phosphor powder for freshly prepared (left) and degraded (right) samples. The red curves are the measurements before sputter cleaning and the blue curves are the measurements after sputter cleaning.

The S 2p peak of the fresh La_2O_2S:Bi sample was unchanged after sputter cleaning. It has an asymmetrical shape because it is composed of an unresolved doublet ($2p_{1/2}$ and $2p_{3/2}$) with area ratio 1:2. The peak position near 160 eV is characteristic of S in sulphides [39]. Since

only one doublet is present, this indicates that all the S occupies sites with the same environment, which is expected from the crystal structure of La_2O_2S if it is similar to that of La_2O_3, but with S replacing O at the 1*a* Wyckoff site. Considering the S 2p peak of the degraded La_2O_2S:Bi sample, the counts are clearly less than for the fresh sample (with higher noise-to-signal ratio). This is consistent with less S on the surface as determined by AES, although the AES measurements suggested that very little S would remain on the surface while XPS indicated that a significant amount of S remains. This highlights the need to use complementary techniques for evaluating the degraded surface. For the unsputtered sample there is only a small peak near 160 eV and a larger peak near 169 eV, which is characteristic of S bonded in sulphates [39]. Therefore, in contradiction to the expectation from the AES data, the XPS results indicate that the degraded La_2O_2S:Bi contained sulphate on the surface. This was probably $La_2O_2SO_4$, which was observed as a contaminant in La_2O_2S samples prepared and annealed at temperatures below 900 °C. Sputter cleaning the sample reduced the peak near 169 eV and increased the peak near 160 eV, suggesting that a thin sulphate later was partially removed, exposing the (oxy)sulphide layer of the host beneath it. Swart *et al.* [46] reviewed reports of the CL degradation of ZnS and concluded that a $ZnSO_4$ layer was formed on the surface when it was exposed to dry oxygen in the vacuum chamber, while a ZnO layer was formed (with the emission of H_2S from the surface) when water was present. Therefore a combination of these mechanisms may have acted during the degradation of La_2O_2S:Bi during the present study.

Although there are definite changes in the La 3d XPS spectra of the fresh and degraded samples, before and after sputtering, the peaks occur generally in the same position with different intensities. Considering the spectra of the fresh sputter cleaned sample of La_2O_2S:Bi in the range 830 – 840 eV, without compensating for the background, the intensity of the lower binding energy peak is markedly less than the higher binding energy peak. The opposite trend occurred in figure 4 for La_2O_3:Bi. Without performing quantitative fits (like was done for La_2O_3:Bi in figure 7.5(a)), the relative heights of these peaks can be used to qualitatively distinguish between the oxide and oxysulphide. For the degraded sputter cleaned sample of La_2O_2S:Bi these two peaks are almost equal in height, suggesting a mixture of the two phases, consistent with the formation of La_2O_3 on the surface of the La_2O_2S:Bi sample during degradation.

The O 1s XPS spectrum for La_2O_3 in figure 7.5(b,c) was modelled in terms of two peaks, resulting from there being two separation distances for O and La. Since La_2O_2S has the same crystal structure as La_2O_3, but with S replacing O at the 1*a* Wyckoff site (which is the site of O atoms further from the La [43]), one may expect that the O 1s spectrum of for La_2O_2S would have a single peak, with binding energy near the higher value found for La_2O_3. However, the O 1s spectrum of the sputter clean fresh La_2O_2S:Bi sample showed two peaks and was similar to the spectra measured for the sputter cleaned La_2O_3:Bi samples. X-ray diffraction measurements of the La_2O_2S:Bi had shown it was not contaminated by other phases, but a possible reason that the second, lower binding energy, peak still occurs in La_2O_2S:Bi is that O and S are mixed on the two possible Wyckoff sites. It cannot be attributed to $La(OH)_3$ which is expected to give a peak close to the higher binding energy value of the oxide, or to $La_2O_2SO_4$ since the S 2p spectrum of the fresh sample shows only a doublet corresponding to the sulphide. However, a distribution of O and S over the two possible Wyckoff sites may have resulted in a second S 2p peak corresponding to two possible S-La distances, which was not observed. A further possibility is that some of the S in the La_2O_2S is actually replaced by O, giving $La_2O_{2+x}S_{1-x}$. For the sputter cleaned sample after degradation the relative height of the higher binding energy O 1s peak has increased compared to the fresh sample. Since sputter cleaned O 1s XPS spectra from La_2O_2S:Bi and La_2O_3:Bi samples were similar, no change would have been expected as a result of the formation of an oxide layer. However, if such an oxide layer underwent hydrolysis then the change could be explained by a hydroxide peak. A more direct possibility is that O in the sulphate layer which formed after degradation increases the O 1s signal at this binding energy, in the region expected for a signal from O in sulphates [39].

7.4. Conclusions

As in the case for PL, the initial CL emission intensity of La_2O_3:Bi was about double that of La_2O_2S:Bi powder phosphor. The CL emissions were shifted to longer wavelengths than the PL emission (from 462 nm to 485 nm in the case of La_2O_3:Bi and from 456 nm to 500 nm in the case of La_2O_2S:Bi), which has been attributed to a relaxation (as a result of the high electric field) of the selection rule forbidding the lowest energy $^3P_0 \rightarrow {}^1S_0$ transition of Bi^{3+} ions. The La_2O_3:Bi powder was found to be stable when exposed to the electron beam, following a small initial decrease in CL emission intensity corresponding to loss to C and other impurities from the surface. It may therefore be suitable for application as a blue phosphor in FEDs. However, the La_2O_2S:Bi CL emission decreased continuously under

electron beam irradiation and is unsuitable for CL applications. AES data showed that the S on the surface decreased, but was not eliminated, during exposure to the electron beam. CL degradation may be due to the formation of a non-luminescent layer of La_2O_3 on the surface, but XPS indicated that a sulphate (likely $La_2O_2SO_4$) was also present on the surface which may have contributed to the degradation.

7.5. References

1. Xing Wang, Hongxia Liu, Lu Zhao, Chenxi Fei, Xingyao Feng, Shupeng Chen, Yongte Wang. Structural Properties Characterized by the Film Thickness and Annealing Temperature for La_2O_3 Films Grown by Atomic Layer Deposition. *Nanoscale Research Letters* 12 (2017) 233 (7 pages). https://doi.org/10.1186/s11671-017-2018-8
2. Xi-xian Luo, Wang-he Cao. Ethanol-Assistant Solution Combustion Method to Prepare La_2O_2S:Yb,Pr Nanometer Phosphor. *Journal of Alloys and Compounds* 460 (2008) 529–534. https://doi.org/10.1016/j.jallcom.2007.06.011
3. Xiaoming Liu, Liushui Yan, Jianping Zou. Tunable Cathodoluminescence Properties of Tb^{3+}-Doped La_2O_3 Nanocrystalline Phosphors. *Journal of the Electrochemical Society* 157 (2010) 1-6. https://doi.org/10.1149/1.3262007
4. Sun Woog Kim, Takuya Hasegawa, Takeshi Abe, Hiroko Nakagawa, Shota Hasegawa, Kohei Seki, Kenji Toda, Kazuyoshi Uematsu, Tadashi Ishigaki, Mineo Sato. Abnormal Improvement in Emission of Lanthanum Oxysulfide Phosphor $La_2O_2S:Tb^{3+}$ Synthesized by a Novel Method, Thermal Decomposition in Eutectic Molten Salt. *Ceramics International* 42 (2016) 10389–10392. https://doi.org/10.1016/j.ceramint.2016.03.176
5. Noha Hakmeh, Christophe Chlique, Odile Merdrignac-Conanec, Bo Fan, François Cheviré, Xianghua Zhang, Xianping Fan, Xusheng Qiao. Combustion Synthesis and Up-Conversion Luminescence of $La_2O_2S:Er^{3+},Yb^{3+}$ nanophosphors. *Journal of Solid State Chemistry* 226 (2015) 255–261. https://doi.org/10.1016/j.jssc.2015.02.015
6. Ryo Yoshimatsu, Masahiro Okada, Tadashi Ishigaki, Shinta Watanabe, Tetsuo Honma, Koutoku Ohmi. Correlational analysis of Eu^{3+} charge transfer state using La effective charge in La-based mixed-anion host compounds. *Japanese Journal of Applied Physics* 56 (2017) 032601 (7 pages). https://doi.org/10.7567/JJAP.56.032601
7. Pere Alemany, Ibério De P. R. Moreira, Rodrigo Castillo, Jaime Llanos. Electronic, structural, and optical properties of host materials for inorganic phosphors. *Journal of Alloys and Compounds* 513 (2012) 630-640. doi:10.1016/j.jallcom.2011.11.036

8. J. Zarembowitch, J. Gouteron, A.M. Lejus. Raman Spectra of Lanthanide Sesquioxide Single Crystals with A-type Structure. *physica status solidi (b)* 94 (1979) 249–256. https://doi.org/10.1002/pssb.2220940128

9. C. R. Gopinatht, I. D. Brown. Normal Coordinate Analysis of the Raman and Infrared Vibrations of the Alpha Phases of RE_2O_3 (RE = La,Pr,Nd) and RE_2O_2S (RE = La and Yb). *Journal of Raman Spectroscopy* 12 (1982) 278–280. https://doi.org/10.1002/jrs.1250120315

10. Ge Yao. Mary, T. Berry, P. Stanley May, Dmitri S. Kilin. Optical Properties of Host Material for Phosphor Computational Modeling. *Journal of Quantum Chemistry* 112 (2012) 3889-3895. https://doi.org/10.1002/qua.24292

11. G. Blasse, W. Schipper, J.J. Hamelink. On the Quenching of the Luminescence of the Trivalent Cerium Ion. *Inorganica Chimica Acta* 189 (1991) 77–80. https://doi.org/10.1016/S0020-1693(00)80392-8

12. P. Dorenbos. The Eu^{3+} Charge Transfer Energy and the Relation with the Band Gap of Compounds. *Journal of Luminescence* 111 (2005) 89–104. https://doi.org/10.1016/j.jlumin.2004.07.003

13. Joon Jae Oh, Byeong Kyou Jin, Woon Jin Chung, Dong Wook Shin, Yong Gyu Choi. Wavelength Conversion Characteristics of Eu^{3+}/Yb^{3+}-Activated La_2O_2S Luminophor. *Current Applied Physics* 11 (2011) S15–S18. https://doi.org/10.1016/j.cap.2011.01.047

14. H.A.A. Seed Ahmed, O.M. Ntwaeaborwa, R.E. Kroon. High Efficiency Energy Transfer in Ce,Tb Co-Doped Silica Prepared by Sol-Gel Method. *Journal of Luminescence* 135 (2013) 15–19. https://doi.org/10.1016/j.jlumin.2012.10.037

15. A. Yousif, R.M. Jafer, S. Som, M.M. Duvenhage, E. Coetsee, H.C. Swart. Ultra-broadband luminescent from a Bi doped CaO matrix. *RSC Advances* 5 (2015) 54115–54122. https://doi.org/10.1039/C5RA09246A

16. Roy H.P. Awater, Pieter Dorenbos. The Bi^{3+} 6s and 6p Electron Binding Energies in Relation to the Chemical Environment of Inorganic Compounds. *Journal of Luminescence* 184 (2017) 221–231. https://doi.org/10.1016/j.jlumin.2016.12.021

17. Maria Méndez, Yolanda Cesteros, Lluís Francesc Marsal, Alexandre Giguère, Dominique Drouin, Pilar Salagre, Pilar Formentín, Josep Pallarès, Magdalena Aguiló, Francesc Dıaz, *et al.* Effect of Thermal Annealing on the Kinetics of Rehydroxylation of Eu^{3+}:La_2O_3 Nanocrystals. *Inorganic Chemistry* 51 (2012) 6139–6146. https://doi.org/10.1021/ic300108f

18. Toshihiro Miyata, Jun Ichi Ishino, Keiichi Sahara, Tadatsugu Minami. Color Control of Emissions from Rare Earth-Co-Doped La_2O_3:Bi Phosphor Thin Films Prepared by

Magnetron Sputtering. *Thin Solid Films* 519 (2011) 8095–8099. https://doi.org/10.1016/j.tsf.2011.04.236

19. P.H. Holloway, T.A. Trottier, B. Abrams, C. Kondoleon, S.L. Jones, J.S. Sebastian, W.J. Thomes, H.C. Swart. Advances in Field Emission Displays Phosphors *Journal of Vacuum Science and Technology B* 17 (1999) 758-764. https://doi.org/10.1116/1.590634

20. Shreyas S. Pitale, Vinay Kumar, I.M. Nagpure, O.M. Ntwaeaborwa, E. Coetsee, H.C. Swart. Cathodoluminescent Properties and Surface Characterization of Bluish-White $LiAl_5O_8$:Tb Phosphor. *Journal of Applied Physics* 109 (2011) 013105 (8 pages). https://doi.org/10.1063/1.3530607

21. J.S. Sebastian, H.C. Swart, T.A. Trottier, S.L. Jones, P.H. Holloway. Degradation of ZnS Field-Emission Display Phosphors during Electron-Beam Bombardment Degradation of ZnS Field-Emission Display Phosphors during Electron-Beam Bombardment. *Journal of Vacuum Science & Technology A* 15 (1997) 2349–2353. https://doi.org/10.1116/1.580746

22. H.C. Swart, K.T. Hillie. Degradation of ZnS FED Phosphors. *Surface and Interface Analysis* 30 (2000) 383–386. https://doi.org/10.1002/1096-9918(200008)30:1<383::AID-SIA779>3.0.CO;2-V

23. A.P. Greeff, H.C. Swart. A Monte Carlo Simulation of Cathodoluminescence Generated in ZnS Phosphor Powders. *Radiation Effects and Defects in Solids* 154 (2001) 367-372. https://doi.org/10.1080/10420150108214079

24. H.C. Swart, K.T. Hillie, A.P. Greeff. Effect of Temperature on the Degradation of ZnS FED Phosphors. *Surface and Interface Analysis* 32 (2001) 110-113. https://doi.org/10.1002/sia.1018

25. Emad Hasabeldaim, Odireleng M. Ntwaeaborwa, Robin E. Kroon and Hendrik C. Swart. Surface Analysis and Cathodoluminescence Degradation of Undoped ZnO and ZnO:Zn Phosphors. *Journal of Vacuum Science & Technology B* 34 (2016) 041221 (8 pages). https://doi.org/10.1116/1.4953561

26. E. Hasabeldaim, O.M. Ntwaeaborwa, R.E. Kroon, V. Craciun, E. Coetsee, H.C. Swart. Surface Characterization and Cathodoluminescence Degradation of ZnO Thin Films. *Applied Surface Science* 424 (2016) 412-420. https://doi.org/10.1016/j.apsusc.2016.11.178

27. A. Yousif, R.E. Kroon, E. Coetsee, O.M. Ntwaeaborwa, H.A.A. Seed Ahmed, H.C. Swart. Luminescence and Electron Degradation Properties of Bi Doped CaO Phosphor. *Applied Surface Science* 356 (2015) 1064–1069. https://doi.org/10.1016/j.apsusc.2015.08.210

28. Elena Haibel, Stefan Berendts, Dirk Walter. Thermogravimetric and X-Ray Diffraction Investigation on Carbonated Lanthanum Oxide and Lanthanum Hydroxide

Formed in Humid CO_2 atmosphere. *Journal of Thermal Analysis and Calorimetry* 134 (2018) 261–267. https://doi.org/10.1007/s10973-018-7256-1

29. A.M. Srivastava, S.J. Camardello. Concentration Dependence of the Bi^{3+} luminescence in $LnPO_4$ (Ln = Y^{3+},Lu^{3+}). *Optical Materials* 39 (2015) 130–133. https://doi.org/10.1016/j.optmat.2014.11.011

30. R.M. Jafer, H.C. Swart, A. Yousif, Vinod Kumar, E. Coetsee. The Effect of Annealing Temperature on the Luminescence Properties of Y_2O_3 phosphor Powders Doped with a High Concentration of Bi^{3+}. *Journal of Luminescence* 180 (2016) 198–203. https://doi.org/10.1016/j.jlumin.2016.08.042

31. A. Yousif, R.M. Jafer, S. Som, M.M. Duvenhage, E. Coetsee, H.C. Swart, Ultra-broadband luminescent from a Bi-doped CaO matrix. *RSC Advances* 5(67) (2015) 54115–54122. https://doi.org/10.1039/c5ra09246a

32. Tadatsugu Minami, Toshihiro Miyata, Kouhei Ueda, Shun Matsui, Haruki Fukada. PL and EL Characteristics in New Blue Emitting La_2O_3:Bi Phosphor Thin Films. *ECS Transactions* 16 (2009) 39-45. https://doi.org/10.1149/1.3106670

33. V. Babin, V. Gorbenko, A. Krasnikov, A. Makhov, M. Nikl, K. Polak, S. Zazubovich, Yu Zorenko. Peculiarities of Excited State Structure and Photoluminescence in Bi^{3+}-Doped Lu_3 Al_5O_{12} Single-Crystalline Films. *Journal of Physics: Condensed Matter* 21 (2009) 415502 (9 pages). https://doi.org/10.1088/0953-8984/21/41/415502

34. Mogahid H.M. Abdelrehman, Robin E. Kroon, Abdelrhman Yousif, Hassan A.A. Seed Ahmed, Hendrik C. Swart. Luminescence Properties and Cathodoluminescence Degradation of Bi Doped SrO Powder. *Journal of Vacuum Science & Technology B* 37 (2019) 011206 (10 pages). https://doi.org/10.1116/1.5075492

35. Lawrence E. Davis, Noel C. Mac Donald, Paul W. Palmberg, Gerald E. Riach, Roland E. Weber, Handbook of Auger Electron Spectroscopy: A Reference Book of Standard Data for Identification and Interpretation of Auger Electron Spectroscopy Data, 2nd ed. (Physical Electronics Division of Perkin-Elmer, Minnesota, 1978), p. 246. ISBN: 9788578110796.

36. L. Oosthuizen, H.C. Swart, P.E. Viljoen, P.H. Holloway, G.L.P. Berning. ZnS:Cu,Al,Au Phosphor Degradation under Electron Excitation. *Applied Surface Science* 120 (1997) 9–14. https://doi.org/10.1016/s0169-4332(97)00246-8

37. H.C. Swart, J.J. Terblans, O.M. Ntwaeaborwa, R.E. Kroon, B.M. Mothudi. PL and CL Degradation and Characteristics of $SrAl_2O_4$: Eu^{2+},Dy^{3+}phosphors. *Physica B: Condensed Matter* 407 (2012) 1664–67. https://doi.org/10.1016/j.physb.2011.09.112

38. M.F. Sunding, K. Hadidi, S. Diplas, O.M. Løvvik, T.E. Norby, A.E. Gunnæs. XPS

Characterisation of in Situ Treated Lanthanum Oxide and Hydroxide Using Tailored Charge Referencing and Peak Fitting Procedures. *Journal of Electron Spectroscopy and Related Phenomena* 184 (2011) 399–400. https://doi.org/10.1016/j.elspec.2011.04.002

39. John F. Moulder, William F. Stickle, Peter E. Sobol, Kenneth D. Bomben. Jill Chastain (Editor). Handbook of X-ray Photoelectron Spectroscopy. Revised Ed. Perkin Elmer Corporation, Eden Prairie, Minnetsoa, USA (1992). ISBN: 978-0-9627026-2-4

40. D.F. Mullica, C.K. Lok, H.O. Perkins, X-ray photoelectron final-state screening in $La(OH)_3$: a multiplet structural analysis, *Physical Review B* 31 (1985) 4039–4042. https://doi.org/10.1103/PhysRevB.31.4039

41. Peter Fleming, Richard A. Farrell, Justin D. Holmes, Michael A. Morris. The Rapid Formation of $La(OH)_3$ from La_2O_3 Powders on Exposure to Water Vapor. *Journal of the American Ceramic Society* 93 (2010) 1187–1194. https://doi.org/10.1111/j.1551-2916.2009.03564.x

42. E. Baškys, V. Bondarenka, S. Grebinskij, M. Senulis and R. Sereika. XPS study of sol–gel produced lanthanum oxide thin films. *Lithuanian Journal of Physics* 54 (2014) 120–24. https://doi.org/10.3952/physics.v54i2.2921

43. Pere Alemany, Ibério De P. R. Moreira, Rodrigo Castillo, Jaime Llanos. Electronic, Structural, and Optical Properties of Host Materials for Inorganic Phosphors. *Journal of Alloys and Compounds* 513 (2012) 630–640. https://doi.org/10.1016/j.jallcom.2011.11.036

44. Ji-ho Eom, Hyun-june Jung, Jun-hee Han, Jeong-yong Lee, Soon-gil Yoon. Formation of Bismuth Nanocrystals in Bi_2O_3 Thin Films Grown at 300 K by Pulsed Laser Deposition for Thermoelectric Applications. *ECS Journal of Solid State Science and Technology* 3 (2014) 315–319. https://doi.org/10.1149/2.0101410jss

45. J. J. Dolo, H. C. Swart, J. J. Terblans, E. Coetsee, M. S. Dhlamini, O. M. Ntwaeaborwa, B. F. Dejene.Degradation of commercial Gd2O2S:Tb phosphor. *Phys. State. Sol (c)* 5 (2008) 594-597.doi: 10.1002/pssc.200776817ds

46. H.C. Swart, J.J. Terblans, E. Coetsee, O.M. Ntwaeaborwa, M.S. Dhlamini, S. Nieuwoudt, P.H. Holloway. Review on electron stimulated surface chemical reaction mechanism for phosphor degradation. *Journal of Vacuum Science & Technology A* 25 (2007) 917–921. 10.1116/1.2539467

Chapter 8

Conclusions and future work

8.1 Summary of the results

$La_{2-x}O_3:Bi_x$ has been successfully synthesized via the sol-gel combustion method. The X-ray diffraction (XRD) patterns confirmed the formation of the pure La_2O_3 hexagonal phase. Scanning electron microscopy (SEM) images showed that the grain size increased with increasing annealing temperature. The diffuse reflectance spectra (DRS) for the doped sample showed two absorption bands, one located at 308 nm and another at shorter wavelengths (250 nm and less). The band located at 308 nm was only present in the doped samples and was therefore attributed to absorption by Bi^{3+} ions. The shorter wavelength absorption was due to the metal-to-metal charge transfer (MMCT) absorption of the Bi^{3+} ions and the indirect band gap absorption. From reflectance data of the pure host sample the band gap of La_2O_3 was found to be 5.1 eV. A broad band of blue fluorescence emission centered at 462 nm was observed when excited at 308 nm, which was attributed to the $^3P_1 \rightarrow {}^1S_0$ transition of Bi^{3+} ions. The emission intensity was measured as a function of Bi doping concentration, with the maximum occurring for x = 0.002. The concentration quenching at this relatively low doping concentration was attributed to strong interaction of the Bi^{3+} ions allowing energy migration between them, which also was responsible for the decrease in the average lifetime observed with increasing doping concentration. The reported properties show that $La_{2-x}O_3:Bi_x$ can be used as a blue emitting phosphor and clarify the energy level diagram for this material.

The La_2O_3 host was found to be unstable under ambient conditions and converted to more stable $La(OH)_3$ due to its hygroscopic nature when exposed to the atmosphere. The change in crystal phase was confirmed by XRD and Fourier transform infrared spectroscopy (FTIR) and was accompanied by a loss of luminescence. The O 1 s X-ray photoelectron spectroscopy (XPS) binding energy spectra could be qualitatively explained by the formation of a new peak corresponding to $La(OH)_3$ in the degraded sample occurring at a binding energy between those of the double peak associated with La_2O_3. The degraded samples were re-annealed and it was found that the structure could be reverted completely to La_2O_3, while the blue photoluminescence (PL) emission was once again observed at about one third of the intensity as for the freshly prepared sample. For samples stored in a vacuum desiccator for

one week, no change for XRD and PL were observed. Initial trials showed that the degradation was reduced significantly by encapsulation of the phosphor in a poly(methyl methacrylate (PMMA) polymer. Although $La_{2-x}O_3:Bi_x$ can be used as a blue emitting phosphor, it is only suitable for applications where it will not be exposed to moisture in the atmosphere. Therefore, it may have an application as a moisture sensor, because while the luminescence remains high it is evidence that it has not been exposed to the atmosphere.

Bi doped La_2O_2S was successfully synthesized by the ethanol-assisted solution combustion method. X-ray diffraction data confirmed that La_2O_2S crystallized in a hexagonal lattice. SEM images showed that the particles were aggregated and had irregular shapes. The reflectance spectra of the $La_{2-x}O_2S:Bi_x$ phosphor powder exhibited two absorption bands centred at 250 nm and 344 nm. The absorption band at 250 nm was observed for both undoped and Bi doped La_2O_2S and was attributed to absorption above the band gap. The weaker band at 344 nm was only present in the doped sample and was therefore attributed to absorption by Bi ions. From reflectance data of the pure host sample the band gap of La_2O_2S was found to be 4.90 eV. A broad band of blue emission at 456 nm, attributed to the $^3P_1 \rightarrow {}^1S_0$ transition of Bi^{3+} ions, was observed. The three excitation bands located at 260 nm, 298 nm and 344 nm were attributed to the $^1S_0 \rightarrow {}^1P_1$, $^1S_0 \rightarrow {}^3P_2$ and $^1S_0 \rightarrow {}^3P_1$ transitions of Bi^{3+} ions, respectively. Although the maximum luminescence intensity (for $La_{2-x}O_2S:Bi_{x=0.02}$) was only about a half of the maximum intensity that could be obtained for an optimized La_2O_3:Bi sample, the La_2O_2S:Bi phosphor was found to be stable when exposed to the atmosphere and did not degrade like La_2O_3:Bi. The La_2O_2S:Bi samples showed long lifetime emission which did not occur for La_2O_3:Bi samples and this was attributed to Bi^{3+} acting as a hole trap.

As in the case for PL, the initial cathodoluminescence (CL) emission intensity of La_2O_3:Bi was about double that of La_2O_2S:Bi powder phosphor. The CL emissions were shifted to longer wavelengths than the PL emission (from 462 nm to 485 nm in the case of La_2O_3:Bi and from 456 nm to 500 nm in the case of La_2O_2S:Bi), which has been attributed to a relaxation (as a result of the high electric field) of the selection rule forbidding the lowest energy $^3P_0 \rightarrow {}^1S_0$ transition of Bi^{3+} ions. The La_2O_3:Bi powder was found to be stable when exposed to the electron beam, following a small initial decrease in CL emission intensity corresponding to loss to C and other impurities from the surface. It may therefore be suitable for application as a blue phosphor in field emission displays (FEDs). However, the La_2O_2S:Bi CL emission decreased continuously under electron beam irradiation and is unsuitable for CL

applications. Auger electron spectroscopy (AES) data showed that the S on the surface decreased, but was not eliminated, during exposure to the electron beam. CL degradation may be due to the formation of a non-luminescent layer of La_2O_3 on the surface, but XPS indicated that a sulphate (likely $La_2O_2SO_4$) was also present on the surface which may have contributed to the degradation.

8.2. Suggestions for future work

For future work the following is suggested:

1. Studying the energy transfer between the Bi and other lanthanides e.g. Eu in the La_2O_3 and La_2O_2S hosts.
2. Preparing La_2O_3:Bi and La_2O_2S:Bi thin films by using sol-gel spin-coated and PLD and comparing the results with the powders results.
3. Preparing La_2O_3:Bi composited with PMMA polymer by using sol-gel spin-coated thin films and comparing the luminescence stability to that from the PMMA mixed La_2O_3:Bi characterized in this work.
4. Trying to solve the problem of the hygroscopic nature of the La_2O_3 alternatively, one can add some materials (e.g. Ga and Y) to the La_2O_3 material to attempt to make it more stable.
5. Preparing other rare earth oxysulphide hosts doped with the Bi (e.g. Y_2O_2S) and comparing the results with La_2O_2S host.
6. To characterize the phosphors produced during this study using thermoluminescence.

8.3. Presentations at conferences/workshops:

1. B.M. Jaffar, H.C. Swart, H.A.A. Seed Ahmed and R.E. Kroon. 2017. Synthesis and characterisation of La_2O_3:Bi phosphor. Oral delivered at the 10th African Laser Centre Student Workshop, Stellenbosch, South Africa. 30 Nov – 2 Dec 2017.
2. B.M. Jaffar, H.C. Swart, H.A.A. Seed Ahmed, A. Yousif and R.E. Kroon. 2018. Sol-gel combustion synthesis and stability of La_2O_3:Bi^{3+} powder phosphor. Oral delivered at the 63rd Annual Conference of the South African Institute of Physics, Bloemfontein, South Africa. 25 – 29 June 2018.
3. B.M. Jaffar, H.C. Swart, H.A.A. Seed Ahmed, A. Yousif, R.E. Kroon. 2019. Cathodoluminescence degradation of bismuth doped La_2O_3 and La_2O_2S phosphor powders. *Abstract submitted to the* 8th South African Conference on Photonic Materials (SACPM2019), Kariega Game Reserve, South Africa. 6 – 10 May 2019.

8.4. Papers published/submitted:

1. B.M. Jaffar, HC. Swart, H.A.A. Seed Ahmed, A. Yousif, R.E. Kroon. Luminescence properties of Bi doped La_2O_3 powder phosphor. Journal of Luminescence 209 (2019) 217–224. https://doi.org/10.1016/j.jlumin.2019.01.044
2. B.M. Jaffar, HC. Swart, H.A.A. Seed Ahmed, A. Yousif, R.E. Kroon. Stability of La_2O_3:Bi^{3+} powder phosphor and PMMA composites. Journal of Physics and Chemistry of Solids 131 (2019) 156-163. https://doi.org/10.1016/j.jpcs.2019.04.004
3. B.M. Jaffar, HC. Swart, H.A.A. Seed Ahmed, A. Yousif, R.E. Kroon. Optical properties and stability of Bi doped La_2O_2S. Submitted to Optical Materials.